Target Definition in Biologically-Conformal Radiation Therapy

By

Tyler J. Bradshaw

A dissertation submitted in partial fulfillment of

the requirements for the degree of

Doctor of Philosophy

(Medical Physics)

at the

UNIVERSITY OF WISCONSIN-MADISON

2015

Date of final oral examination: 01/21/2015

Members of the Final Oral Committee:
Robert Jeraj, Associate Professor, Medical Physics
Bryan Bednarz, Assistant Professor, Medical Physics
Michael W. Kissick, Assistant Professor, Medical Physics
Mark A. Ritter, Professor, Human Oncology
Jun Zhu, Professor, Statistics

Table of contents

List of abbreviations

BED	Biologically effective dose
BCRT	Biologically-conformal radiation therapy
CIRT	Canine imaging and radiation therapy trial
CT	Computed tomography
Cu-ATSM	Copper(II)-diacetyl-bis(N4-methylthiosemicarbazone)
DPV	Dose painted volume (GTV + 2mm)
DVH	Dose volume histogram
FAZA	^{18}F-fluoroazomycin arabinoside
FDG	2-deoxy-2-[^{18}F]fluoro-D-glucose
FET	^{18}F-fluoro-ethyl-tyrosine
FLT	3'-deoxy-3'-^{18}F-fluorothymidine
FMISO	^{18}F-fluoromisonidazole
GBM	Glioblastoma multiforme
GTV	Gross tumor volume
HN	Head-and-neck
HNSCC	Head-and-neck squamous cell carcinoma
IMRT	Intensity-modulated radiation therapy
MRI	Magnetic resonance imaging
NTCP	Normal tissue complication probability
OS	Overall survival
PDVH	Prescription dose volume histograms
PET	Positron emission tomography
PFS	Progression-free survival

PTV	Planning target volume
pO_2	Partial pressure of oxygen
PTV	Planning target volume
R	Pearson correlation coefficient
R^2	Coefficient of determination
RECIST	Response evaluation criteria in solid tumors
SUV	Standardized uptake value
SUV_{max}	Maximum standardized uptake value
SUV_{mean}	Mean standardized uptake value
SUV_{peak}	Peak standardized uptake value
SUV_{SD}	Standard deviation of standardized uptake values
SUV_{total}	Sum of standardized uptake values
TCP	Tumor control probability model
ρ	Spearman correlation coefficient
$\rho_{Cu\text{-}ATSM}$	Voxel spearman correlation between pre- and mid-treatment Cu-ATSM SUV distributions
ρ_{FLT}	Voxel spearman correlation between pre- and mid-treatment FLT SUV distributions

List of figures

Acknowledgments

This dissertation work would not have been possible without the efforts of the many people who worked to collect the data — namely, the "CDP Group". This includes Matt La Fontaine, Stephen Bowen, Ngoneh Jallow, Vikram Adhikarla, Peter Scully, Michael Deveau (although our time did not overlap), Stephanie Harmon, and support from the Veterinary Medicine Teaching Hospital, including Lisa Forrest, Margaret Henzler, Lyndsay Kubicek, and Pamela White. I also want to express gratitude for the years of guidance, support, and encouragement I received from my research group, my advisor, and my family.

Abstract

In biologically-conformal radiation therapy, or dose painting, functional imaging is used to define biological targets for radiotherapy dose escalation. There is still much uncertainty about which imaging target is optimal for dose painting, and how dose should be prescribed inside the target volume. The goal of this dissertation was to investigate and characterize the properties of different biological imaging methods that make them good or poor candidates to serve as dose painting targets, and to evaluate how dose is likely to be prescribed to target volumes. Using spontaneous sinonasal tumors in canines treated with radiation therapy as research models, we related FDG, FLT, and Cu-ATSM PET uptake—surrogate measures of metabolism, proliferation, and hypoxia, respectively—to radiation resistance using outcome analysis and voxel-wise spatial analysis. We also investigated the similarities and spatio-temporal stability of the different tracer uptake patterns. Overall, we found that FLT-based biomarkers, especially those acquired during the course of radiation therapy, were the best biomarkers at predicting outcome following radiation therapy. Using spatial analysis, we found that all tracers had comparable performances in identifying resistant tumor subvolumes, and that there was large interpatient heterogeneity in how well PET tracer distributions could identify resistant subvolumes. We also demonstrated that spatial distributions of Cu-ATSM and FLT uptake measured during therapy were very similar to those measured at baseline, indicating FLT and Cu-ATSM PET as spatially-robust targets for dose painting. Finally, we demonstrate how FDG, FLT, and Cu-ATSM dose painting prescriptions are likely to be applied in human head-and-neck tumors, and confirm the feasibility of accurately delivering dose painting plans with tomotherapy. Overall, we did not find a single imaging method that stood out as the most promising target for dose painting. Rather, all tracers demonstrated evidence both for and against their use as dose painting targets. However, through these studies, we now have a greater understanding of the characteristics and limitations of dose painting according to different biological targets, which can help guide the development of future dose painting studies.

1. Introduction

Biologically-conformal radiation therapy, or dose painting, is an emerging paradigm in radiation therapy in which dose prescriptions are tailored to match underlying biological heterogeneities within tumors. Biological imaging of solid tumors, such as with positron emission tomography (PET), is used to define biological imaging targets for radiation dose escalation. The overall objective of this dissertation was to evaluate the properties of several potential imaging-based targets and to determine their suitability as dose painting targets.

This chapter introduces the basic principles of dose painting, and describes why dose painting is anticipated to eventually supplant traditional intensity-modulated radiation therapy (IMRT) for many tumor sites. The theoretical basis for dose painting will be described in the context of tumor modeling studies, and results from experimental dose painting trials in humans will be discussed. Additionally, the remaining uncertainties in dose painting will be described, followed by a description of an experimental trial in canines that the majority of this dissertation work will be drawn from. Finally, the specific aims of this thesis will be explained, followed by an outline of the remainder of the dissertation.

1.1. Rationale for dose painting

Prescriptions of uniform dose to tumor volumes are the current standard for radiation therapy. Typically, tumor volumes are manually delineated by physicians according to computed tomography (CT) images, and then the entire tumor volume is prescribed to a single dose level. For IMRT, inverse treatment planning software is then used to optimize the weights of different radiation fields such that uniformity of the physical dose distribution is maximized inside the tumor volume (plus margins), while dose to the surrounding normal tissue is minimized. Overall, a great deal of effort is expended to ensure uniform dose coverage of target volumes. The method of prescribing uniform doses to target volumes is currently employed in nearly all radiation oncology facilities, yet the method fails to account for the fact that tumors are spatially heterogeneous in composition (*1*). In fact, it has become apparent over the last

few decades that tumors are far from homogeneous, exhibiting biological complexities and heterogeneities matching, or even exceeding, that of normal tissue (*1-2*). Even multiple biopsies from the same tumor can differ substantially in both phenotype and genotype (*3-4*).

Spatial variations in biological properties such as cell cycle phase, proliferation rates, acidity, oxygenation, and repair capabilities can result in heterogeneous patterns of radiosensitivity (*5*). Even small niches of resistant tumor cells can prove detrimental to radiation therapy plans, as only a small number of surviving cells may be necessary to repopulate a tumor (*5*). This principle is best exemplified by the property of tumor hypoxia: hypoxic tumor cells can require up to 3 times the dose as normal tumor cells for equivalent cell kill (*5*). Hypoxic cells generally make up only a small portion of a tumor—about 15% on average (*6*)—but can be seriously detrimental to patient outcome (*7*). Ideally, dose prescriptions to tumors would be high enough to control even the most radioresistant cells, but normal tissue tolerances do not allow for such prescriptions. Clearly, targeting the most radioresistant subregions of tumors would be a more efficient method of killing tumors than the method of treating tumors as having uniform biological composition. In the past, however, accurately identifying resistant tumor subpopulation *in vivo* was not possible, and therefore uniform dose prescriptions have remained the clinical standard.

Recent advances in molecular imaging may allow for discernment of spatial variations in radiosensitivity throughout tumor volumes. When only CT images of tumors are used for treatment planning purposes, spatial heterogeneities in radiosensitivity cannot be resolved. Under these circumstances (which are standard in current clinical practice) uniform dose prescriptions are indeed best, as dose inhomogeneities in target volumes would just as likely be distributed to sensitive regions as to resistance regions, resulting in an overall inferior treatment (*8*). However, supplementing anatomical imaging with molecular imaging, such as positron emission tomography (PET), may help uncover spatial patterns of radiosensitivity, and identify targets for dose escalation. For example, studies of 2-deoxy-2-[^{18}F]fluoro-D-glucose (FDG) PET in lung tumors suggest that tumor subregions with affinity for FDG might be more radioresistant than regions with little FDG uptake (*9*). PET images can be fused together

with treatment planning CT images, and regions of elevated FDG uptake could then be targeted for dose escalation during treatment planning.

In addition to insufficiently addressing tumor heterogeneity, current uniform dose prescriptions appear to be too low for controlling certain tumor types. In lung tumors, for example, biologically effective doses (BED) of greater than 100 Gy are likely needed achieve 70%–90% local control rates (*10-11*), but standard treatment schedules for lung cancer often include prescriptions of only 60-70 Gy in 2 Gy fractions; this results in BED of only 70-85 Gy (*12*). Any increase in total tumor dose, however, is undermined by a simultaneous increase in normal tissue complications, which may result in overall inferior outcome (*13*). Consequently, local recurrences most often occur at primary tumor sites—the regions receiving the highest dose—highlighting the need for higher dose prescriptions (*14-17*). To counteract this problem, simultaneous integrated boosts (SIBs) have been increasingly used in treatment planning protocols, but these boosts are only based on past clinical experience and not on patient-specific biology. Furthermore, it is unlikely that the entire tumor volume needs to be boosted to higher dose levels. Rather, it is probable that only small niches of radioresistance within the tumor actually require significant dose escalation.

The practice of biologically-conformal radiation therapy, or dose painting, attempts to address two factors that render uniform dose prescriptions as insufficient: spatial heterogeneities in tumor radiosensitivity, and insufficient tumor dose levels. In dose painting, non-uniform dose is prescribed to a tumor volume, tailored to match the spatial heterogeneity of an underlying biological property linked with radioresistance (see Figure 1.1) (*18*). This enables higher doses to be delivered to tumor subregions of suspected radioresistance while decreasing dose to radiosensitive tumor subregions, and maintaining or even reducing normal tissue dose. The basic principles for dose painting were proposed over a decade ago

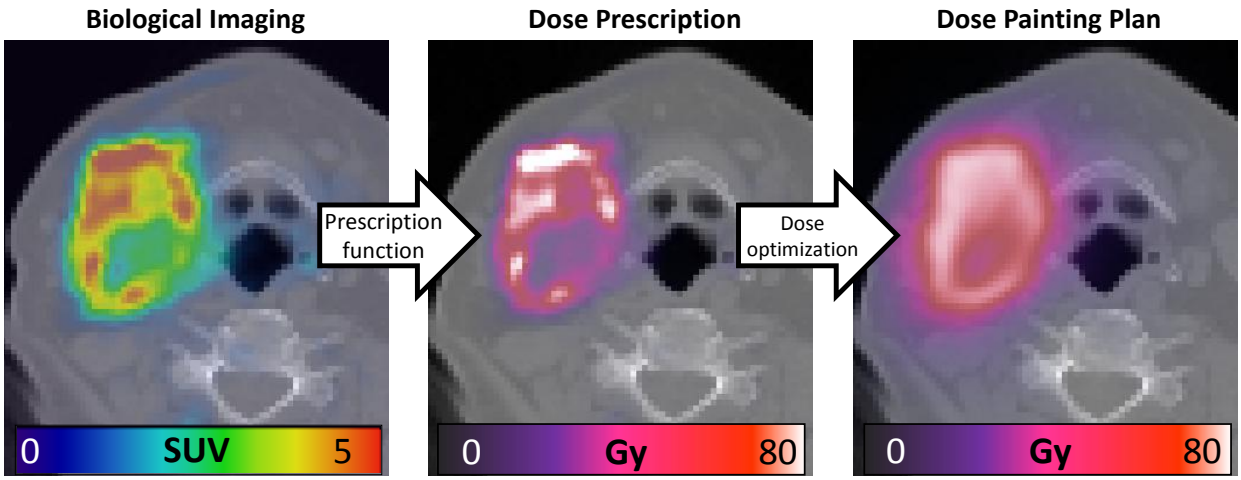

Figure 1.1. An example of how dose painting can be implemented in a head-and-neck tumor.

(*18-19*), and numerous modeling studies have subsequently predicted its superiority over uniform-dose prescriptions (see Table 1.1).

1.2. Modeling and planning studies

Early investigators used tumor control probability (TCP) models based on survival of clonogenic cells to evaluate the effects of dose inhomogeneities, and showed that for a fixed mean tumor dose, uniform dose distributions maximize TCP for tumors of uniform radiosensitivity (*20-21*). In 1987, Brahme and Ågren used a single-hit multi-target tumor cell model to determine the optimal physical dose distribution for eradicating tumors with heterogeneous cell populations (*19*). Not surprisingly, they found that heterogeneous tumors are best treated with heterogeneous dose distributions. They even speculated that molecular imaging may one day provide the means to "allow a more specific localization of different types of human tumor cells," and even recognized that perfusion and cell density effects would need to be corrected for in molecular images. At the time, however, available imaging methods were not able to distinguish resistant tumor subpopulations from sensitive subpopulations, and, consequently, uniform dose prescriptions were adopted as the clinical standard, which has persisted until now.

In 2000, Clifton Ling and colleagues introduced the concept of biological target volumes (*18*). They proposed that functional imaging, such as PET or magnetic resonance imaging (MRI), could be

used to define biological subvolumes with radiosensitivity values that differed from the rest of the tumor. These biological target volumes could then be prescribed more or less dose, depending on their radiosensitivity values. These principles have since been extrapolated to the voxel level, wherein individual voxel radiosensitivity values—representing averages of the voxel's cellular population—could be extracted from voxel imaging values (eg, from PET imaging), and each voxel could then receive its own unique dose prescription. Voxel-based dose painting is often called dose painting by numbers (*22*).

The superiority of non-uniform dose prescriptions over uniform dose prescriptions for heterogeneous tumors has been demonstrated in numerous modeling studies. Popple *et al*. and Yang *et al.* used TCP modeling to show that non-uniform dose distributions result in greater tumor control in conditions of spatially-varying oxygenation or radiosensitivity (*23-24*). Other similar modeling studies are listed in Table 1.1. Many planning studies have demonstrated the feasibility of using treatment planning software—both commercial and customized treatment planning software—to create treatment plans consisting of non-uniform dose distributions derived from functional images. This has been demonstrated for a variety of imaging methods, including FDG PET (*25*), 3'-deoxy-3'-^{18}F-fluorothymidine (FLT) PET (*26*), copper(II)-diacetyl-bis(N4-methylthiosemicarbazone) (Cu-ATSM) PET (*27*), ^{18}F-fluoromisonidazole (FMISO) PET (*28*), ^{18}F-fluoro-ethyl-tyrosine (FET) PET (*29*), ^{11}C-choline PET (*30*), and for DCE-MRI parametric maps (*31*). All of the modeling and planning studies listed in Table 1.1 are practically unanimous in their conclusions: dose painting is not only feasible, but would increase tumor control rates if radiosensitivity levels could be accurately measured via imaging. Furthermore, tumor modeling predicts that voxel-based dose painting would be superior to uniform boosts to biological target volumes *if* radiosensitivity values can be accurately measured at the voxel level (*23, 32*).

Table 1.1. Dose painting studies.

REFERENCE	DESCRIPTION
PLANNING & MODELING STUDIES	
Brahme A, et al. 1987 (*19*)	Modeling, non-uniform dose
Webb S, et al. 1993 (*8*)	Modeling, non-uniform dose
Stavreva N, et al. 1996 (*33*)	Modeling, non-uniform dose
Chao KS, et al. 2001 (*35*)	Planning, Cu-ATSM boost
Popple RA, et al. 2002 (*24*)	Modeling, hypoxia, TCP
Alber M, et al. 2003 (*38*)	Planning, optimization
Brahme A, et al. 2003 (*40*)	Modeling, response-based DP
Solberg T, et al. 2004 (*25*)	Planning, FDG boost, feasibility
Das S, et al. 2004 (*43*)	Planning, feasibility, SPECT, EUD
Yang Y, et al. 2005 (*23*)	Modeling, TCP
Schwartz D, et al. 2005 (*46*)	Planning, FDG boost
Malinen E, et al. 2006 (*31*)	Planning, DCE-MRI, TCP
Vanderstraeten B, et al. 2006 (*49*)	Planning, FDG boost, optimization
Vanderstraeten B, et al. 2006 (*51*)	Planning, FDG, DPBN
Sovik A. et al. 2007 (*53*)	Planning/modeling, hypoxia, TCP
Sovik A, et al. 2007 (*55*)	Planning/modeling, DCE-MRI, TCP/NTCP
Thorwarth D, et al. 2007 (*28*)	Planning, FDG & FMISO, TCP
Chen G, et al. 2007 (*56*)	Planning, optimization
Thorwarth D, et al. 2008 (*58*)	Planning, FMISO, IMRT vs IMPT vs Tomo
Gillham C, et al. 2008 (*60*)	Planning, adaptive FDG
Lee N, et al. 2008 (*62*)	Planning, FMISO boost, feasibility
Lin Z, et al. 2008 (*64*)	Planning, FMISO boost, test-retest
Kim Y, et al. 2008 (*66*)	Modeling, prescription, TCP/NTCP
Flynn R, et al. 2008 (*68*)	Planning, IMRT vs IMPT, Cu-ATSM
Petit SF, et al. 2009 (*70*)	Planning, FDG, prescription
Petit SF, et al. 2009 (*72*)	Planning/modeling, hypoxia
Feng M, et al. 2009 (*74*)	Planning, adaptive FDG
Bowen S, et al. 2009 (*75*)	Planning, Cu-ATSM, prescription function
South C, et al. 2009 (*76*)	Modeling, TCP
Jingu K, et al. 2010 (*78*)	Planning/modeling, FDG, NTCP
Kissick M, et al. 2010 (*80*)	Planning, motion
Deveau M, et al. 2010 (*27*)	Planning, feasibility, tomotherapy
Korreman S, et al. 2010 (*81*)	Planning, feasibility, VMAT
Kim Y, et al. 2010 (*82*)	Modeling, prescription, TCP/NTCP
Rickhey M, et al. 2010 (*83*)	Planning, IMPT, FET, feasibility
Le, Maitre A, et al. 2010 (*84*)	Modeling, TCP, FDG + FMISO
Troost E, et al. 2010 (*26*)	Planning, FLT response
Niyazi M, et al. 2010 (*30*)	Planning, TCP, choline, prostate
Shi K, et al. 2011 (*85*)	Planning, optimization, FMISO
Meijer G, et al. 2011 (*86*)	Planning, FDG, DPBN vs boost
Aristophanous M, et al. 2011 (*87*)	Planning, 4D FDG
Hendrickson K, et al. 2011 (*88*)	Planning/modeling, FMISO boost, TCP
Rodal J, et al. 2011 (*89*)	Planning, dosimetry
Witte M, et al. 2011 (*90*)	Planning, optimization
Hardcastle N, et al. 2011 (*91*)	Planning, IMRT vs VMAT, NTCP
Chang JH, et al. 2012 (*92*)	Planning, ^{11}C-choline, TCP
Dirscherl T, et al. 2012 (*93*)	Planning, TCP-based, 18F-choline
Toma-Dasu I, et al. 2012 (*94*)	Planning, FMISO, feasibility
Bowen S, et al. 2012 (*95*)	FDG, FLT, Cu-ATSM, prescription
Bender E. 2012 (*32*)	Modeling, optimization, prescription
Hardcastle N, et al. 2012 (*96*)	Modeling, optimization, prescription
Chang JH, et al. 2013 (*97*)	Planning/modeling, FMISO, TCP/NTCP
Rusten E, et al. 2013 (*98*)	Planning, dynamic FDG boost
Teoh M, et al. 2013 (*99*)	Planning, FDG boost, IMRT vs VMAT
Vogelius I, et al. 2013 (*100*)	Planning/modeling, prescription, TCP
Hakansson, K, et al. 2014 (*101*)	Planning, optimization
Olteanu, L, et al. 2014 (*102*)	Planning, dosimetry
Park, Y, et al. 2014 (*103*)	Planning , optimization
Alfonso, J et al. 2014 (*104*)	Modeling, CSCs

REFERENCE	DESCRIPTION
REVIEW & CONCEPT PAPERS	
Ling C, et al. 2000 (*18*)	Review/concept
Bentzen S, et al. 2005 (*22*)	Review/concept
Galvin J, et al. 2007 (*34*)	Review
Bentzen S, et al. 2008 (*36*)	Review/concept
Lawrence R, et al. 2008 (*37*)	Review
Sovik A, et al. 2009 (*39*)	Review
Lambin P, et al. 2010 (*41*)	Review/concept, NSCLC
Thorwarth D, et al. 2010 (*42*)	Review, hypoxia
Thorwarth D, et al. 2010 (*44*)	Review/concept
Supiot S, et al. 2010 (*45*)	Review
Bentzen S, et al. 2011 (*47*)	Review/concept
van der Heide, et al. 2012 (*48*)	Review, MRI
Gregoire V, et al. 2012 (*50*)	Review/concept
Hoeben B, et al. 2013 (*52*)	Review, HN, adaptive
Geets X, et al. 2013 (*54*)	Review, hypoxia
DOSE PAINTING CLINICAL TRIALS	
Douglas J., et al. 2006 (*57*)	Mid-tx FDG, GBM, 40 pts
Madani I, et al. 2007 (*59*)	FDG boost, HN, 41 pts
Miwa K, et al. 2008 (*61*)	^{11}C-MET boost,, GBM, 3 pts
Pinkawa M, et al. 2010 (*63*)	^{18}F-choline, prostate, 66 pts
Duprez F et al. 2011 (*65*) &... Madani I, et al. 2011 (*67*)	Adaptive FDG DPBN, HN, 21 pts
Fodor A, et al. 2011 (*69*)	FDG boost, pleural mesothelioma, 12 pts
Piroth M, et al. 2012 (*71*)	FET boost, GBM, 22 pts
Berwouts D, et al. 2013 (*73*)	Adaptive FDG DPBN, HN, 10 pts,
FUTURE & ONGOING CLINICAL TRIALS	
Hamming-Vrieze, O. (PI) (*77*)	FDG boost, HN, 268 pts (NCT01504815)
De Ruysscher D. (PI) (*79*)	FDG boost, NSCLC, 106 pts (NCT01024829),
Kong S (PI)	Mid-tx FDG boost, NSCLC, 42 pts (RTOG 1106)
Vera P (PI)	FMISO boost, NSCLC, 75 pts (NCT01576796)
Ghent Univ. (multiple studies)	FDG, HN (NCT01427010, NCT01341535, NCT01287390)
Xiaolong F (PI)	FDG boost, esophageal SCC, 40 pts (NCT01843049)

1.3. Clinical studies

Few clinical trials have actually treated patients with dose painting plans (see Table 1.1). In a trial with glioblastoma multiforme (GBM) patients undergoing radiation therapy, Douglas and colleagues were the first to adapt physical dose distributions during therapy to match mid-treatment FDG PET uptake patterns and deliver additional boosts to those regions (*57*). They treated MRI-defined target volumes to 59.4 Gy in 1.8 Gy fractions, and then treated residual FDG-avid volumes at mid-treatment (defined after 45-50.4 Gy) with an additional 20 Gy in 10 fractions, for a total of 79.4 Gy. In 40 patients, they observed no significant differences in clinical outcome when compared to a historical control.

Researchers at Ghent University have run a series of dose painting clinical trials in patients with head-and-neck (HN) tumors investigating FDG PET as a dose painting target. In their first published study, 41 HN cancer patients received IMRT between 2003 and 2005, with 69 Gy prescribed to the macroscopic tumor (*59*). The PET-avid regions were then boosted uniformly to either 72.5 Gy or 77.5 Gy. The trial was halted early due a treatment-related death, but a comparison of the two boost arms found that the higher boost (77.5 Gy) actually resulted in worse overall survival than the lower boost (72.5 Gy) (P=0.06). This trial was followed up by another dose painting trail in HN cancer patients wherein voxel doses were prescribed according to their FDG uptake values (ie, dose painting by numbers), and then adapted during therapy to match mid-treatment FDG PET images (*65*). In their treatment protocol, a linear prescription function was used to convert PET voxel intensity values into voxel doses (voxel doses ranged between 72.5 Gy to 95.9 Gy), re-imaging and re-planning occurred after 10 fractions, and then uniform dose was prescribed to tumors after 20 fractions. The study included two treatment arms: one arm with a median dose of 80.9 Gy to the target volume (N=7), and the other arm with a median dose of 85.9 Gy (N=14). Due to the development of mucosal ulcers in 36% of the patients (N=5) in the higher dose group, they concluded that 80.9 Gy was the maximum tolerated dose (*67*). They also conducted a third trial with 10 HN cancer patients, and demonstrated the feasibility of performing three-phase

adaptive dose painting in HN tumors using longitudinal FDG imaging (*73*). They are currently performing several more dose painting trials in HN cancer patients (see Table 1.1).

Dose painting studies have also been conducted in other tumor sites. Miwa and colleagues demonstrated the feasibility of boosting regions of high ^{11}C-methionine PET uptake in 3 patients with GBM tumors (*61*). Pinkawa and colleagues performed simultaneous integrated boosts of 4 Gy (from 76 Gy to 80 Gy) to the regions of elevated ^{18}F-choline PET uptake in 66 patients with prostate tumors (*63, 105*). Piroth and colleagues boosted high ^{18}F-fluoro-ethyl-tyrosine (FET) PET uptake regions by 12 Gy (from 60 Gy to 72 Gy) in 22 GBM patients (*71*). Fodor and colleagues uniformly boosted high FDG PET regions by 6.5 Gy (from 56 Gy to 62.5 Gy) in 12 malignant pleural mesothelioma patients (*69*). Preliminary results from an ongoing dose painting trial have been reported by van Elmpt *et al.*, in which 20 lung cancer patients were randomized between a control treatment arm and an FDG PET boost arm, both of which were boosted in an isotoxic manner (ie, until normal tissue dose constraints were met) (*79*). For the control arm, the boost volume was defined as the entire primary tumor, and for the experimental arm, the boost volume was defined as the region inside the 50% FDG SUV_{max} isocontour. Patient outcome and toxicities have yet to be reported.

1.4. Uncertainties in dose painting

Despite the multitude of modeling and planning studies affirming dose painting's advantage over traditional radiation therapy, the few clinical trials that have been conducted have been modest in their boosting technique and are often small in sample size. This is likely due to the many uncertainties—biological and technical—associated with dose painting, which collectively make dose painting a potentially risky method. Many of dose painting's technical uncertainties can likely be overcome, such as motion (*80*), setup uncertainties (*90, 106*), imaging uncertainties (*107*), and treatment planning (*27*) . However, the main uncertainties hindering dose painting are *what* to target, and *how*. Targeting the wrong part of the tumor (ie, a sensitive region) at the expense of a resistant region would most certainly be inferior to standard uniform-dose prescriptions. Furthermore, it is uncertain how high the dose

modulations should be within tumor volumes (ie, how much higher should the maximum voxel dose be than the minimum voxel dose?), as this question is inherently related to how confident we are in assessing *what* to target. These biological-based uncertainties are currently the main obstacles for dose painting.

1.4.1. Uncertainty in target definition

Dose painting requires an imaging target, from which boost dose prescriptions can be derived. Currently, it is unknown which imaging target is optimal for dose painting. Many researchers have proposed different biological targets for dose painting, including PET tracer uptake distributions and MRI parametric maps (*22, 44, 47*). For dose painting to be successful, the imaging target needs to be strongly correlated with spatial patterns of resistance. Three of the most commonly proposed targets in dose painting are tumor hypoxia, cellular proliferation, and glucose metabolism, all three of which were investigated as part of this dissertation work.

Glucose metabolism, as assessed by FDG PET, is the most commonly considered candidate target for dose painting. FDG PET has proven to be valuable in lesion detection, tumor staging, and tumor segmentation (*108*) , and has been used in most of the dose painting clinical trials (*57, 59, 65, 73, 79*). Furthermore, FDG is the most clinically-used PET radiotracer. Consequently, empirical evidence has accumulated suggesting FDG's potential as an effective dose painting target. For example, post-treatment residual tumor is most often located in regions with the highest pre-treatment FDG uptake for several tumor sites (*9, 14, 95, 100, 109*). On the other hand, FDG uptake is influenced by a variety of biological properties, including inflammation, proliferation, hypoxia, cell density, and perfusion (*110-111*), some of which can decrease its utility as a dose painting target.

Another promising PET tracer for oncology is FLT. FLT PET is a marker of tumor proliferation, and has been shown to have better specificity for tumor disease than FDG PET, primarily due to its uptake being independent of inflammation (*112-113*). Specifically, FLT is imported into the cell via thymidine kinase 1 activity, which is active during the S phase of the cell cycle. FLT uptake therefore

represents the fraction of cells in S phase (*114*). However, the relationship between proliferation and radioresistance is not very clear. While highly proliferative tissues were associated with increased radiosensitivity as early as 1906 (*115*), this relationship is not always observed in tumors. For example, a meta analysis of 476 patients' tumor biopsies prior to radiation therapy found no significant association between potential cell doubling times and patient survival (*116*). Despite the ambiguous relationship between pre-treatment proliferation rates and patient outcome, accelerated repopulation of surviving cancer cells *during* therapy has been shown to influence treatment outcome (*117*). In addition, drastic changes in uptake of FLT have been observed in tumors after the onset of radiotherapy (*118-119*). This has created interest in using changes in FLT uptake from pre- to mid-therapy as an early response indicator (*26, 120-121*). Extending this idea to the voxel level, the change in a voxel's FLT uptake during therapy could be indicative of the voxel's response to therapy, so that maps of voxel responses could then be used to define biological targets for dose painting.

The case for tumor hypoxia as a dose painting target is well established in literature. In cultured cells and murine cancer models, hypoxic tumor cells require 2-3 times the dose as normoxic cells for equivalent cell kill (*5*). Using oxygen electrode measurements in human tumors, oxygen partial pressures (pO2) within tumors prior to radiation therapy have been shown to be prognostic: tumors with $pO2 \leq 2.5$ mmHg have significantly worse loco-regional control that those with $pO2 > 2.5$ mmHg (*7, 122-123*). The molecular mechanisms that cause oxygen to act as a radiosensitizer are not entirely understood. It is assumed that molecular oxygen combines with free radicals resulting from ionizations, creating a reactive species that can cause irreparable damage to DNA (*124*). It is also unclear the distinction between acute hypoxia and chronic hypoxia, as studies have found both exist within tumors (*125-126*). Tumor hypoxia can be imaged *in vivo* with hypoxia radiotracers such as Cu-ATSM (*127*) or FMISO (*128*), among others (*129*). In fact, Cu-ATSM PET imaging has been shown to be prognostic following radiation therapy for HN tumors (*130-131*), as well as for cervical (*132-133*), lung (*134*), and rectal (*135*) tumors.

Other dose painting targets have been proposed. These include diffusion-weighted MRI (*136*), epidermal growth factor receptor (EGFR) imaging with radiolabeled monoclonal antibodies (*41*), and amino acid imaging (*71*). Brahme proposed using changes in biological imaging patterns from pre-treatment to mid-treatment to guide target volume definition (*40*). Given the numerous potential imaging targets for dose painting, and the heavy reliance of dose painting on the efficacy its imaging target, imaging target uncertainty is perhaps the largest hindrance to the clinical success of dose painting.

1.4.2. Uncertainty in dose prescriptions

Even with well-defined dose painting targets, it is unclear how dose should be prescribed to target volumes. For uniform boosts to biological subvolumes, it is uncertain the degree to which target subvolumes should be boosted above the baseline tumor dose. For voxel-based dose painting, a prescription function is required to convert voxel image intensity values into voxel dose prescriptions (*75*). The prescription function embodies the relationship between the imaging method and the underlying biological target, and the relationship between the biological target and radioresistance. Clearly, the prescription function is strongly dependent on the imaging method, and represents a very complex relationship. Consequently, there is much uncertainty about what the best prescription function for voxel-based dose painting would be. Several methods have been proposed, including prescription functions based on TCP (*23*), sigmoidal functions (*75*), and linear functions (*51*). At this time, only linear prescription functions have been used in clinical studies (*65*, *73*, *79*).

A further prescription uncertainty is how to adapt dose prescriptions to biological differences between patients (ie, *inter*patient variability). For example, would certain biological properties be more effective as targets in some patients than others? Would certain patients benefit from hypoxia-based dose painting, while other patients would benefit more from proliferation-based dose painting? And should all patients receive the same maximum voxel dose, the same minimum voxel dose, or the same integral/mean dose? These questions are difficult to answer, and may not be answered until after extensive clinical

experience. Clearly, interpatient variability could impede the development of and complicate the evaluation of different prescription methods in different clinical trials.

1.5. Canine imaging and radiation therapy (CIRT) trial

The goal of this dissertation work is to address some of the uncertainties regarding target selection for dose painting. The large majority of this dissertation work will come from the canine imaging and radiation therapy (CIRT) trial. Detailed descriptions of the CIRT trial can be found in previous publications (*95, 137-139*). Canine patients with spontaneous sinonasal tumors of stage I-III were eligible for the study, baring distant metastases or brain involvement. Patients received IMRT via tomotherapy with curative intent. The CIRT study included two treatment arms. Arm A received the standard-of-care prescription at the University of Wisconsin Veterinary Teaching Hospital, including 10 fractions of 4.2 Gy to the planning target volume (PTV). Arm B was the boost cohort, which included 10 fractions of 4.2 Gy to the PTV with an integrated boost of 0.8 Gy per fraction to the gross tumor volume (GTV), for a total of 50 Gy to the GTV. 10 patients completed treatment in arm A and 12 patients completed treatment in arm B. Patient characteristics are listed in Table 1.2.

Table 1.2. Patient characteristics from the CIRT trial

		Number of patients
Histology	Adenocarcinoma	13
	Squamous cell carcinoma	1
	Chondrosarcoma	7
	Osteosarcoma	1
Age	0-5	6
	5-10	8
	11+	8
Starting weight (kg)	5-10	2
	11-20	3
	21-30	8
	31+	9
Sex	Female	11
	Male	11
Treatment	Boost (50 Gy)	12
	Standard-of-care (42 Gy)	10
Stage (*140*)	D1	3
	D2	12
	D3	7

The treatment and imaging schedule is diagramed in Figure 1.2. Patients had pre-treatment [^{18}F]FDG, [^{18}F]FLT , and [^{61}Cu]Cu-ATSM PET/CT scans on consecutive days beginning 3 days before the onset of therapy. Patients received a second FLT PET/CT scan after two fractions of IMRT (8.4 or 10 Gy) and a weekend break. Patients received a second Cu-ATSM PET/CT scan following the third fraction of IMRT (12.6 or 15 Gy). One patient missed the mid-treatment FLT scan due to equipment failure. Patients were injected with 150-370 MBq of tracer. After injection, patients were kept in a kennel to limit physical activity. PET/CT scans were acquired on a Discovery VCT (GE Healthcare, Waukesha, WI) scanner. FDG and Cu-ATSM PET scans were acquired 60 minutes and 180 minutes post-injection, respectively; both were 20-minute 3D static acquisitions over a single 15 cm bed position. FLT scans were 90-minute 3D dynamic acquisitions over a single 15 cm bed position. Patients were anesthetized during imaging and treatment sessions with an initial propofol bolus injection, and then maintained on isoflurane inhalation plus 100% oxygen. Emission data were attenuation corrected and reconstructed using ordered subset expectation maximization (2 iterations, 35 subsets, and 3 mm postfiltering). The image grid was 256×256×47 with 2.0×2.0×3.3 mm^3 voxel sizes. Voxel activity measurements were

converted to standardized uptake values (SUVs) for analysis. For FLT scans, SUVs were calculated by averaging frames from 60–90 minutes. To achieve reproducible positioning across PET/CT scans and IMRT treatment sessions, patients' maxillae were positioned into custom dental molds that were affixed to the scanner and treatment couches, and patients' bodies were immobilized with vacuum mattresses, as shown in Figure 1.3 (*137*).

Following treatment, patients were scheduled for follow-up FDG PET/CT scans at 3 and 6 months. Patients without progressive disease within the first 6 months received an additional CT scan at 9 months, and an additional FDG PET/CT scan whenever they presented with clinical signs suspicious of recurrence (eg, epistaxis).

For data analysis, veterinarians contoured gross tumor volumes (GTVs) and planning target volumes (PTVs) based on CT images, which were then propagated to PET images through registration (either rigid or deformable, depending on the study) and resampling. The PTV included the GTV, plus regions of suspected microscopic extensions. For each PET image, SUV metrics were calculated within the GTV, including the maximum voxel SUV in the GTV (SUV_{max}), the mean SUV of a 1 cm^3 sphere centered at SUV_{max} (SUV_{peak}), the mean SUV of the GTV (SUV_{mean}), and the total summed SUV in the GTV (SUV_{total}).

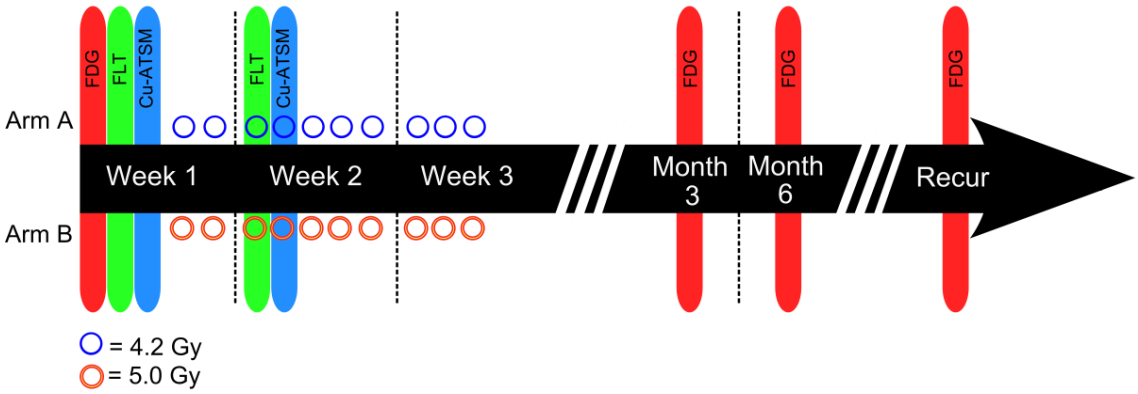

Figure 1.2. Imaging and treatment schedules for treatment arms A and B of the CIRT trial

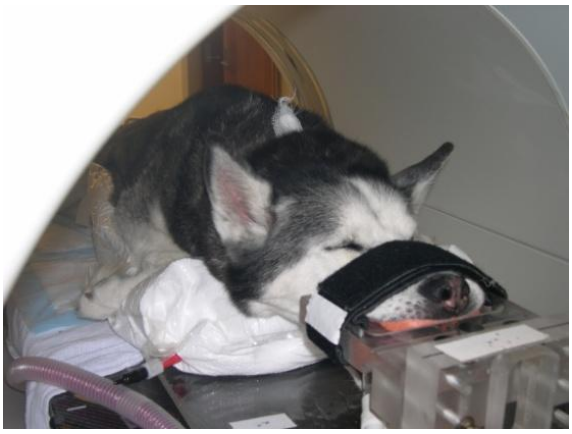

Figure 1.3. Canine patients were immobilized during imaging and radiation therapy using a custom-built bite block with patient-specific dental molds and vacuum mattresses.

1.6. Specific aims and dissertation outline

The objective of this dissertation was to characterize and address several of the limitations and uncertainties currently facing dose painting. As a primary uncertainty in dose painting is imaging target definition, we evaluated the properties of several imaging targets —glucose metabolism, proliferation, and hypoxia— as they relate to dose painting target definition. The work in this dissertation is unique in that the data from the CIRT trial is both rich (eg, high quality imaging and outcome data) and broad (eg, multi-tracer PET imaging), which allowed us to address several questions about target definition that have not been addressed before, and required the development of unique methods of data analysis. This dissertation is split into three specific aims, with respective sub-aims.

Specific Aim 1: To evaluate the suitability of FDG, FLT, and Cu-ATSM PET for target definition in biologically-conformal radiation therapy

Sub-aim 1a: To assess the spatio-temporal stability of FLT and Cu-ATSM PET distributions in tumors during radiotherapy (*Chapter 2*)

Sub-aim 1b: To evaluate the robustness of PET-based target definition in two tumor histologies: sarcomas and carcinomas (*Chapter 3*)

Sub-aim 1c: To characterize the spatial relationships between regional recurrence and FDG, FLT, and Cu-ATSM PET distributions (*Chapter 4*)

Specific Aim 2: To assess how different quantitative imaging biomarkers relate to clinical outcome for canine patients following radiation therapy

Sub-aim 2a: To assess univariable relationships between imaging biomarkers and progression-free survival (*Chapter 5*)

Sub-aim 2b: Using multivariate analysis, assess each biomarkers relative contribution in predicting progression free survival (*Chapter 5*)

Specific Aim 3: To investigate the feasibility of creating and delivering PET-based dose painting plans

Sub-aim 3a: To characterize how voxel-based dose painting prescriptions are likely to be distributed in human head-and-neck tumors (*Chapter 6*)

Sub-aim 3b: To evaluate the dosimetric accuracy of tomotherapy-delivered dose painting plans (*Chapter 6*)

The remainder of this dissertation is organized as follows: Chapter 2 characterizes the spatio-temporal stability of FLT and Cu-ATSM PET distributions in canine tumors during radiation therapy, in order to evaluate if FLT and Cu-ATSM PET are spatially robust targets for dose escalation (*139*). Chapter 3 characterizes how similar or dissimilar pre-treatment FDG, FLT, and Cu-ATSM PET distributions were in canine tumors according to the tumor's histologic tumor type (sarcoma vs. carcinoma), to assess how dose painting plans change according to different biological targets (*141*). Chapter 4 describes the degree to which PET imaging can predict the location of tumor recurrence following radiation therapy using voxel-based regression methods. Chapter 5 contains survival analysis results for the CIRT trial, identifying the best imaging biomarkers of resistance to radiation therapy. Chapter 6 describes the

feasibility of dose painting; specifically, it describes how FDG, FLT, and Cu-ATSM dose painting prescriptions are likely to be distributed in human HN tumors, and demonstrates how accurately we can deliver simulated dose painting plans with tomotherapy. Finally, Chapter 7 summarizes the significant findings of this dissertation, and discusses how this dissertation work contributes to the advancement of dose painting.

2. Spatio-temporal stability of Cu-ATSM and FLT PET distributions during radiation therapy

This chapter addresses Specific Aim 1 of the dissertation, which is to evaluate the characteristics of different PET radiotracers that make them good or poor candidates as dose painting targets. Specifically, this chapter discusses the how Cu-ATSM and FLT PET distributions change in canine tumors during the course of radiation therapy, both in terms of magnitude and spatial distribution, and the implications of these changes for dose painting target definition. This work has been published in the International Journal of Radiation Oncology • Biology • Physics (*139*).

2.1. Motivation

The relationship between tumor hypoxia and radioresistance has long been established (*142*). Consequently, PET hypoxia tracers make for an appealing dose painting target. There is concern, however, over the spatio-temporal stability of hypoxia maps, particularly in the context of dose painting (*22, 42*). Tumor hypoxia levels have been shown to fluctuate over time (*125*). If hypoxic locations change between pre-treatment measurements and the onset of therapy—or if hypoxic locations change during therapy—the quality of dose painting plans could greatly deteriorate: sensitive regions could be overdosed while resistant regions underdosed. To ensure that hypoxic regions are indeed preferentially targeted, hypoxia imaging would need to be repeated frequently and dose painting plans adjusted accordingly, which may not be technically or economically feasible. The spatial stability of hypoxia distributions has previously been investigated using repeated FMISO PET scans, but with conflicting results: Nehmeh *et al*., Lin *et al*., and Roels *et al*. found poor spatial stability in serial FMISO images (*64, 143-144*), while Okamoto *et al*. found very high spatial stability (*145*). Therefore, the stability of hypoxic targets prior to and during radiotherapy remains uncertain.

FLT PET imaging for proliferation may also assist in the identification of resistant or sensitive tumor subvolumes. Accelerated repopulation of tumor cells after the onset of radiation therapy has been shown to be detrimental to patient outcome, indicating a possible relationship between during-treatment proliferation and resistance to radiation therapy (*117*). Also, drastic changes in FLT PET uptake have been observed after the onset of radiotherapy (*118-119*), with one study demonstrating that early FLT response was associated with better patient outcome (*120*). For this reason, maps of FLT PET voxel responses might provide useful information for biological target definition, and it is therefore important to characterize how proliferation maps change in tumors during radiotherapy.

The goal of this study was twofold: to assess the spatial and absolute stability of Cu-ATSM PET during radiotherapy as a surrogate for tumor hypoxia stability, and to measure changes in FLT PET during radiotherapy as a surrogate for changes in cellular proliferation.

2.2. Methods and materials

The study included 22 canine patients from the CIRT trial. Histopathology revealed 13 adenocarcinoma, 7 chondrosarcoma, 1 squamous cell carcinoma, and 1 osteosarcoma tumor. Details of the imaging and treatment protocol are found in section 1.5. For this study, only pre- and mid-treatment Cu-ATSM and FLT scans were used from each patient.

2.2.1. Tracer production

^{61}Cu ($t_{1/2}$=204.5 min) was produced via the ^{60}Ni(d,n)^{61}Cu reaction at the University of Wisconsin Cyclotron. [^{61}Cu]Cu-ATSM tracer was synthesized via the process outlined by Avila-Rodriguez (*146*). Analytic high performance liquid chromatography of [^{61}Cu]Cu-ATSM showed radiochemical purity >95% and specific activity typically between 1-3 Ci/μmol. [^{18}F]FLT tracer was also provided by the University of Wisconsin Cyclotron.

2.2.2. Data analysis

We assessed the spatial stability of Cu-ATSM and FLT SUV distributions from pre- to -mid-treatment. For each patient, pre- and mid-treatment CT images were deformably registered using the optical flow algorithm (*147*), and the resulting transformations were applied to their respective PET data. This allowed for voxel-based comparisons of pre- and mid-treatment tracer distributions. To quantify tracer spatial stability, voxel-based Spearman rank correlation coefficients (ρ) were calculated for Cu-ATSM ($\rho_{Cu\text{-}ATSM}$) and FLT (ρ_{FLT}) within each patient's GTV, comparing pre- and mid-treatment voxel SUV distributions. Spearman correlation coefficients were preferred over Pearson correlation coefficients because SUV distributions were often not normally distributed. Population-averaged ρ were calculated using the Fisher transformation, and two-sided paired *t*-tests compared patients' $\rho_{Cu\text{-}ATSM}$ and ρ_{FLT}. We also investigated whether or not $\rho_{Cu\text{-}ATSM}$ and ρ_{FLT} were influenced by tumor volume, or by the level of uptake heterogeneity within the tumor, which we quantified using the standard deviation of the SUV distribution within the GTV (SUV_{SD}).

In addition to assessing voxel correlations, we quantified the degree of spatial overlap between the high-uptake regions at pre- and mid-treatment. For each tumor, various thresholds were used to segment high-uptake regions. Thresholding was not performed as a percentage of the SUV_{max} as is typically done in PET segmentation—this type of thresholding can result in extremely small volumes for some tumor distributions. Instead, we performed volume-based thresholding of the sorted SUV distribution, from 10% to 90%, in 10% increments. For instance, a 70% threshold would include 30% of the GTV's highest uptake voxels. For each threshold level, both pre- and mid-treatment high-uptake volumes were segmented, and Dice coefficients quantified the degree of spatial overlap. The Dice coefficient is defined as the ratio of the intersection of two regions to the average volume of the two regions. After calculating each patient's Dice coefficients for both tracers and all threshold levels, two-sided paired *t*-tests determined if, across the population, Dice coefficients for Cu-ATSM were significantly different than Dice coefficients for FLT.

We investigated whether or not the magnitudes of Cu-ATSM and FLT uptake were significantly lower at mid-treatment than at pre-treatment. SUV_{max}, SUV_{peak}, and SUV_{mean} were calculated for pre- and mid-treatment PET scans (mid-treatment SUV measurements were assessed prior to deformable registration). Two-sided paired *t*-tests determined if changes in the SUV measures from pre- to mid-treatment were statistically significant across the population, with a significance level of $p \leq 0.05$.

2.3. Results

A patient's pre- and mid-treatment PET/CT images are shown in Figure 2.1. Voxel scatter plots comparing pre- and mid-treatment Cu-ATSM and FLT PET distributions are shown for four patients in

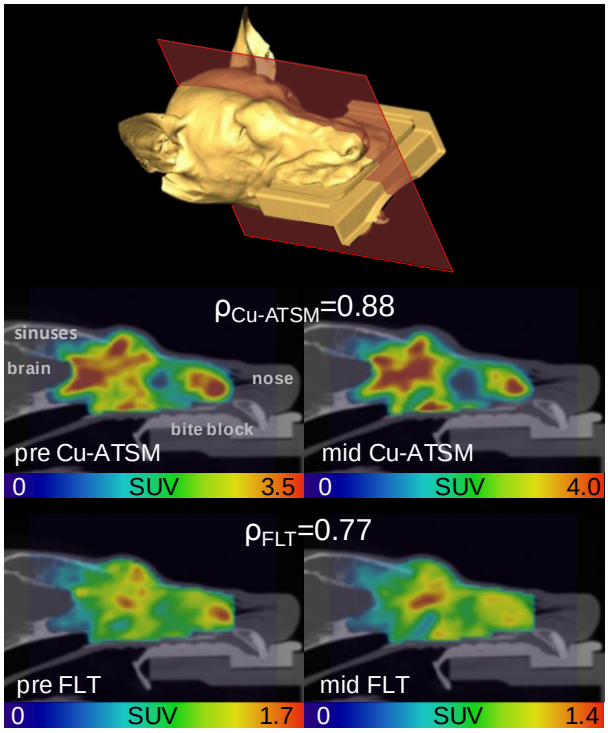

Figure 2.1. Example sagittal PET/CT slices are shown from a carcinoma patient's pre- and mid-treatment Cu-ATSM (middle) and FLT (bottom) scans. An isosurface is shown for anatomical reference. This patient is the same patient as Patient 1 in Figure 2.2, and had $\rho_{Cu\text{-}ATSM}$ and ρ_{FLT} values similar to the population averages.

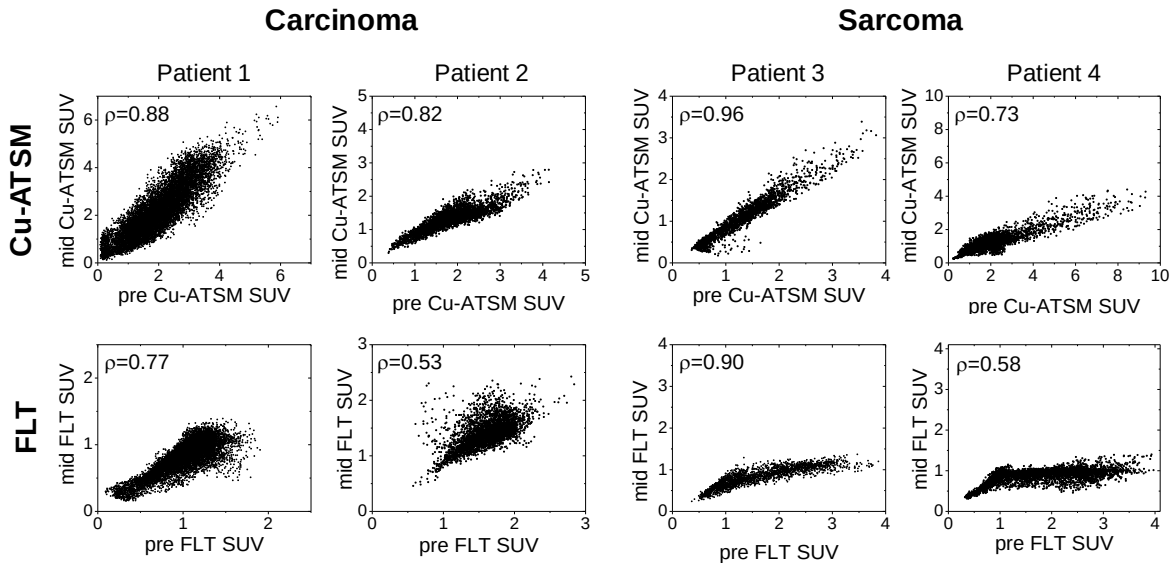

Figure 2.2. Voxel-based scatter plots comparing pre- and mid-treatment Cu-ATSM SUV distributions (top row) and FLT SUV distributions (bottom row) for four different patients — two carcinomas and two sarcomas. Spearman rank correlation coefficients are shown in upper-left corners.

Figure 2.2. The population-averaged $\rho_{\text{Cu-ATSM}}$ (±SD) was 0.88±0.07 for all patients, 0.88±0.08 for carcinoma patients, and 0.88±0.07 for sarcoma patients. The population-averaged ρ_{FLT} was 0.79±0.13 for all patients, 0.76±0.14 for carcinoma patients, and 0.84±0.12 for sarcoma patients. All patients' $\rho_{\text{Cu-ATSM}}$ and ρ_{FLT} are shown in Figure 2.3. Carcinoma and sarcoma populations were not significantly different in terms of $\rho_{\text{Cu-ATSM}}$ or ρ_{FLT} values. Using paired *t*-test we found that patients' $\rho_{\text{Cu-ATSM}}$ were consistently higher than their respective ρ_{FLT} values (P=0.001). We did not find significant correlations between tumor

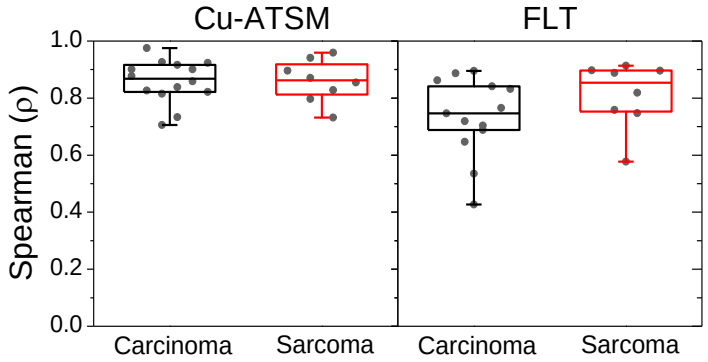

Figure 2.3. Quartile box plots of all patients' $\rho_{\text{Cu-ATSM}}$ (left) and ρ_{FLT} (right), representing the degree of tracer spatial stability through mid-treatment, separated by histologic tumor type.

volume and $\rho_{Cu\text{-}ATSM}$ or ρ_{FLT} ($R \approx 0.2$), or between SUV_{SD} and $\rho_{Cu\text{-}ATSM}$ or ρ_{FLT} ($|R| < 0.2$), indicating that tracer stability was not likely impacted by tumor volume or tumor heterogeneity.

Figure 2.4 shows the population-averaged Cu-ATSM and FLT Dice coefficients—quantifying the degree of overlap between pre- and mid-treatment high-uptake regions—plotted as a function of segmentation method. For example, using a 70% threshold (ie, the hottest 30% of the tumor volume), 77% of the pre-treatment Cu-ATSM-avid regions, on average, overlapped with the mid-treatment Cu-ATSM-avid regions. For FLT and a 70% threshold, the average overlap was 69%. Paired *t*-tests found that for a threshold of 30% and for all thresholds greater than 50%, patients' Cu-ATSM Dice coefficients were consistently greater than their respective FLT Dice coefficients ($P < 0.01$).

Resulting pre- and mid-treatment SUV_{mean} and SUV_{max} measurements are presented in Figure 2.5. On average, Cu-ATSM SUV_{mean} decreased by 18% at mid-treatment, or 1.2%/Gy when normalized by the prescribed dose. FLT SUV_{mean} decreased by 24% (2.5%/Gy) at mid-treatment. The average decreases in

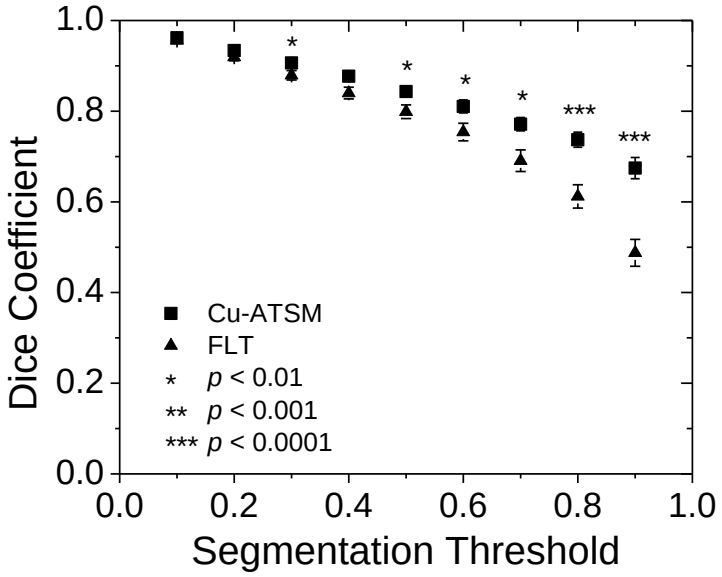

Figure 2.4. Population-averaged Dice coefficients quantifying the overlap between high-uptake regions at pre- and mid-treatment plotted as a function of segmentation method. Also shown are standard errors and results from paired *t*-tests comparing patients' respective Cu-ATSM and FLT Dice coefficients.

SUV_{max} were 9% (0.6%/Gy) for Cu-ATSM and 36% (3.8%/Gy) for FLT. Table 2.1 shows results from paired *t*-tests comparing pre- and mid-treatment SUV measures. On average, patients had significantly lower FLT uptake after two fractions of hypofractionated IMRT regardless of histology. A significant reduction in Cu-ATSM uptake was observed for carcinoma patients, while sarcoma patients showed no significant changes in Cu-ATSM uptake. Dose level (42 Gy vs. 50 Gy) had no significant effect on changes in Cu-ATSM and FLT SUV measures.

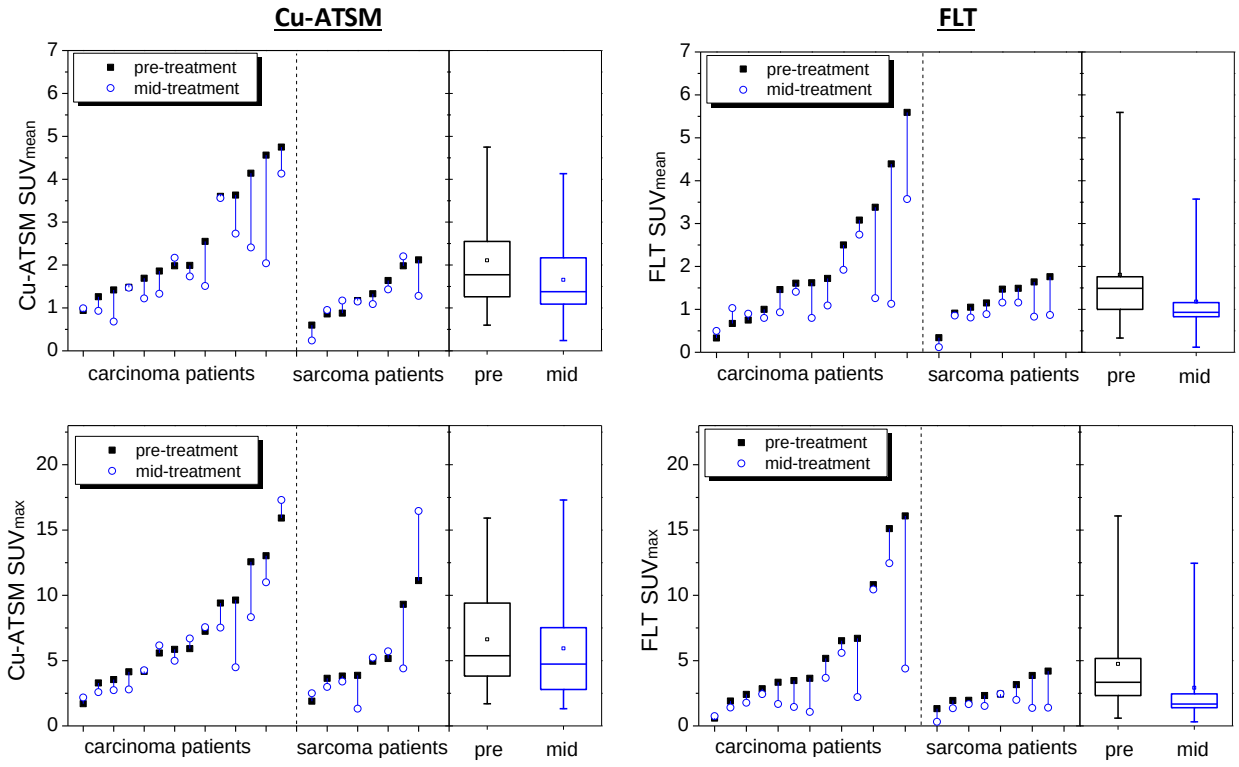

Figure 2.5. Parallel line plots comparing each patient's pre-treatment (*solid square*) and mid-treatment (*empty circle*) SUV measures for Cu-ATSM SUV_{mean} and SUV_{max} (*left*) and FLT SUV_{mean} and SUV_{max} (*right*), separated by histology. Also included are quartile box plots representing population distributions of respective SUV measures.

Table 2.1. Results from paired *t*-tests comparing patients' pre- and mid-treatment SUV measures. Significant values ($P \leq 0.05$; bolded) indicate significant decreases in SUV measures at mid-treatment.

Tracer	SUV measure	Carcinoma (N=14)	Sarcoma (N=8)	All patients (N=22)
pre vs. mid Cu-ATSM	SUV_{mean}	*P*=**0.006**	*P*=0.34	*P*=**0.004**
	SUV_{max}	*P*=0.08	*P*=0.83	*P*=0.17
	SUV_{peak}	*P*=**0.02**	*P*=0.81	*P*=**0.05**
pre vs. mid FLT	SUV_{mean}	*P*=**0.02**	*P*=**0.008**	*P*=**0.003**
	SUV_{max}	*P*=**0.02**	*P*=**0.01**	*P*=**0.004**
	SUV_{peak}	*P*=**0.04**	*P*=**0.02**	*P*=**0.01**

2.4. Discussion

2.4.1. Spatial stability of tracer distributions

We assessed the spatial stability of Cu-ATSM and FLT distributions during treatment in canine sinonasal tumors. These patients were ideal for this study for several reasons: anesthesia during imaging eliminated motion— motion blurring can cause two images to appear more similar than they really are (*148*); the bone surrounding the nasal cavity guided accurate image registration—registration inaccuracies can significantly degrade voxel-based correlations (*149*); and precise immobilization techniques enabled repeatable positioning.

Overall, spatial distributions of Cu-ATSM uptake were very stable from pre- to mid-treatment. Only three patients had $\rho_{Cu\text{-}ATSM}$ values less than 0.8. Even the highest uptake regions of the tumors (thresholds of 90%) had high average overlap (67%) between pre- and mid-treatment. Therefore, in canine sinonasal tumors, Cu-ATSM dose-painting targets are spatially stable early during radiotherapy, so that neither multiple PET scans prior to therapy, nor treatment adaptation based on additional PET imaging early in therapy, are necessary. Our results are consistent with results from Okamoto *et al.*, who

found average voxel correlations from FMISO test-retest scans to be 0.89 in HN cancer patients (*145*). In contrast, Nehmeh *et al.* found average voxel-based correlations from FMISO test-retest scans in HN cancer patients to be 0.6 over the whole tumor volume, and 0.3 when only the most hypoxic subvolumes were considered (*144*).

On average, pre- and mid-treatment FLT distributions were strongly correlated. This indicates that, for most patients, the most proliferative regions of the tumor generally remained the most proliferative regions early in therapy. This was surprising considering that FLT uptake at mid-treatment was often low (the average mid-treatment SUV_{mean} was only 1.2), and one would expect correlations to deteriorate as tumor uptake approached background levels. Considerable inter-patient heterogeneity in ρ_{FLT}, however, was observed, with three patients' ρ_{FLT} values lower than 0.6. In addition, patients' ρ_{FLT} were significantly lower than their respective $\rho_{Cu\text{-}ATSM}$, and FLT Dice coefficients were significantly lower than Cu-ATSM Dice coefficients for the high-uptake thresholds. Even the highest measured ρ_{FLT} (0.91) was only slightly better than the average $\rho_{Cu\text{-}ATSM}$ (0.88). And the highest FLT uptake regions (threshold of 90%) only had moderate overlap (49%) from pre- to mid-treatment. This indicates that proliferative response to radiation is not spatially uniform throughout the tumor, and that magnitude of intratumor heterogeneity in proliferative response appears to vary considerably across patients. Further investigations is warranted on whether intratumor proliferative response heterogeneity could provide useful information for defining dose painting targets, some of which are described in Chapters 4 and 5.

2.4.2. Changes in tracer uptake magnitude

The reason for histology-dependent changes in Cu-ATSM SUV measures is uncertain. Other animal models have also demonstrated cell-line dependence in reoxygenation patterns (*150*). The reduction in Cu-ATSM uptake, however, may also be a consequence of cell kill. SUV values are affected not only by the biological property of interest (eg, hypoxia), but by the number of tumor cells available to take up the tracer (ie, cellular density). Consequently, decreases in SUV during therapy cannot be fully attributed to either biological changes or anatomical changes alone, but rather some combination of the

two. Based on our analysis of megavoltage CTs acquired during therapy (data not shown), carcinoma tumors had a greater tendency to shrink during therapy than sarcomas. This suggests that cell kill may have been a larger factor in carcinomas than in sarcomas, perhaps influencing the histology-specific changes in Cu-ATSM SUV.

We observed significant drops in FLT SUV measures for both histologies during treatment. Other studies have found similar results (*118-119*). This reduction in proliferation could be interpreted as radiation-induced DNA damage checkpoint control (*151*), but may also represent a drop in cell density. It is interesting to note that FLT uptake decreased significantly in both carcinoma and sarcoma tumors, while Cu-ATSM uptake decreased only in carcinoma tumors. If the lower tracer uptake were primarily due to cell kill, one would have expected that, regardless of histology, both FLT *and* Cu-ATSM uptake would have simultaneously decreased. In addition, we would have expected that tumors with large changes in Cu-ATSM uptake would also experience similarly large changes in FLT uptake (ie., Cu-ATSM response would correlate with FLT response across patients). However, this was not observed: changes in FLT SUV were not correlated with changes in Cu-ATSM SUV ($R \approx 0.2$, data not shown). This suggests that changes in FLT uptake were driven primarily by functional response rather than anatomical response.

2.4.3. Limitations

There are uncertainties in the interpretations of this study's results, particularly in application to human cancers. While humans and dogs have many biological similarities—they are more similar in growth rate, vasculature, treatment response, and gene expression profile that humans and mouse models (*152*)—the use of anesthesia and 100% O_2 during imaging may affect tracer uptake (*153-154*) (although patients were awake and breathing air during the 3-hour Cu-ATSM uptake period). Cu-ATSM also has less binding affinity for serum albumin in dogs than in humans, potentially influencing uptake (*155*). There is also uncertainty regarding Cu-ATSM's specificity for hypoxia. The understanding of Cu-ATSM's uptake mechanism has evolved over time (*156*), but has recently been shown to be caused by impaired

mitochondrial electron transport chain function—a consequence of cellular hypoxia (*157*). Nonetheless, studies have found certain tumor types to have poor spatial correlations of Cu-ATSM and FMISO uptake patterns, especially with shorter Cu-ATSM uptake periods (*158*). We used a 3-hour uptake period for Cu-ATSM based on preliminary analysis we performed in canine patients: we found that Cu-ATSM uptake at 24 hours post-injection had higher spatial correlations to Cu-ATSM uptake at 3-hours post-injection than at 1-hour post-injection ($R \approx 0.85$; data not shown). Finally, we emphasize that while tracer distributions were spatially stable early during treatment, tracer distributions at later mid-treatment time points are likely to be less stable.

2.5. Conclusion

In this chapter, we aimed to evaluate the spatio-temporal stability of Cu-ATSM and FLT PET distributions in canine sinonasal tumors during fractionated radiation therapy. We found that spatial distributions of Cu-ATSM and FLT PET remained mostly stable after a few fractions of IMRT, despite significant decreases in mid-treatment SUV measures. FLT PET spatial distributions were mostly stable, but they were significantly less stable than Cu-ATSM PET spatial distributions. As targets for dose painting, Cu-ATSM and FLT PET appear to be spatially robust targets in canine sinonasal tumors, and would be unlikely to require repeated imaging and replanning early during fractionated radiation therapy. This is the first study to report on the spatial stability of Cu-ATSM and FLT PET uptake distributions during therapy.

3. Patterns of FDG, FLT, and Cu-ATSM PET uptake in sarcoma and carcinoma tumors in canines

This chapter also addresses Specific Aim 1 of the dissertation, which is to evaluate properties of FDG, FLT, and Cu-ATSM PET as they relate to target definition in dose painting. Specifically, this chapter describes the similarities and dissimilarities in FDG, FLT, and Cu-ATSM PET uptake distributions in sarcoma and carcinoma canine tumors, and describes how dose painting plans are likely to differ according to different biological targets. This work has been published in the Journal of Nuclear Medicine (*141*).

3.1. Motivation

Biological heterogeneity within tumors, or intratumor heterogeneity, occurs when a single tumor has regional variations in biological—and even genetic—properties (*159*). Intratumor heterogeneity presents a challenge for advanced or targeted therapies where specific biological processes are targeted: certain tumor regions might express the biological target while other tumor regions might not. With increasing interest in therapies that target specific biological mechanisms, measuring intratumor heterogeneity may, in the future, help inform treatment selection, and could influence staging and treatment response assessment.

In biologically conformal radiotherapy, it is uncertain which biological property should be targeted for dose escalation. Tumors in which different biological targets (eg, cellular hypoxia and glucose metabolism) have similar spatial distributions would be robust targets for dose painting: targeting one phenotype would result in a similar treatment plan as targeting other phenotypes. However in tumors where different biological targets cluster in different regions of the tumor, dose painting treatment plans would be sensitive to the choice of biological target. Measuring spatial distributions of different

biological targets could help identify tumor types that are most likely to gain from dose painting treatments.

The purpose of this study was to measure and compare spatial distributions of three different biological properties in tumors—glucose metabolism, cellular proliferation, and hypoxia—in two different tumor histologies. Surrogates of these properties were measured using PET radiotracers FDG, FLT, and Cu-ATSM, respectively. We compared sarcoma and carcinoma canine tumors in terms of FDG, FLT, and Cu-ATSM PET uptake patterns, including a comparison of uptake magnitudes and an analysis of spatial relationships between the three tracer distributions.

3.2. Materials and methods

Twenty canine patients of from the CIRT trial were included in the study. This included 12 adenocarcinoma patients, 6 chondrosarcoma patients, 1 squamous cell carcinoma patient, and 1 osteosarcoma patient. The imaging and treatment schedule, and details of image acquisition and processing, are found in section 1.5. This study used patients' pre-treatment FDG, FLT, and Cu-ATSM PET/CT images.

3.2.1. Data Analysis

The magnitudes of FDG, FLT, and Cu-ATSM uptake were compared between sarcoma (N=7) and carcinoma (N=13) tumors. SUV_{max}, SUV_{peak}, and SUV_{mean} were calculated for each patient, and then compared between sarcoma and carcinoma patient populations. Two-sided Mann-Whitney *U*-tests were used to determine significant differences. In addition, *F*-tests were used to compare variances of SUV measures between sarcomas and carcinomas.

For this study, patients' images were registered using rigid registration: all CT images were cropped to include only the volume of interest, and then rigidly registered to a single reference CT image in Amira® (Visage Imaging Inc., San Diego) using mutual information. The resulting transformations were then applied to their respective PET data. This allowed for a voxel-based comparison of FDG, FLT,

and Cu-ATSM uptake distributions in each tumor. Voxel-based Spearman rank correlation coefficients were calculated for each tracer combination: FLT:Cu-ATSM, FDG:Cu-ATSM, and FDG:FLT. Spearman rank correlation coefficients were used instead of Pearson correlation coefficients to avoid assumptions of linearity and normality. Correlation coefficients were averaged for sarcomas and carcinomas using the Fisher transformation, and two-sided *t*-tests determined significant differences between the two tumor histology *z*-score distributions.

In addition to a voxel-based analysis, tracer uptake patterns in sarcoma and carcinoma tumors were compared by analyzing the degree of overlap between tracer-avid uptake regions. Tracer-avid volumes were created for each tracer by applying a threshold of each tracer's SUV_{max} within the GTV, resulting in three tracer-avid volumes per tumor. From these three volumes we calculated the percent overlap relative to the total thresholded volume (ie, the intersect relative to the union). As the best threshold for segmenting tumor volumes is unknown, we applied several different thresholds, from 10% to 90% of SUV_{max} in 10% increments. At each threshold level, the percent overlap was quantified. These overlap percentages were then averaged for both tumor histologies, and *t*-tests determined if the degrees of overlap were significantly different between histologies. To better visualize the histology-averaged tracer overlap, we created Venn diagrams (*160*) for each threshold level.

3.3. Results

3.3.1. Magnitude of Tracer Uptake

Table 3.1 shows SUV measures when averaged over the sarcoma and carcinoma populations, with *P*-values resulting from Mann-Whitney *U*-tests. Carcinomas had significantly higher FDG SUV_{max} than sarcoma tumors (11.1 vs 5.0; P=0.01), as well as higher Cu-ATSM SUV_{mean} (2.6 vs 1.2; P=0.02). Differences in FDG SUV_{mean} and SUV_{peak} were approaching significance (P=0.057). For all SUV

Table 3.1. Histology-averaged SUV measures

Tracer	SUV_{mean}			SUV_{max}			SUV_{peak}		
	Sarc	Carc	*P*	Sarc	Carc	*P*	Sarc	Carc	*P*
FDG	2.3	4.5	0.057	5.0	11.1	**0.014**	3.9	8.3	0.057
FLT	1.3	2.7	0.38	2.8	7.6	0.13	1.9	5.3	0.27
Cu-ATSM	1.2	2.6	**0.022**	4.6	7.4	0.15	3.3	5.5	0.13

Sarc = sarcoma; Carc = carcinoma

measures, carcinomas had higher average uptake than sarcomas. Box plots of patients' SUV_{mean} and SUV_{max} measurements are shown in Figure 3.1. It is evident from Figure 3.1 that the interpatient range, or variance, in SUV measures was much larger for carcinomas than sarcomas. This was confirmed by *F*-tests, which found the variances to be significantly different between histologies ($P<0.01$) in all cases but Cu-ATSM SUV_{max} and SUV_{mean}. The average tumor volumes were not significantly different between histologies.

3.3.2. Spatial Correlations

Figure 3.2 shows voxel-based SUV scatter plots for three carcinoma patients on the left, and three sarcoma patients on the right. Four of the seven sarcoma tumors had FLT:Cu-ATSM scatter plots that appeared to be bifurcated, with one arm of low hypoxia and varying degrees of proliferation, and another arm with low proliferation and varying degrees of hypoxia. The other three sarcoma tumors had fan-shaped scatter plots. Carcinoma tumors, on the other hand, generally had high linear correlations between phenotypes. Box plots of patients' voxel-based Spearman correlation coefficients, separated by tumor histology, are shown in Figure 3.3. Fisher-averaged correlation coefficients and *t*-test results are shown in Table 3.2. Carcinomas had significantly higher intertracer correlations than sarcomas for all tracer comparisons. The greatest differences between the two histologies were the FLT:Cu-ATSM correlations, where the average correlation coefficient was 0.38 for sarcomas, and 0.83 for carcinomas ($P < 10^{-4}$).

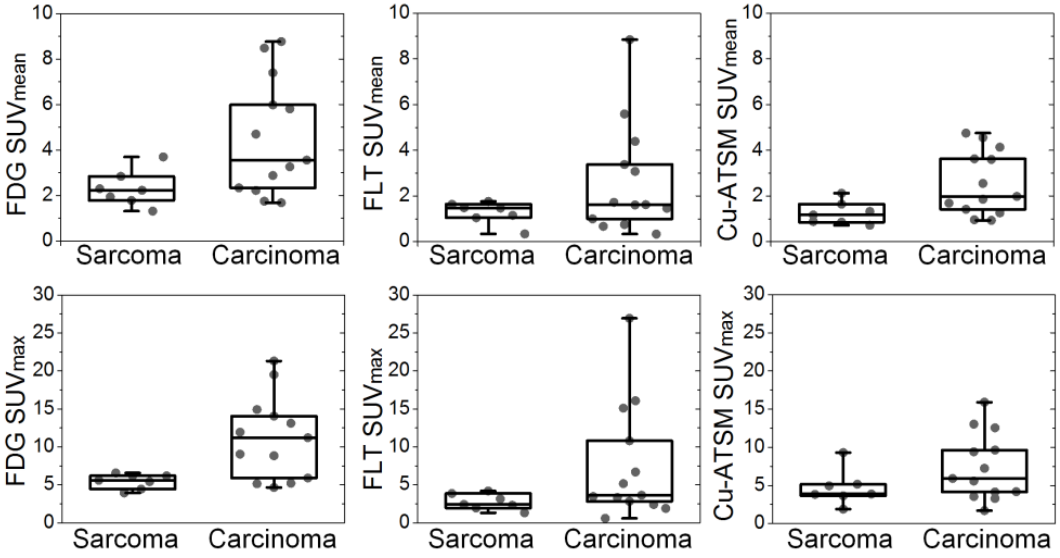

Figure 3.1. Quartile box plots representing distributions of SUV_{mean} (*top row*) and SUV_{max} (*bottom row*) for FDG (*left column*), FLT (*middle column*), and Cu-ATSM (*right column*) PET scans, separated by tumor histology.

.Table 3.2. Histology-averaged Spearman correlation coefficients.

Tracers	Sarcoma Avg ρ	Carcinoma Avg ρ	*P*
FLT:Cu-ATSM	0.38	0.83	<0.0001
FDG:Cu-ATSM	0.69	0.82	0.04
FDG:FLT	0.61	0.80	0.02

3.3.3. Overlapping Volumes

Examples of tracer-avid volumes using a 70% threshold are shown for 12 tumors in Figure 3.4. Tracer-avid regions generally overlapped in carcinoma patients, but were spatially separated in sarcoma patients. Figure 3.5 shows Venn diagram representations of intertracer overlap, averaged for carcinomas and sarcomas, using nine different SUV thresholds. Low thresholds (≤ 30%) and high thresholds (90%) showed no significant differences between histologies. For thresholds between 40-80%, however, significant differences were observed between sarcomas and carcinomas; *t*-test results are shown in Table 3.3. No significant differences were observed between sarcomas and carcinomas in terms of FDG:FLT overlap for any threshold. Overlap between Cu-ATSM:FDG and Cu-ATSM:FLT were significantly

different between the histologies for thresholds of 40-80%, with carcinomas having greater average overlap. The regions where all three tracers overlapped were also significantly larger in carcinomas for thresholds of 40-70%.

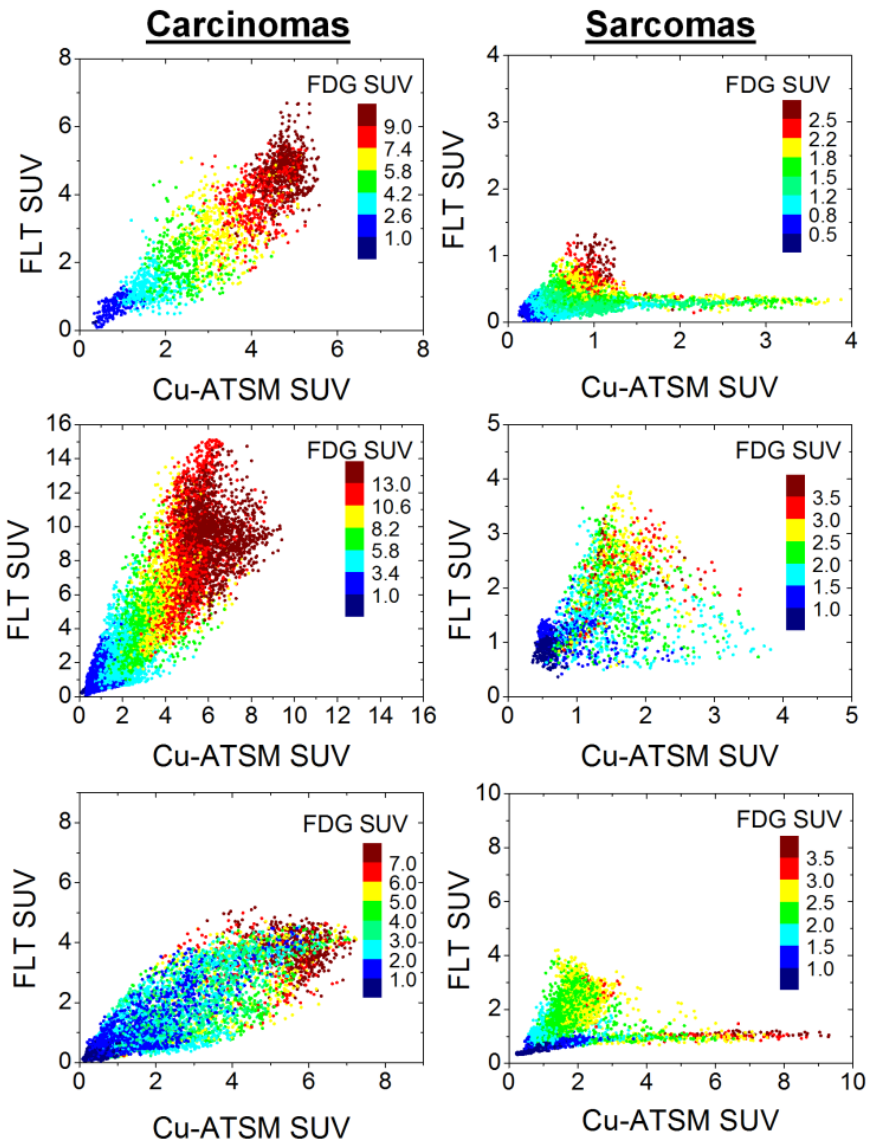

Figure 3.2. Voxel-based SUV scatter plots for three carcinoma patients on the left, and three sarcoma patients on the right, illustrating intratumor tracer correlations. Each point represents a voxel inside the tumor, with its position and color representing the voxel's SUV values from the three PET scans.

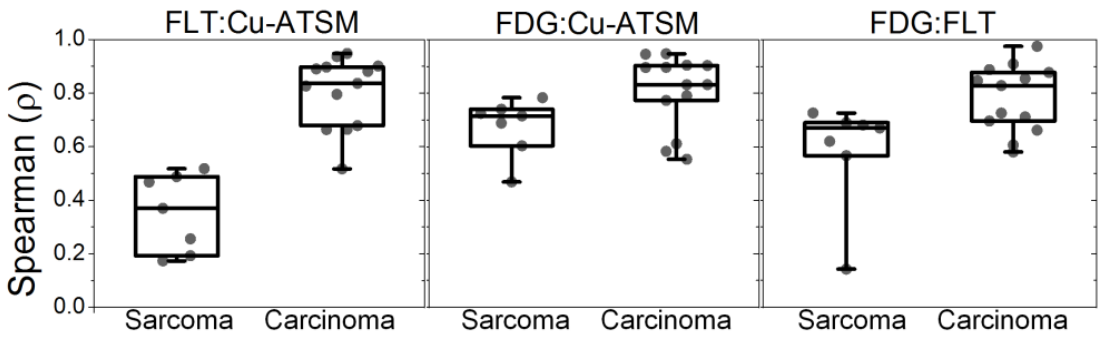

Figure 3.3. Quartile box plots representing distributions of voxel-based Speaman correlation coefficients for sarcoma and carcinoma patient populations, comparing FLT and Cu-ATSM (*left*), FDG and Cu-ATSM (*middle*), and FDG and FLT (*right*).

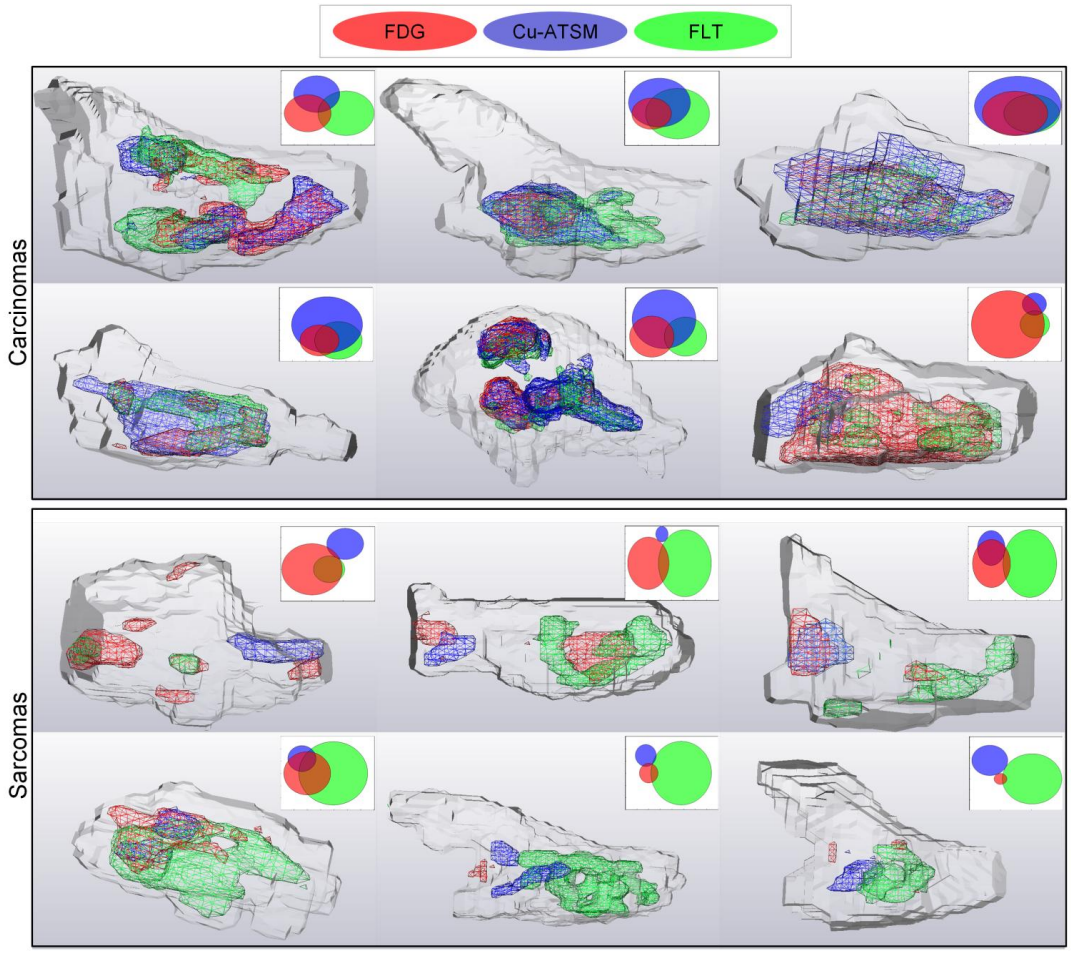

Figure 3.4. Three-dimensional representations of twelve patients' GTVs (*gray outline*) with tracer-avid volumes inside. The tracer-avid volumes presented in these images were created by applying a 70% threshold to each respective tracer, with FDG in red, Cu-ATSM in blue, and FLT in green. Venn diagrams in the upper right corners help visualize the degree of overlap.

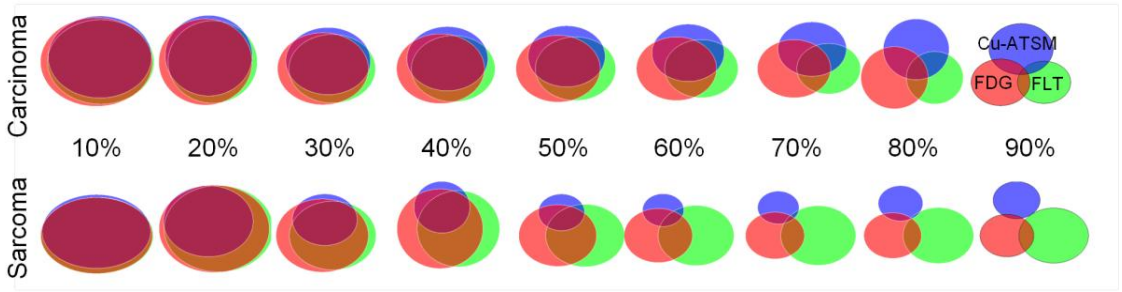

Figure 3.5. Venn diagrams representing average degrees of overlap between tracer-avid volumes for various thresholds, averaged for carcinomas (*top row*) and sarcomas (*bottom row*). FDG volumes are represented by red, Cu-ATSM by blue, and FLT by green.

Table 3.3. Comparison of overlapping tracer-avid volumes for sarcomas and carcinomas

Region of Overlap	*P*-values for thresholds of:				
	40%	50%	60%	70%	80%
FLT ∩ Cu-ATSM	0.02	<0.001	<0.001	0.004	0.04
FDG ∩ Cu-ATSM	0.05	0.004	0.002	0.006	0.03
FDG ∩ FLT	-	-	-	-	-
FLT ∩ FDG ∩ Cu-ATSM	0.04	0.002	0.001	0.002	-

Significant values indicate that carcinomas had significantly greater overlap of respective tracers than sarcomas;*P* values greater than 0.05 are not shown, indicated by (-).

3.4. Discussion

In comparing FDG, FLT, and Cu-ATSM uptake patterns in canine nasal tumors, we found that sarcoma tumors had significantly lower FDG and Cu-ATSM uptake than carcinoma tumors. Two other studies—one in canines (*161*) and one in human lung cancer patients (*162*)—compared FDG uptake in sarcoma and carcinoma tumors and found similar results. Lower FDG and Cu-ATSM uptake may be indicative of a less aggressive phenotype in sarcoma tumors. However, the low uptake may also be caused by a lower tumor cell density, which is characteristic of chondrosarcoma tumors (*163*).

Spatial correlations of FDG, FLT, and Cu-ATSM PET were heterogeneous across patients, with Spearman correlation coefficients ranging from 0.14 to 0.98. Carcinoma tumors had significantly higher correlations and colocalizations of tracers than sarcoma tumors. The greatest discordance between the two histologies was the FLT:Cu-ATSM correlations. In four of the seven sarcoma patients, there were distinctive bifurcations in the FLT:Cu-ATSM scatter plots (three of these patients also had minor bifurcations in their FDG:Cu-ATSM scatter plots), which have not been reported in literature. The two branches, when mapped back into three-dimensional image space, resulted in two spatially contiguous tumor regions. This suggests that significant phenotypic heterogeneity exists in sarcoma tumors, with distinct regions of proliferation, distinct regions of hypoxia, and varying levels of metabolism. It is also possible that one branch of the bifurcation is due to normal tissue uptake. We have observed that the ethmoturbinates located caudally in the canine nasal cavity consistently had nonspecific uptake of FDG and Cu-ATSM, with SUVs around 2-4. When we contoured out regions where the GTV overlaps with the ethmoturbinates, the scatter plot bifurcations indeed become less pronounced (data not shown). However, the correlations in sarcoma tumors remained significantly lower than in carcinoma tumors regardless of ethmoturbinate inclusion.

The biological underpinnings of the observed uptake patterns are unclear. Based on analysis of DCE-CT scans acquired in the same patient population, tracer uptake patterns did not appear to be spatially correlated to perfusion parameters (*164*). Assuming that high FDG, high FLT, and high Cu-ATSM uptake indicates the colocalization of metabolism, proliferation, and hypoxia, the high intertracer correlations in carcinomas may be explained by increased cellular hypoxia inducible factor 1 (HIF-1) activity, which can activate metabolic enzymes and transporters and drive proliferation (*165*). This reasoning may be supported by a study by Kaira *et al.*, where human lung carcinoma patients were found to have significantly higher HIF-1α expression than lung sarcoma patients (*162*). Conversely, the low intertracer correlations observed in sarcomas may be due to a preference of sarcoma cells to undergo cell cycle arrest under hypoxic conditions, thereby lowering proliferation rates (*166*). However, as a voxel's

SUV only reflects an average of the many cellular processes occurring within its macroscopic volume, we cannot explain the trends with certainty. Interestingly, while sarcoma tumors had significantly more phenotypic heterogeneity than carcinoma tumors, canine sarcoma nasal tumors are reported to respond better to treatment than carcinoma tumors (*167*). This is in contrast to other studies that have shown intratumor heterogeneity, although defined and measured differently, to be associated with worse outcome (*168*).

Treatments designed to specifically target certain tumor phenotypes (e.g. dose painting) may result in very different outcomes for carcinoma and sarcoma tumors. In carcinomas, where proliferative, hypoxic, and metabolic phenotypes were colocalized, targeting one phenotype appears likely to simultaneously target the other two phenotypes. Alternatively, in sarcomas, each tracer accumulated in different regions of the tumor, and targeting a single phenotype would likely miss tumor regions with high expression of the other two phenotypes. Consequently, dose painting in canine carcinoma tumors could be considered a safer bet than dose painting in sarcoma tumors. It may also be the case that in different tumor histologies the relationships between various biological properties and treatment resistance may be different. This was observed in a study involving a smaller subset of this patient population, where we observed histology-dependence when associating distributions of different pre-treatment tracers with follow-up FDG distributions (*95*).

This is the first study to have reported comparisons of three tracer distributions in two different tumor histologies. Results from previous studies comparing two tracers in two or more histologies were in agreement with our results—namely that spatial correlations of different biological properties are histology-specific (*169-171*). Tumor types that have demonstrated poor correlations between metabolic activity and hypoxia include, in rodents, colon adenocarcinoma (*172*) and Lewis lung carcinomas (*173*), and in humans, lung squamous cell carcinoma (*170*) and sarcomas (*171*). On the other hand, high correlations have been found in head-and-neck (*171*) and lung adenocarcinoma (*170*) patients. Hansen *et al.* compared FDG and Cu-ATSM distributions in six sarcoma and three carcinoma canine tumors and

found moderate to strong voxel correlations, but reported no comparisons between histologies (*174*). Studies that have investigated FLT and hypoxia correlations in tumors have found varying degrees of correlation in human oropharyngeal tumors (*149*), high correlations in a 9L gliosarcoma rat model (*175*), and low correlations in non-small cell lung cancer (NSCLC) xenografts in mice (*176*). For intratumor correlations of FDG and FLT, Nyflot *et al.* reported high correlations in oropharyngeal tumors (*149*), while Huang *et al.* reported low FDG:FLT overlap in NSCLC xenografts (*176*). Other studies have found FDG uptake to be strongly influenced by proliferation rate (*177*). These reports, coupled with our findings, suggest that tumors of different histologies have substantially different relationships among biological properties, although trends do appear to occur within individual histologies.

Many of the limitations of this study have been addressed in section 2.4.3. An additional limitation specific to this study is that we grouped together all sarcoma tumors (six chondrosarcomas and one osteosarcoma) and all carcinoma tumors (twelve adenocarcinomas and one squamous cell carcinoma) for analysis. They were grouped together because of their similarities in tracer uptake patterns, however we recognize that genetic profiles can vary drastically between different sarcomas and carcinoma subtypes (*178*). Therefore, phenotypic patterns may have different trends in different subtypes.

3.5. Conclusion

Distributions of Cu-ATSM, FLT, and FDG uptake were spatially disparate in sarcoma tumors, whereas in carcinoma tumors, the uptake distributions of all three PET tracers were spatially colocalized. Additionally, carcinoma tumors demonstrated much greater interpatient heterogeneity in the magnitude of tracer uptake for all three tracers. This implies that the interrelationship between hypoxia, proliferation, and metabolism may be significantly different in sarcoma and carcinoma canine tumors. Consequently, targeting a single biological property via dose painting may result in very different outcomes for different tumor histologies. Canine carcinoma tumors represent a tumor type that is likely to be robust to how the dose painting target is defined: regardless of which PET tracer is used, dose painting dose distributions for carcinomas would be similar. Canine sarcoma tumors represent a tumor type in which it is very

important to select the best dose painting target, as large differences exist between the locations of different biological targets. It is unclear if tumor types with similar properties exist in humans, but identifying those that are robust to target definition may help in selection of patients most likely to benefit from dose painting.

4. Predicting location of recurrence using PET imaging and voxel regression modeling

This chapter also addresses Specific Aim 1, which is to evaluate properties of FDG, FLT, and Cu-ATSM PET as they relate to target definition in dose painting. This chapter aimed to address one of the most important properties of a dose painting target: the *spatial* relationship between imaging patterns and resistance to radiation therapy. Voxel-based regressions were used to relate PET imaging patterns to post-treatment recurrent tumor location, in order to evaluate which PET tracer is the best spatial biomarker of resistance.

4.1. Motivation

The success of dose painting is contingent on the ability of biological imaging to reliably and consistently identify resistant tumor subvolumes before (or during) radiation therapy. Unlike traditional imaging biomarkers of resistance in which tumor imaging summary statistics (eg, maximum standardized uptake value) are correlated with clinical outcome, imaging targets for dose painting need to spatially correlate with spatial patterns of resistance. As tumor radioresistance cannot be directly measured, location of recurrence is often used as a surrogate measure of tumor resistance (*100, 179-180*). Pre- and post-treatment images are coregistered, and the locations of tumor recurrence on the post-treatment image are mapped back to the pre-treatment image. Patterns of recurrence are then compared to the pre-treatment imaging patterns. For example, using positron emission tomography (PET) imaging in non-small cell lung cancer tumors, Aerts *et al.* found high spatial overlap between post-treatment 2-deoxy-2-[^{18}F]fluoro-D-glucose (FDG) uptake and pre-treatment FDG uptake (*14, 179*). In head-and-neck tumors, Soto *et al.* found that 8 out of 9 patients' recurrence volumes resided primarily within regions of high pre-treatment FDG uptake (*109*). Results such as these have encouraged the use of FDG as a target for dose painting, and consequently clinical trials of FDG dose painting have been conducted in head-and-neck

and lung tumors (*59, 65, 79*). Other PET radiotracers, such as FLT and Cu-ATSM, may also demonstrate promise as spatial markers of radioresistance.

The goal of this work was to assess how accurately pre-treatment FDG PET imaging, as well as pre- and mid-treatment FLT and Cu-ATSM PET imaging, predicts the location of residual or recurrent tumor in canine sinonasal tumors. This work builds off of a previously-published exploratory study, in which Bowen and colleagues performed voxel regressions of pre-treatment FDG, FLT, and Cu-ATSM uptake values against 3-month post-treatment FDG uptake values in 9 canine patients (*95*). In that study, they found that pre-treatment FDG PET performed better than FLT and Cu-ATSM PET at predicting post-treatment FDG PET distributions. This work builds on these results by increasing the number of patients, adding additional predictor variables in mid-treatment FLT and Cu-ATSM PET images, and expanding the statistical methods of analysis.

4.2. Methods

Nineteen of the 22 patients from the CIRT trial were evaluable for this study. Three patients were excluded from analysis: two because no residual/recurrent tumor was visible in follow-up PET/CT images, and one because the tumor did not shrink following treatment. Details of the imaging and treatment protocol are found in section 1.5. For this study, patients' pre- and mid-treatment PET images were used, as well as post-treatment FDG PET images. All analysis was performed inside the GTV, with the ethmoturbinates manually segmented and removed from analysis due to non-specific uptake of FDG and Cu-ATSM.

4.2.1. Regression analysis

Similar to Bowen *et al.* (*95*), we used voxel regression methods to assess how well PET uptake patterns predicted the location of tumor recurrence. For each tumor, pre-treatment FDG (FDG_{pre}), FLT (FLT_{pre}), Cu-ATSM ($Cu\text{-}ATSM_{pre}$) and mid-treatment FLT (FLT_{mid}) and Cu-ATSM ($Cu\text{-}ATSM_{mid}$) voxel SUVs were regressed against follow-up FDG voxel values (FDG_{post}), which was used as a surrogate for

residual/recurrent tumor. Ratios of mid-treatment voxel values to pre-treatment voxel values for FLT (R_{FLT}) and Cu-ATSM ($R_{Cu\text{-}ATSM}$) images were also used as predictor variables. Two types of regression were considered. In linear regression models, voxel SUVs from patients' post-treatment FDG images were used as response variables. In logistic regression models, recurrent tumor was segmented in the post-treatment FDG PET image, and the response variables were converted to binary variables — 1 if the voxel was within the segmented volume, and 0 otherwise. The segmentation of post-treatment images was performed using an in-house automatic segmentation algorithm that combines gradient, region-growing, and textural feature methods (*181*). Simple regression models and a multivariable regression model were created for each patient. For multivariable models, all 5 PET images were included as predictor variables (ratio variables were not included, as the multivariable model already accounts for absolute differences between pre- and mid-treatment voxel values). As patients had multiple follow-up FDG PET scans, the time point at which the tumor was the smallest was used for the response variable.

To evaluate how well pre- and mid-treatment PET distributions predicted recurrent tumor, goodness of fits of the regression models were calculated. For linear regression models, the coefficient of determination (R^2) was calculated. For logistic regression models, pseudo R^2 was used. Pseudo R^2 was calculated according to the correlation between the model's predicted response and measured response values:

$$Pseudo\ R^2 = 1 - \frac{\sum_{i=1}^{N}(y_i - \hat{\pi}_i)^2}{\sum_{i=1}^{N}(y_i - \bar{y})^2} \quad , \qquad (4.1)$$

where y_i is the *i*th response value, $\hat{\pi}_i$ is the model-predicted probability, and $\bar{y}$ is the mean response value. It should also be noted that pseudo R^2 for logistic regression and R^2 from linear regression are not directly comparable, but do have similar interpretations. Significance testing of the regression coefficients was not performed due to the very high spatial correlations between neighboring voxels, which resulted in exaggerated significance values. Similar to Bowen *et al.*, two-tailed *t*-tests were used to assess if the population of regression coefficients from all patients were significantly different from zero (*95*).

Using correlation analysis, we investigated if any clinical measures or imaging biomarkers could predict which patients would have high or low R^2 (ie, which patients would be good or poor candidates for dose painting). Clinical measures that were tested as predictors of R^2 values included histologic tumor type and dose level. Imaging biomarkers that were tested included tumor volume, maximum and mean SUV from pre- and mid-treatment images, relative changes in maximum and mean SUV from pre- to mid-treatment, and relative change in 1D tumor size.

4.2.2. Predictive modeling

Given the limitations of linear regression (eg, linearity), we also created advanced prediction models to evaluate how accurately the location of recurrence for a "new" patient could be predicted given the imaging data of all the other patients. For each patient, 4 prediction models were created/trained based on the other 17 patients' combined data, and then applied to the test patient (ie, leave-one-out cross validation). One patient was excluded due to missing FLT_{mid} data. Each model was trained on patients' pre- and mid-treatment PET images, with FDG_{post} as the response/predicted variable.

The 4 models included a multivariable linear regression (LR) model (as a basis for comparison), a classification and regression tree (CART) model (*182-183*), a linear mixed-effects regression (LMER) model, and a multivariable linear regression model that included neighborhood structures surrounding each voxel as additional covariates to account for autocorrelation between neighboring voxels. The autocorrelation model was defined as follows:

$$FDG_i^{post} = \beta_0 + \beta_1 PET_{1i} + \beta_2 \sum_{j \epsilon \mathcal{N}_i} PET_{1j} + \cdots + \beta_9 PET_{5i} + \beta_{10} \sum_{j \epsilon \mathcal{N}_i} PET_{5j} \quad , \qquad (4.2)$$

where FDG_i^{post} is the post-treatment FDG SUV at voxel *i*, PET_{mi} is the SUV at voxel *i* for the *m*th PET image, β_k are the 10 regression coefficients (2 for each PET image), N_i is the neighborhood surrounding voxel *i*, and PET_{mj} is the SUV of the *j*th voxel in N_i for PET image *m*. For this study, we used the first-

order neighborhood surrounding voxel *i* to define N_i, meaning only those voxels sharing a side with voxel *i*.

For each patient, predicted FDG_{post} values were compared to true FDG_{post} values, and prediction accuracy was quantified using R^2. When pooling the 17 patients' data for training the models, only 249 voxels were randomly sampled and used from each patient so that each tumor was equally represented in the pooled model, regardless of tumor size (249 voxels was the size of the smallest tumor). Fitted R^2 (or pseudo R^2) values were calculated based on the model fit of the 17 patients × 249 voxels = 4,233 voxels. For testing prediction accuracy, R^2 was calculated by applying the fitted model to all the voxels of the tested patient. The procedure was repeated 100 times for each patient, and the average of the resulting R^2 values were reported. These steps were then repeated using binary response variables (ie, segmented post-treatment FDG images) instead of continuous response variables. The same 4 models were trained for each patient, except logistic regression was used instead of linear regression, and prediction accuracy was quantified according to pseudo R^2.

4.3. Results

An example patient's PET/CT images and simple linear regression plots are shown in Figure 4.1. In Figure 4.2, example images from 3 adenocarcinoma patients' pre-treatment PET/CT imaging, during treatment CT and mega-voltage CT (MVCT) imaging, and post-treatment FDG PET/CT imaging are shown. These 3 patients demonstrated various ways by which tumors shrank during and after treatment. All 3 tumors appeared anatomically similar at pre-treatment, nearly filling one side of the nasal cavity. However, Patient 1's tumor began to shrink by the end of therapy, resulting in multiple fragmented patches of residual tumor. Patient 2's tumor demonstrated slower, more elastic shrinking, resulting in a single, nearly-spherical mass of residual tumor. Patient 3's tumor represented a mix between elastic tumor shrinkage and patchy tumor shrinkage, and began responding anatomically immediately after the onset of therapy.

4.3.1. Regression results

Results from simple linear and logistic regressions for all patients are shown in Figure 4.3. Overall, linear regression coefficients were significantly different from zero across the population for all pre- and mid-treatment tracers (P<0.05) according to t-tests. R_{FLT} coefficients were significantly less than zero (P=0.038), whereas $R_{Cu\text{-}ATSM}$ coefficients were not significantly different from zero (P=0.055). Likewise, for logistic regression, regression coefficients for all pre- and mid-treatment tracers were significantly different from zero (P<0.05), except for FLT_{pre} (P=0.38). Again, R_{FLT} coefficients were significantly less than zero (P=0.028), whereas $R_{Cu\text{-}ATSM}$ coefficients were not (P=0.33).

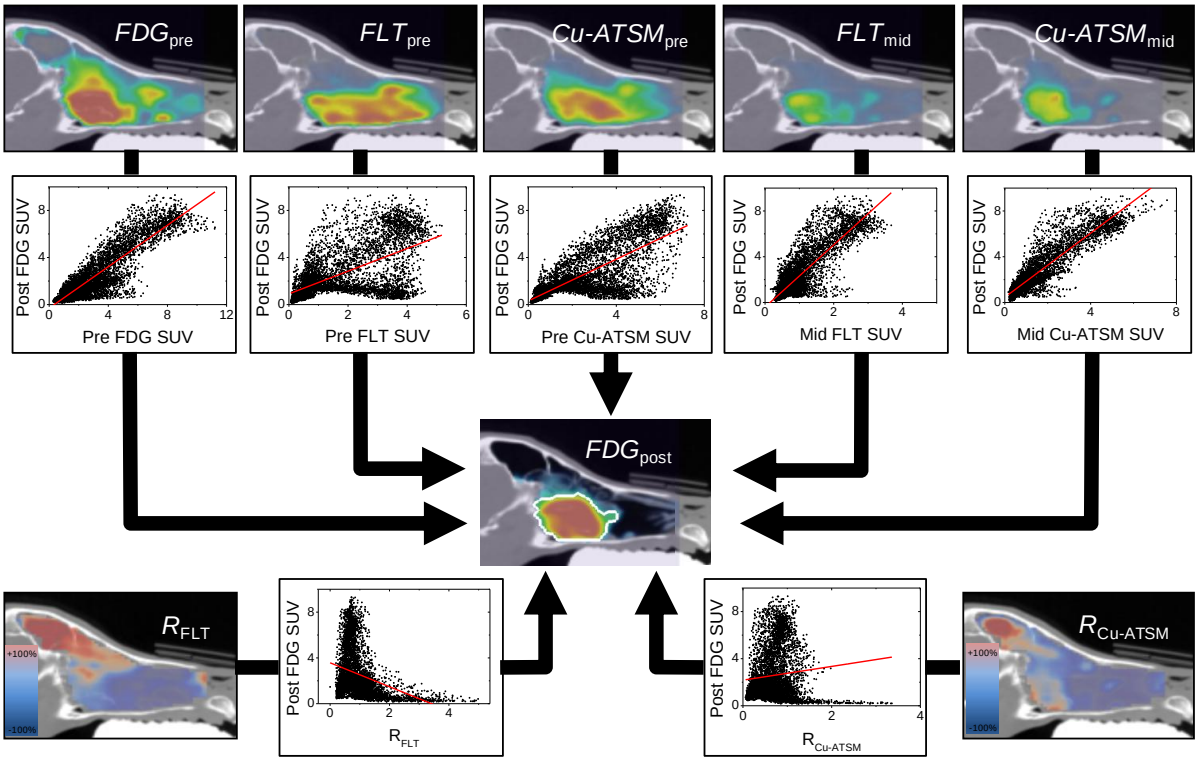

Figure 4.1. An example patient is shown, illustrating the simple linear voxel regression method. Pre- and mid-treatment PET voxel values (*top row*) were regressed against follow-up FDG voxel values. Response maps (R_{FLT} and $R_{Cu\text{-}ATSM}$; *bottom row*) were also regressed against follow-up FDG. For logistic regression, post-treatment voxel values were dichotomized using a in-house segmentation method (*outlined in white*).

Figure 4.3 shows R^2 and pseudo R^2 for all patients' linear and logistic simple models. There was large variability between patients in goodness of fits, with R^2 and pseudo R^2 values ranging from 0.00 to 0.85, with an overall median of 0.12. For linear regression, the median R^2 for FDG_{pre} was 0.19, while the median R^2 values for FLT_{pre}, $Cu\text{-}ATSM_{pre}$, FLT_{mid}, and $Cu\text{-}ATSM_{mid}$ were all around 0.10. Median R^2 for

R_{FLT} and $R_{Cu\text{-}ATSM}$ were less than 0.05. For logistic regression, median pseudo R^2 values for FDG_{pre}, FLT_{pre}, $Cu\text{-}ATSM_{pre}$, FLT_{mid}, and $Cu\text{-}ATSM_{mid}$ varied between 0.06 to 0.10, and R_{FLT} and $R_{Cu\text{-}ATSM}$ had median pseudo R^2 less than 0.03.

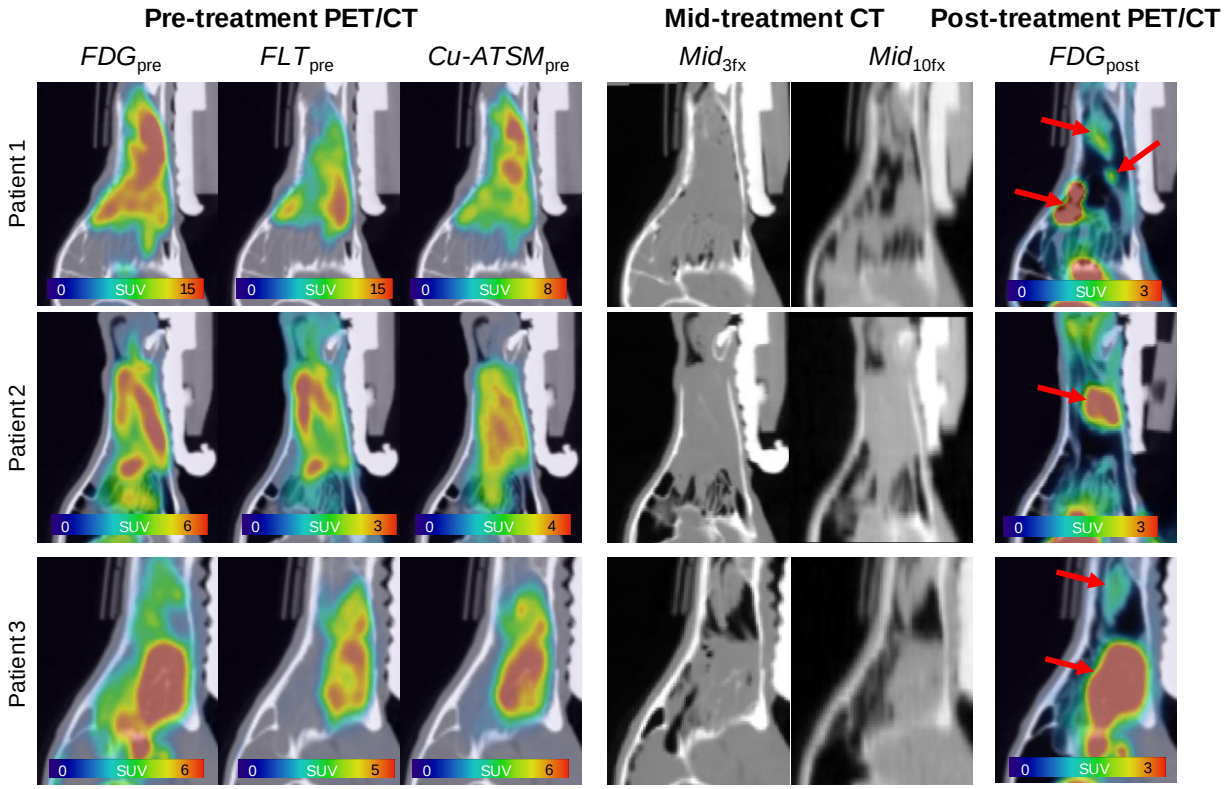

Figure 4.2. Example pre-treatment sagittal PET/CT images (*left*), CT and MVCT images at 3 and 10 fractions, respectively (*middle*), and post-treatment FDG PET/CT images (*right*) are shown for 3 example patients. The three patients demonstrate different ways by which tumors shrink during and after therapy.

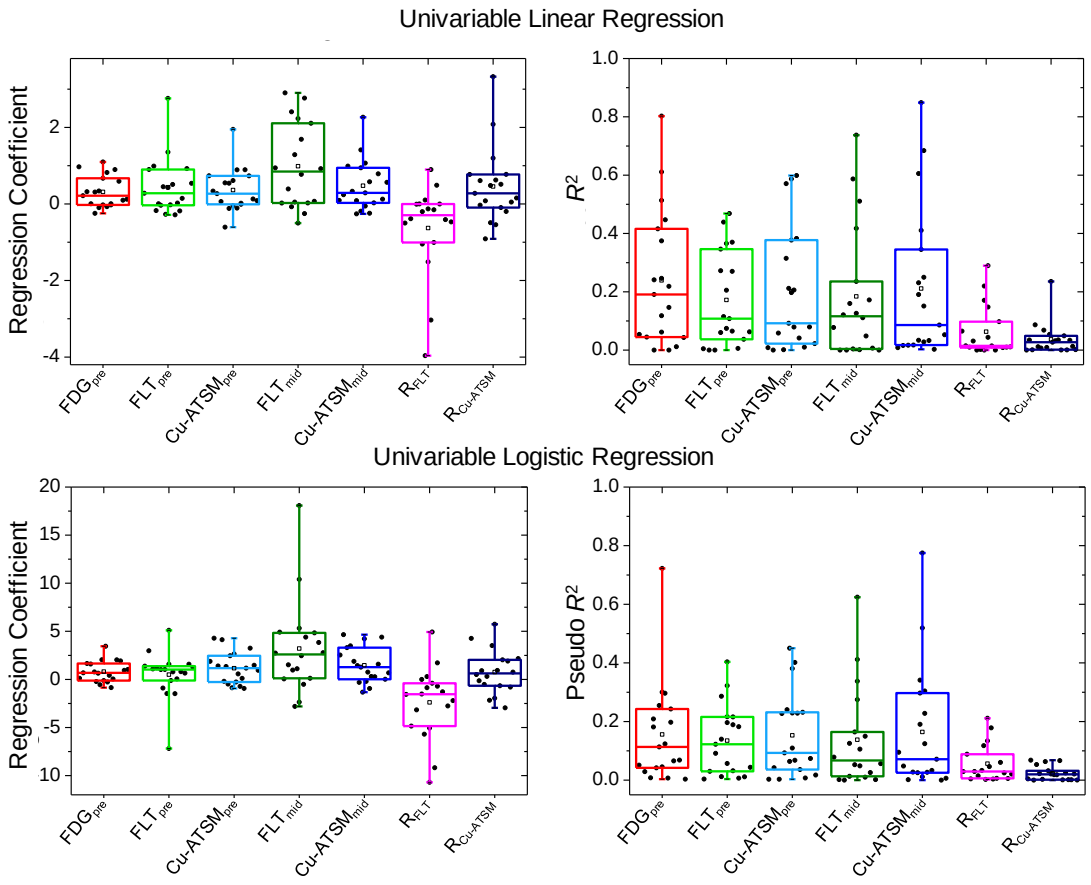

Figure 4.3. Results from simple linear (*top row*) and logistic (*bottom row*) voxel regressions for all patients. Regression coefficients (*left*) and goodness of fits (*right*) are shown.

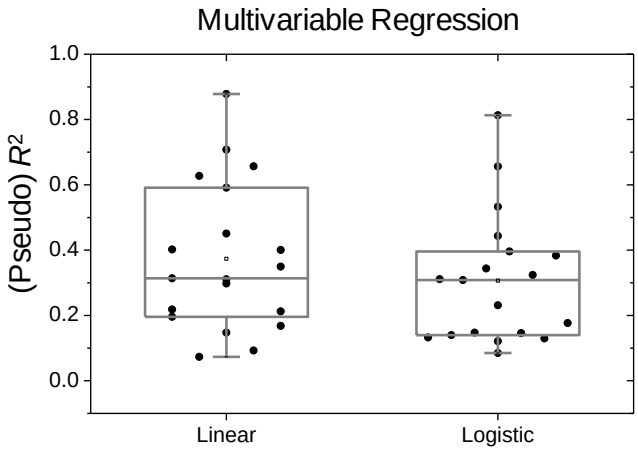

Figure 4.4. R^2 and a pseudo R^2 for each patient's multivariable linear and logistic regression models, respectively.

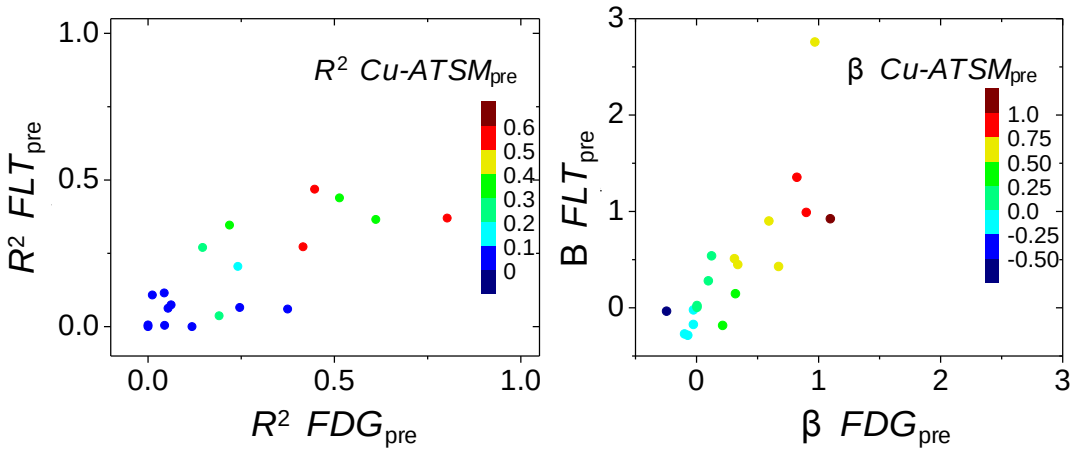

Figure 4.5. Scatter plots illustrating that different predictor variables' R^2 were correlated across patients (*left*). Likewise, regression coefficients for different predictor variables were correlated across patients (*right*). Only results from pre-treatment simple linear regression models are shown here.

Figure 4.4 shows all patients' R^2 and pseudo R^2 from multivariable linear and logistic regressions, respectively. Multivariable models had better goodness of fits than simple regression models: the median R^2 for the linear model was 0.31, and median pseudo R^2 for the logistic model was 0.24.

No clinical measures or imaging biomarkers were correlated with patients' respective R^2 ($R < 0.3$). We found that patients with low R^2 for a single predictor variable had similarly low R^2 for all predictor variables, even for multivariable models. In other words, the R^2 of different regression models (for different predictor variables) were correlated across patients ($R > 0.75$). This is illustrated for all three pre-treatment simple linear regression models in Figure 4.5. Likewise, if a patient had low regression coefficient for a single predictor variable, the other predictor variables were likely to also have low regression coefficients (see Figure 4.5).

4.3.2. Predictive modeling results

Figure 4.6 shows results from each patient's predictive modeling. For each patient, the fitted R^2 and fitted pseudo R^2 are shown—these indicate how well the models described the *other* 17 patients' data. The prediction R^2 and prediction pseudo R^2 indicate how well the prediction models performed when applied to the test patient. In general, CART outperformed the other models in fitting the patients' data,

but often had the worst performance in predicting a "new" test patient. Overall, advanced prediction models did not improve the prediction accuracy when compared to multivariable linear regression models.

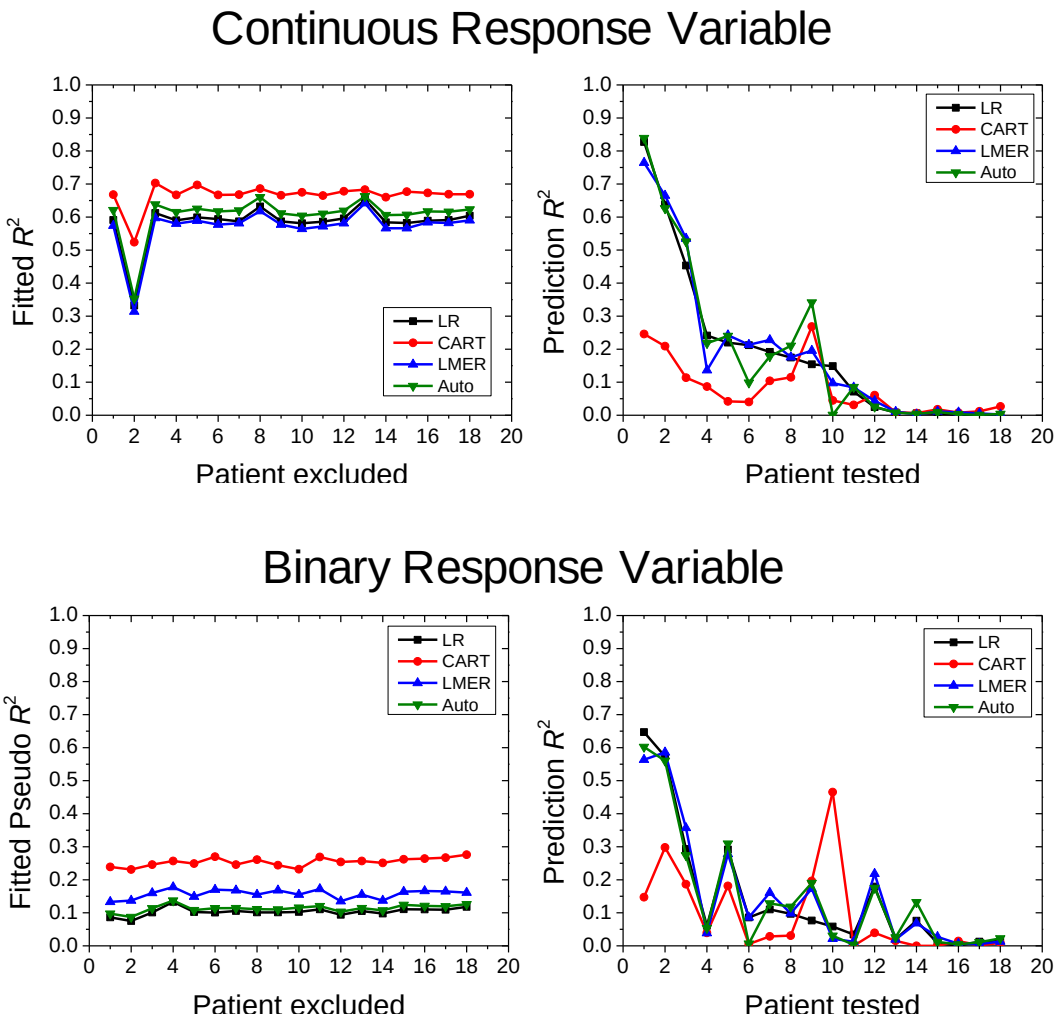

Figure 4.6. Prediction modeling results for each patient, for both continuous response variables (*top row*) and binary response variables (*bottom row*). For each patient, fitted R^2 are shown, indicating how well the four models fit the 17 *other* patients' data that they were trained on. Prediction R^2 are also shown, indicating how well the trained models predicted the response values for the test patient. Patients are sorted according to the prediction R^2 for the linear regression model. LR = multivariable linear regression; CART = classification and regression tree; LMER = linear mixed effects regression; Auto = regression with neighborhood structures.

4.4. Discussion

In this study, we used canine sinonasal tumors as models for determining which radiotracer uptake distribution — FDG, FLT, or Cu-ATSM — best correlated with location of tumor recurrence as a surrogate for measuring spatially-resolved resistance to radiation therapy. Bowen *et al.* previously published an exploratory voxel regression study evaluating 9 of the patient used in this study, and reported pre-treatment FDG uptake distributions as being the best predictor of post-treatment FDG uptake distributions (*95*). In this study, we made several additions to the methods of analysis, including the addition of mid-treatment FLT and Cu-ATSM images as predictor variables, implementing logistic regression with segmented follow-up FDG images as binary response variables (removing potential autocorrelation between pre- and post-treatment FDG), and creating advanced prediction models accounting for non-linearity, patient-level variables, and autocorrelation among neighboring voxels. We also increased the statistical power of the study by increasing the number of evaluable canine patients from 9 to 19.

Overall, we found large variability among patients in how well pre- and mid-treatment PET imaging predicted the locations of tumor recurrence. For simple regression models, FDG_{pre} had the highest median and mean R^2 values of the tested predictor variables, suggesting it might be the most suitable target for dose painting. This is in agreement with the results reported by Bowen *et al.* (*95*). On the other hand, when FDG_{post} was dichotomized and logistic regression was performed, the R^2 values for FDG_{pre} were nearly identical to those of the other predictor variable. Unsurprisingly, we found that multivariable models resulted in better goodness of fits (R^2 and pseudo R^2) than simple regression models. Regardless of regression method, however, there was a cluster of 5 patients whose R^2 were at or below 0.20. Unfortunately, patients' R^2 values were not correlated with any imaging biomarkers or clinical measures that we tested. Biomarkers that could predict which patients would "behave well" under dose painting would be valuable for selecting patients most likely to benefit from dose painting.

The interpretation and implications of a low or high R^2 for such regression models, or the thresholds at which an R^2 could be considered adequate for dose painting, are not straightforward. Bender addressed these issues using a tumor control probability model, and reported that when the voxel-based correlation coefficient between a particular imaging method and the theoretical probability of recurrence risk was greater than 0.45 (corresponding to an R^2 of 0.20), voxel-based dose painting would result in greater tumor control than uniform dose prescriptions (*32*). Clearly, the measure of post-treatment FDG SUV used in our study was not a direct measure of recurrence risk, but if we were to use an R^2 threshold of 0.20 for the simple linear regression models, we would find that roughly half of the 19 patients would benefit from dose painting. For the other half of the population, however, dose painting might actually be worse than uniform dose prescriptions. These results, of course, depend on the tracer used (see Figure 4.3), and regression method used for analysis (linear vs logistic vs multivariable), but do suggest that all patients may not be good candidates for dose painting. These results highlights the need to identify objective measures that can predict which patients would make good or poor candidates for dose painting based on a given biological imaging target.

Voxel-based predictors based on ratios of PET images from pre- to mid-treatment (R_{FLT} and $R_{Cu\text{-}ATSM}$) were not good at predicting recurrent tumor location: R^2 and pseudo R^2 values were close to 0 for simple linear and logistic regression models. We originally hypothesized that biological changes occurring early during radiation therapy might correlate to tumor resistance. This hypothesis was supported by the analysis of clinical outcome for the canine patients which is presented in Chapter 5: mid-treatment FLT SUV_{max} and relative changes in FLT SUV_{max} from pre-treatment to mid-treatment were the most predictive of progression-free survival. In this study, we did not find response maps of FLT uptake to be significant spatial predictors of residual/recurrent tumor location. A mathematical problem with ratio maps, however, is that response values can become inflated in regions with initially-low voxel values (ie, denominators close to zero), so that even fluctuations in image values due to statistical noise can appear as large response values. This may have confounded the utility of R_{FLT} and $R_{Cu\text{-}ATSM}$ as

predictors. Other techniques of quantifying spatially-resolved changes in longitudinal PET images may be more appropriate, such as absolute SUV changes (this was included in the multivariable regression models), or other methods (*184*).

Advanced predictive models did not provide an improvement over multivariable linear regression models at predicting a "new" patient's post-treatment FDG values. These prediction models were used to account for potentially confounding factors that aren't accounted for in linear regression, such as patient categorical variables, non-linearity, and autocorrelation among neighboring voxels. For the models with continuous response data, the fitted R^2 for the pooled data were generally higher than for the multivariable linear models shown in Figure 4.4 However, the better fitting did not result in high prediction accuracy, as median prediction R^2 values for the different models were less than 0.15. CART performed the best at describing the training data (see Figure 4.6) , but often having the poorest prediction performance—likely a consequence of over fitting. Overall, prediction R^2 were approximately the same as the regression R^2 shown in Figure 4.4, and contained large interpatient variability.

We observed that tumors were highly variable in their anatomical response to radiation therapy. This is demonstrated in Figure 4.2. Using during-treatment CT and MVCT imaging, we were able to observe tumor shrinkage over time. Some tumors experienced anatomical response almost immediately following the onset of IMRT, whereas others did not shrink at all during the 2-week course of IMRT. Of those that did shrink, some tumors appeared to shrink elastically: the tumor died or contracted at the edges, resulting in a single mass of residual tumor near the center. Other tumors, however, did not shrink elastically, but rather had patchy or fragmented anatomical responses, containing spatial clusters of dying tumor and spatial clusters of resistant tumor. Yet other tumors responded in manner that appeared to be a mixture of the two types. It is unclear why different tumors responded so differently during treatment. Clearly, these types of responses have implications for adaptive IMRT, in which dose distributions are shaped to match the spatial patterns of tumor anatomical (or biological) response. The tumors with patchy regions of response could indicate the existence of tumor subregions with distinct biological states.

Several other studies have correlated imaging patterns to recurrent tumor location. The studies by Aerts *et al.* and Soto *et al.* in lung and head-and-neck tumors, respectively, have already been discussed in the introduction. Abramyuk *et al*. and Shusharina *et al.* performed similar studies in 10 and 19 patients, respectively, who had lung cancer and experienced loco-regional failure following radiation therapy. Both studies found high degrees of spatial overlap between recurrence volumes and pre-treatment FDG uptake (*180, 185*). Petit *et al*. used logistic voxel regression to relate pre-treatment FDG uptake to post-treatment FDG uptake in 39 NSCLC tumors, and found increased FDG uptake at baseline predicted a greater probability of post-treatment FDG uptake (*70*). Vogelius *et al.* found that recurrent tumor was most likely to originate in the regions of elevated FDG uptake in 39 HN cancer patients undergoing radiation therapy (*100*).

A primary assumption to the methods of this study—which is a common assumption to all of the previously-mentioned spatial analysis studies—is that, following image registration, the tumor cells in a voxel location do not change or move location between pre-treatment imaging and post-treatment imaging. It is unclear how frequently this assumption is valid. Deformable registration methods attempt to account for tumor morphological changes over time, but deformable registration algorithms assume that the tumor's mass is preserved, which is not the case for tumors undergoing treatment. Canine sinonasal tumors benefit from the fact that rigid registration can be very accurate due to the surrounding bony nasal cavity, and (based on our experience) the turbinates inside the nasal cavity serve as a sort of scaffolding to hold the tumor in its place, restricting tumor movement over time. An additional limitation of the study is the degree to which post-treatment FDG uptake is a valid marker of recurrent or residual tumor, and whether it corresponds to resistant tumor. Numerous studies have found that post-treatment FDG uptake does correlate with poor clinical outcome (*186-188*), however, non-specific uptake of FDG after therapy could still be a confounding factor in this study.

4.5. Conclusion

The property of greatest importance for a dose painting imaging target is its spatial concordance with tumor resistance. In this study, we used location of residual/recurrent tumor following radiation therapy as a surrogate measure of spatially-varying resistance, against we correlated imaging patterns of three PET radiotracers. Using voxel regression models, we found that FDG, FLT, and Cu-ATSM PET were able to predict the locations of recurrence in some canine tumors, but were poor predictors of recurrence locations in other tumors. We also showed that no individual PET tracer outperformed the other PET tracers in terms of correlations with patterns of recurrence. These results highlight the need for methods of pre-selecting candidates for dose painting and for the development of better molecular imaging probes of resistance.

5. Quantitative imaging biomarkers of resistance to radiation therapy

This chapter addresses Specific Aim 2: the assessment of quantitative imaging biomarkers of resistance to radiation therapy. In this chapter, quantitative imaging biomarkers are extracted from pre- and mid-treatment FDG, FLT, and Cu-ATSM PET image, and then evaluated for their ability to predict progression-free survival following radiation therapy in the canine patients of the CIRT trial. Imaging values that correlate with resistance may help inform dose painting target definition. This work has been accepted for publication in the International Journal of Radiation Oncology • Biology • Physics (*189*)

5.1. Motivation

Outcome following radiation therapy can be highly variable across different patients, even in tumors with similar clinical presentation (*190*). The underlying mechanisms and causes of this variability are poorly understood, and treatment outcome remains difficult to predict. Better methods of predicting outcome following radiation therapy could greatly improve patient management by helping physicians better tailor treatments to patient-specific biology.

There is great interest in identifying biomarkers of tumor resistance to radiation therapy. Numerous studies have investigated genetic, molecular, and anatomical biomarkers of radiation resistance in different tumor types (*191-192*). Many of these biomarkers are biopsy-based and therefore limited by sampling, invasiveness, and intratumor heterogeneity. PET imaging, however, non-invasively provides spatially-resolved quantitative measurements of tumor biological processes. Using different PET radiotracers, different phenotypic states can be assessed and compared *in vivo*. Therefore, there is great promise for molecular imaging biomarkers to improve treatment outcomes in radiation oncology (*193*).

Given that multiple factors affect resistance to radiation therapy, a direct comparison of multiple imaging biomarkers may shed further light on the characteristics of tumor resistance. This study aimed to

concurrently evaluate the predictive value of numerous quantitative imaging biomarkers derived from multi-tracer PET imaging in tumors before and during radiation therapy. In addition to traditional quantitative PET imaging metrics (ie, standardized uptake values), advanced imaging metrics containing spatiotemporal and response information were also tested for their predictive value.

5.2. Methods and Materials

This study included 22 canine patients from the CIRT trial, including 13 adenocarcinoma patients, 7 chondrosarcoma patients, 1 squamous cell carcinoma patients, and 1 osteosarcoma patient. The imaging and treatment schedule and protocol are described in detail in section 1.5. For this study, all pre- and mid-treatment PET scans were used for each patient, as were follow-up CT scans.

5.2.1. Imaging biomarkers

Numerous imaging biomarkers were extracted from each patient's imaging set. Table 5.1 describes the imaging biomarkers used for analysis. These included the conventional SUV measures (SUV_{mean} and SUV_{max}) measured at pre-treatment and mid-treatment, as well as response and spatiotemporal variables. Response variables, quantifying the relative change from pre-treatment to mid-treatment, were calculated according to

$$R_X^T = \frac{X_{\mathrm{mid}}^T - X_{pre}^T}{X_{\mathrm{pre}}^T} \quad , \tag{5.1}$$

where X is either the SUV_{mean} or SUV_{max} of tracer T, evaluated at pre-treatment and mid-treatment. For spatiotemporal variables, voxel-based Spearman correlation coefficients (ρ) quantified the relative spatial agreement between two different tracer distributions, T_1 and T_2, at baseline (ρ_{T_1,T_2}). Spearman correlation coefficients also quantified the relative spatial stability of a tracer T from pre-treatment to mid-treatment ($\rho_{\mathrm{pre,mid}}^T$). The computation of ρ has been described previously (*139, 141*) (see sections 2.2.2 and 3.3.2).

Table 5.1. Imaging biomarker definitions.

Variable	Description
Volume	Gross tumor volume (cm^3)
SUV_{mean}	Mean SUV in the GTV
SUV_{max}	Maximum voxel SUV in the GTV
$R^{FLT}_{SUVmean}$	Fractional change in FLT SUV_{mean} from pre-treatment to mid-treatment
R^{FLT}_{SUVmax}	Fractional change in FLT SUV_{max} from pre-treatment to mid-treatment
$R^{Cu-ATSM}_{SUVmean}$	Fractional change in Cu-ATSM SUV_{mean} from pre-treatment to mid-treatment
$R^{Cu-ATSM}_{SUVmax}$	Fractional change in Cu-ATSM SUV_{max} from pre-treatment to mid-treatment
$\rho_{FDG,FLT}$	Spatial (voxel) correlation between pre-treatment FDG and FLT uptake distributions
$\rho_{FDG,Cu-ATSM}$	Spatial (voxel) correlation between pre-treatment FDG and Cu-ATSM uptake distributions
$\rho_{FLT,Cu-ATSM}$	Spatial (voxel) correlation between pre-treatment FLT and Cu-ATSM uptake distributions
$\rho^{FLT}_{pre,mid}$	Spatial (voxel) correlation between pre-treatment and mid-treatment FLT uptake distributions
$\rho^{Cu-ATSM}_{pre,mid}$	Spatial (voxel) correlation between pre-treatment and mid-treatment Cu-ATSM uptake distributions

5.2.2. Statistical analysis

Progression-free survival was assessed according to the RECIST criteria. Kaplan-Meier analysis with log-rank tests for significance were applied to the following categorical variables: dose level (42 Gy vs. 50 Gy), histologic tumor type (sarcoma vs. carcinoma), sex, and the tumor stage as defined by Adams *et al.* (*140*). For continuous variables, such as patient age and the imaging biomarkers of Table 5.1, Cox proportional hazards (PH) regression was used to assess their impact on progression-free survival. Univariable Cox PH regression was performed for each continuous variable, and hazard ratios (HR) with their respective 95% confidence intervals (CI) were calculated.

A full multivariable regression model was not developed in this study due to the limited number of patients and the high number of predictor variables. However, we investigated bivariable Cox PH regression models that contained 2 predictor variables, thus following the recommended ratio of ~10 patients per explanatory variable (*194-195*). This was done by creating regression models for all possible combinations of 2 explanatory variables, considering both categorical and continuous variables. Of the

SUV measures, only SUV_{max} was used due to the strong correlations (R>0.9) between SUV_{max} and SUV_{mean}. The best bivariable model was selected according to the Pseudo R^2 (*196*). *P* values less than 0.05 were considered statistically significant.

5.3. Results

The average time to disease progression was 14.3 months, the median was 12.5 months, and the range was 3 months to 35 months. Four cases were censored: two due to death unrelated to disease, and two who were alive without progressive disease at the time of the analysis, but had the longest progression-free intervals.

Figure 5.1 shows PET/CT images from an example patient during the course of therapy. Figure 5.2 shows results from Kaplan-Meier analysis for categorical variables. Dose level, histologic tumor type, sex, and tumor stage were found not to be significant predictors of time to progression after radiation therapy. Table 5.2 summarizes the results of univariable Cox PH regression for continuous variables. Large tumor volume (HR [95% CI] = 1.01 [1.00, 1.02]; *P*=0.011), high mid-treatment FLT SUV_{mean} (2.76 [1.19, 6.40]; *P*=0.018), and high mid-treatment FLT SUV_{max} (1.36 [1.09, 1.68]; *P*=0.006) were found to be significant independent predictors of worse outcome. Positive $R^{\mathrm{FLT}}_{\mathrm{SUVmean}}$ values (ie, increases in FLT SUV_{mean} from pre-treatment to mid-treatment) were significantly associated with better clinical outcome (0.11 [0.02, 0.64]; *P*=0.013). Figure 5.2 also shows Kaplan-Meier plots (for display purposes only) for the group of continuous variables found to be significant predictors according to univariable Cox PH regression analysis.

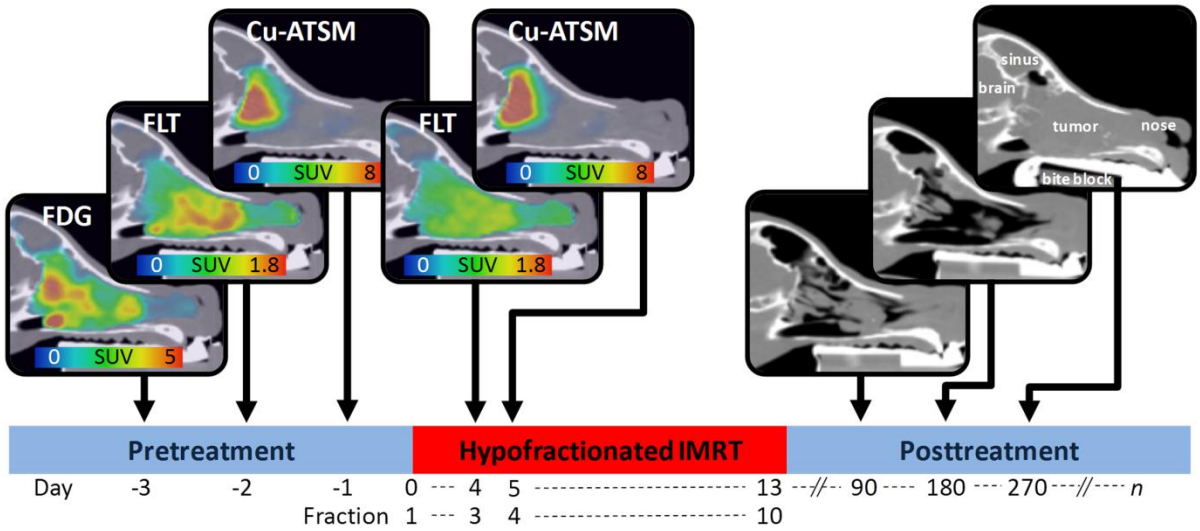

Figure 5.1. Patients underwent pre-treatment FDG, FLT, and Cu-ATSM PET/CT imaging (in no particular order). Mid-treatment FLT and Cu-ATSM PET/CT scans were acquired before fractions 3 and 4, respectively. Following therapy, CT scans were acquired at 3, 6, and 9 months, and at time of recurrence (up until progressive disease was detected). Sagittal slices of a canine patient's PET/CT images are shown above.

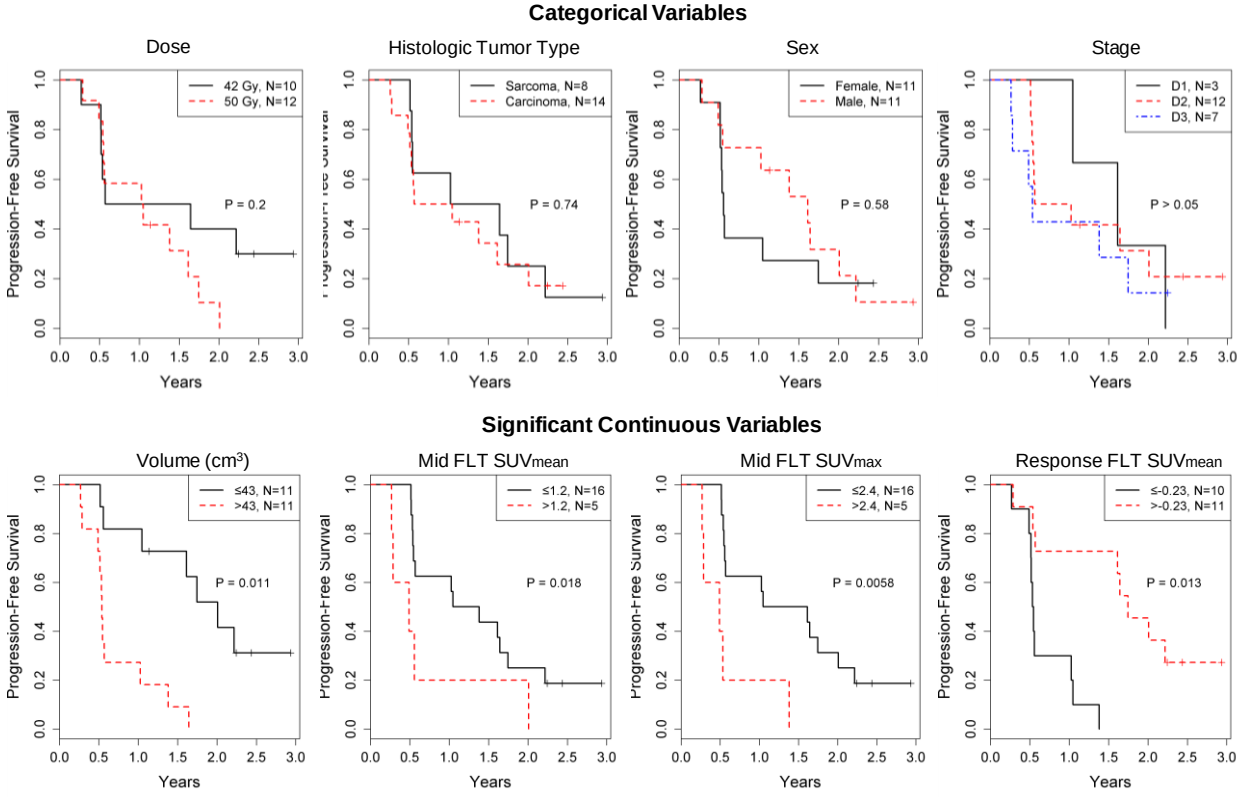

Figure 5.2. *Top:* Results of Kaplan-Meier analyses with log-rank tests for categorical variables. Categorical variables were not predictive of outcome. *Bottom:* For display purposes only, variables that were significant predictors of outcome according to Cox proportional hazards (PH) regression were dichotomized using an optimal cut point, and plotted according to Kaplan-Meier method. *P* values are from Cox PH regression.

Table 5.2. Results of univariable Cox proportional hazard regression for continuous variables against progression-free survival.

Variable	Hazard Ratio	95% Confidence Interval	*P*
Volume (cm^3)	1.01	[1.00, 1.02]	**0.011**
Age	1.01	[0.87, 1.17]	0.911
Pre FDG*			
SUV_{mean}	1.12	[0.91, 1.40]	0.287
SUV_{max}	1.09	[0.99, 1.20]	0.080
Pre FLT			
SUV_{mean}	1.07	[0.86, 1.35]	0.543
SUV_{max}	1.02	[0.95, 1.01]	0.565
Pre Cu-ATSM			
SUV_{mean}	1.28	[0.84, 1.94]	0.245
SUV_{max}	1.08	[0.95, 1.23]	0.226
Mid FLT			
SUV_{mean}	2.76	[1.19, 6.40]	**0.018**
SUV_{max}	1.36	[1.09, 1.68]	**0.006**
Mid Cu-ATSM			
SUV_{mean}	1.63	[0.88, 3.02]	0.124
SUV_{max}	1.06	[0.96, 1.17]	0.288
$R^{FLT}_{SUVmean}$	0.11	[0.02, 0.64]	**0.013**
R^{FLT}_{SUVmax}	0.15	[0.02, 1.11]	0.064
$R^{Cu-ATSM}_{SUVmean}$	0.63	[0.10, 3.97]	0.620
$R^{Cu-ATSM}_{SUVmax}$	0.94	[0.19, 4.58]	0.941
$\rho_{FDG,FLT}$	5.08	[0.41, 62.2]	0.204
$\rho_{FDG,Cu-ATSM}$	0.99	[0.04, 25.8]	0.997
$\rho_{FLT,Cu-ATSM}$	3.82	[0.62, 23.7]	0.150
$\rho^{FLT}_{pre,mid}$	3.28	[0.17, 61.6]	0.428
$\rho^{Cu-ATSM}_{pre,mid}$	2.36	[0.02, 275]	0.724

* see Table 5.1 for variable definitions

Table 5.3 presents the two bivariable models with the highest Pseudo R^2. Both models indicate that significantly worse outcome was associated with large reductions in FLT uptake (ie, negative response values) in combination with high mid-treatment FLT SUV_{max}. The relationships between patients' clinical outcome and their various FLT measures are illustrated in the scatter plots of Figure 5.3.

Table 5.3. The two bivariable models with the highest Pseudo R^2.

Variable	Hazard Ratio	*P*	Pseudo R^2
Model 1			0.44
Mid FLT SUV_{max}*	1.28	0.022	
$R^{FLT}_{SUVmean}$	0.17	0.041	
Model 2			0.43
Mid FLT SUV_{max}	1.38	0.002	
R^{FLT}_{SUVmax}	0.11	0.042	

* see Table 5.1 for variable definitions

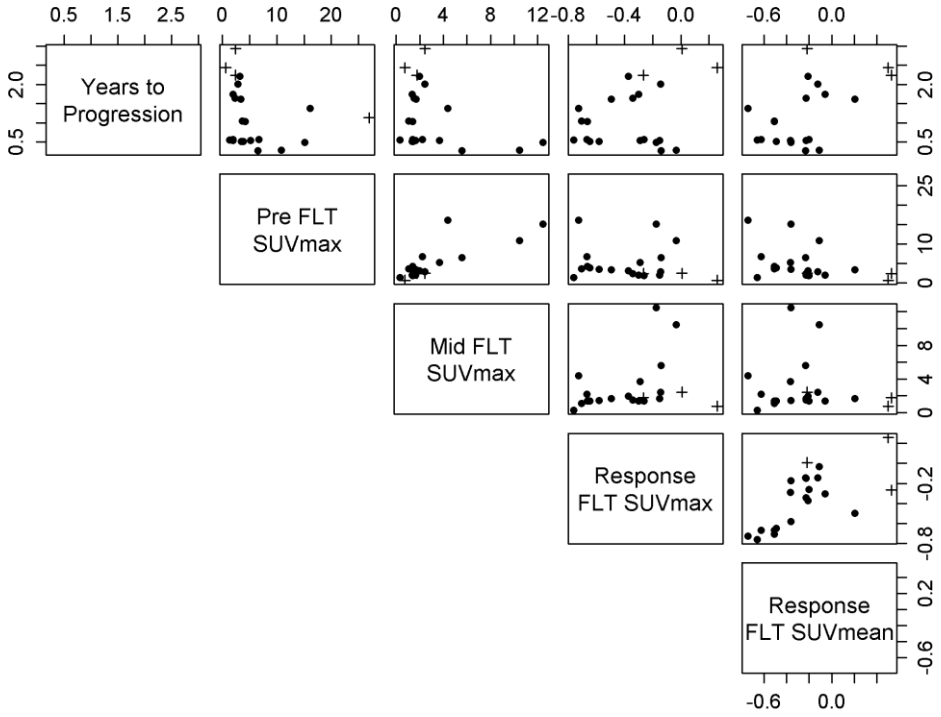

Figure 5.3. Scatter plot matrix illustrating the relationships between patients' treatment outcome (*top row*) and various FLT measures. Each column and row corresponds to a different measure, as indicated by the labels in the diagonals. Crosses (+) indicate censored patients.

5.4. Discussion

Using multi-tracer PET imaging in canines with spontaneous tumors, we were able to directly compare numerous imaging biomarkers as predictors of time to progression after radiation therapy. Motionless imaging and accurate image registration enabled us to extract non-conventional spatiotemporal imaging measures, which we compared against conventional SUV measures for their predictive value.

The best predictors of time to progression after radiation therapy were FLT-based biomarkers. FLT response and mid-treatment FLT SUV were both found to be significant predictors of outcome in univariable and multivariable analysis. Whereas high mid-treatment FLT SUV was found to be associated with worse clinical outcome, the relationship between FLT-response and patient outcome was counter to our expectations: tumors with large relative reductions in FLT uptake had worse outcomes than tumors with small relative changes. FLT response during radiation therapy has been previously investigated in humans (*120, 197-200*); unfortunately, several of these studies are small and there is no consistent picture emerging at this point in time. In a series of 12 lung cancer patients, Trigonis *et al.* found that higher mid-treatment FLT, but not baseline FLT, was associated with worse local-regional control, which is consistent with our findings. However, FLT response was not a significant predictor of outcome (*199*). In another small study, Wieder *et al.* did not find significant relationships between histopathological tumor response and FLT uptake at baseline or at mid-treatment in 10 rectal cancer patients undergoing neoadjuvant chemoradiotherapy (*198*). Hoeben *et al.* found that for 33 head-and-neck cancer patients, early FLT response during radiation therapy was not predictive of patient outcome (*120*). However, when they included 15 chemoradiotherapy patients in their analysis, large reductions in FLT SUV became associated with better 3-year disease-free survival (but not overall survival). For tumors treated with chemotherapies, studies have generally found that large FLT reductions during treatment predicts better clinical outcome (*201-202*). The heterogeneity between the findings of these studies could be due to their limited statistical power compounded by differences in treatment schedules (hypofractionated vs.

conventional), imaging time points (our patients were imaged after the second fraction, including a weekend break), treatment type (radiotherapy alone vs. chemoradiotherapy), tumor histology, and species.

It is unclear what radiobiological principles are driving the relationships between FLT biomarkers and patient outcome. It is not surprising that baseline FLT uptake was not significantly associated with clinical outcome in this study, as high baseline proliferation rates have been previously shown to be associated with both favorable and poor clinical outcome following radiation therapy (*116*). However, we did find that high FLT uptake at mid-treatment was associated with worse clinical outcome. It is tempting to speculate that these tumors could have contained a greater number of remaining viable cells after receiving ~10 Gy of radiation dose, or the population of surviving cells in these tumors were rapidly proliferating. We also found that tumors with large *reductions* in FLT uptake at mid-treatment relative to baseline had a shorter time to progression than tumors with small changes or increases in FLT uptake, and this relationship was independent of pre-treatment or mid-treatment FLT uptake levels (see Figure 5.3). This is consistent with a hypothesis where tumors with pronounced responses at the beginning of treatment could be more likely to regrow rapidly following radiation therapy, resulting in shorter progression-free intervals. Indirect support for this hypothesis comes from the recent study by Brink *et al.*, who found that marked tumor regression during fractionated radiation therapy for non-small cell lung cancer was associated with worse clinical tumor outcome in a series of 99 patients (*203*).

In addition to FLT PET biomarkers, tumor volume was a predictor of adverse clinical outcome following radiation therapy. Dose level, histology, sex, age, and tumor stage were not significant predictors of outcome. Past veterinary studies have found conflicting results on the prognostic significance of tumor histology, patient age, and tumor stage in canine nasal tumors following radiation therapy (*140, 204-205*). It is possible that the low patient number, and thus the low statistical power, prevented us from detecting predictive relationships that would have been observed in a larger population. Interestingly, we did not find Cu-ATSM and FDG biomarkers to be significant predictors of outcome; although, FDG SUV_{max} was borderline significant (P=0.08).

None of the spatial imaging biomarkers were significantly associated with patient outcome. The baseline voxel correlation coefficients ($\rho_{\mathrm{FDG,FLT}}$, $\rho_{\mathrm{FDG,Cu-ATSM}}$, and $\rho_{\mathrm{FLT,Cu-ATSM}}$) represented how similar the spatial distributions of the three tracers were, so that a low correlation coefficient indicated spatial heterogeneity of phenotypes within a tumor (*141*). We hypothesized that higher PET heterogeneity would predict worse response to therapy; however, this was not supported by our analysis. The voxel correlations from pre-treatment to mid-treatment ($\rho_{\mathrm{pre,mid}}^{\mathrm{Cu-ATSM}}$ and $\rho_{\mathrm{pre,mid}}^{\mathrm{FLT}}$) represent the spatial stability of Cu-ATSM and FLT uptake distributions during treatment. We recently showed that values of $\rho_{\mathrm{pre,mid}}^{\mathrm{Cu-ATSM}}$ were very high for these patients, with an average correlation of 0.88 (*139*). Values of $\rho_{\mathrm{pre,mid}}^{\mathrm{FLT}}$ were also high (0.79), but significantly lower than $\rho_{\mathrm{pre,mid}}^{\mathrm{Cu-ATSM}}$. We hypothesized that larger spatial stability of a tumor's Cu-ATSM or FLT maps during treatment might be associated with tumor resistance to radiation. However, we did not find PET spatial stability to be significantly associated with clinical outcome.

The cost and logistics of conducting multiple scans at baseline and during therapy restricted the total sample size in this exploratory study. This in turn limited our ability to investigate biomarkers in subpopulations of tumors (eg, sarcomas), and to create a complex multivariable model. Multivariable models can become unstable when there are less than 10 observations (ie, patients) per explanatory variable (*194-195*). On the other hand, it is important to assess whether different explanatory variables contain redundant or complementary predictive information. For example, many quantitative PET features have been shown to be highly correlated to tumor volume (*206*). Therefore, we tested bivariable models, selected according to a goodness of fit statistic. Another caveat of the study is the large number of hypotheses tested in this study, which increases the likelihood of type I error. Consequently, these results should be considered as hypothesis-generating, and need to be tested in a larger cohort.

5.5. Conclusions

Using extensive imaging of spontaneous tumors in canines, we explored a number of molecular imaging biomarkers as potential predictors of resistance to radiation therapy. In addition to tumor volume, pronounced tumor proliferative response measured with FLT PET, especially when associated with high residual FLT PET at mid-treatment, was a predictive biomarker of poor outcome following radiation therapy. This suggests that FLT imaging, especially FLT imaging performed during radiation therapy, may be useful for identifying tumor resistance, and further investigation is warranted into the relationship between longitudinal FLT imaging during treatment and resistance to radiation therapy. Neither FDG PET nor Cu-ATSM PET were significant predictors of outcome in the CIRT trial. Biomarkers of spatial stability or correlations between tracers were also not predictive of outcome.

6. Characterization of non-uniform dose prescriptions based on different biological targets

This chapter addresses Specific Aim 3, which is to determine the feasibility of creating and delivering dose painting prescriptions and plans. In this chapter, we created and characterized dose painting prescription maps based on FDG, FLT, and Cu-ATSM PET in human head-and-neck (HN) tumors. We also describe the degree to which dose can be added to high-uptake tumor subregions by sacrificing dose to low-uptake subregions. Furthermore, we tested how accurately voxel-wise dose painting plans based on Cu-ATSM PET in canine tumors can be delivered via tomotherapy.

6.1. Motivation

Dose painting allows for dose redistribution rather than dose escalation. Dose redistribution is accomplished by lowering dose in radiosensitive tumor subvolumes and transferring that dose to radioresistant tumor subvolumes, meanwhile preserving the overall mean tumor dose. This is important because tumor dose escalation can also lead to increased normal tissue toxicities. The degree of dose trade-off between sensitive and resistant tumor subvolumes for dose escalation has yet to be characterized in literature.

Creating voxel-wise dose painting prescriptions requires a prescription function — a mathematical function that converts image voxel values into prescribed voxel doses (*75*). The optimal dose painting prescription method remains unknown. The majority of prescription methods that have been proposed in literature or implemented in clinical trials have assumed that all tumor voxels receive some minimum dose (ie, a uniform base dose), on top of which a non-uniform boost is added such that the voxel boost doses are linearly proportional to voxel image values. Substantial differences exist, however, between the constraints used in the various linear prescription methods. For example, in a HN dose painting trial from Ghent University, patient prescriptions were such that target volumes received a

minimum of 72.5 Gy, with maximum voxel doses constrained to either 90.9 Gy or 95.9 Gy (*65, 67*). Other studies have used different minimum and maximum dose constraints (*43, 51, 73*). Some planning studies have developed prescription methods that constrain the mean tumor dose instead of constraining the maximum voxel dose (*31, 55, 68*). For example, Deveau *et al* and Korreman *et al* evaluated dose painting plans with base doses of 60 Gy and mean boosts of 30 Gy, redistributed according to PET voxel intensity values (*27, 81*).

It is important to characterize different dose painting prescription methods, as the optimal method of dose painting remains unknown despite ongoing clinical trials. Previous studies have described the feasibility of dose painting treatment planning and optimization for various imaging targets (*28-29, 43*), and its sensitivity to various treatment planning parameters (*27, 68, 81*). A characterization of how the choices of imaging target and prescription function parameters impact dose prescriptions has not been previously performed. The goal of this study was to evaluate how non-uniform dose boosts would be distributed within HN tumors for various degrees of boosting, for different PET radiotracers, and for different prescription methods. Additionally, we aimed to characterize the dosimetric trade-off between low-uptake and high-uptake tumor subvolumes. Finally, we demonstrate the accuracy of dose painting delivery via tomotherapy. This work can help inform the development of protocols for future dose painting trials in HN tumors.

6.2. Methods

6.2.1. Patients

The study included 10 patients with head-and-neck squamous cell carcinoma (HNSCC). All patient imaging protocols were approved by Institutional Review Board and use of experimental tracers was approved by the radiation Drug Research Committee at the University of Wisconsin.

6.2.2. Imaging

Imaging protocols have been described in a previous report (*149*). Briefly, patients underwent PET/CT imaging with radiotracers FDG, FLT, and Cu-ATSM prior to chemoradiation. PET/CT scans were acquired on separate days over a period of less than 2 weeks. Patients were scanned on a Discovery LS PET/CT scanner (GE Healthcare, Waukesha, WI), with thermoplastic masks used for immobilization during FLT and Cu-ATSM scans. FDG PET scans were whole-body acquisitions, 1 frame per bed position, 5 minutes per frame, acquired 40-60 minutes after injection of 5.2 MBq/kg. FLT PET acquisitions consisted of 3 frames over a single bed position, 10 minutes per frame, acquired 60 minutes after injection of 150 MBq. Cu-ATSM acquisitions consisted of 3 frames over a single bed position, 15 minutes per frame, acquired 120-180 minutes after injection of 110 MBq. One patient did not receive an FLT PET/CT scan, and one patient did not receive a Cu-ATSM PET/CT scan.

PET images were reconstructed with CT attenuation correction using 3D ordered-subset expectation-maximization (2 iterations, 28 subsets, 5 mm full-width-at-half-max (FWHM) loop-filtration, and 3 mm FWHM post-filtration). The image grid was 128 × 128 × 35, with 3.91 × 3.91 × 4.25 mm^3 voxel sizes. Voxel activity values were converted to standardized uptake values (SUVs) for analysis. The gross tumor volume (GTV) was contoured by a radiation oncologist using treatment planning contrast-enhanced CT and FDG PET images. The GTV was expanded by 2 mm to better conform to the uptake distributions of all three PET radiotracers, yielding the dose painted volume (DPV). All dose painting prescriptions were performed in the DPV. FLT and Cu-ATSM PET/CT images were rigidly registered to the treatment planning CT, and DPVs were propagated to each PET image.

6.2.3. Dose prescriptions

Two voxel-based dose prescription methods for non-uniform boosting were considered: the redistribution method and the max-dose method. Both methods assumed the DPV received some uniform base dose —the minimum dose received by all voxels in the DPV. This is illustrated in Figure 6.1. On top of the base dose, a non-uniform boost was added, such that

$$D_{\mathrm{i}} = D_{\mathrm{base}} + B_{\mathrm{i}} \,, \tag{6.1}$$

where D_{i} is the dose prescription to voxel i, D_{base} is the base (or minimum) dose to the DPV, and B_{i} is the boost to voxel i. For both prescription methods, B_{i} was linearly proportional to the PET SUV value at voxel i.

For the redistribution method, the boost was constrained to have a fixed mean dose (B_{mean}) (*47*). As B_{mean} and the minimum voxel dose (D_{base}) were both constrained, the maximum voxel boost dose (B_{max}) delivered to the tumor varied among patients according to the unique distributions of voxel SUVs for each patient. For the redistributions method, the prescription function for the boost dose to a tumor was

$$B_{\mathrm{i}} = \frac{\mathrm{SUV_i}}{\mathrm{SUV_{mean}}} B_{\mathrm{mean}} \,, \tag{6.2}$$

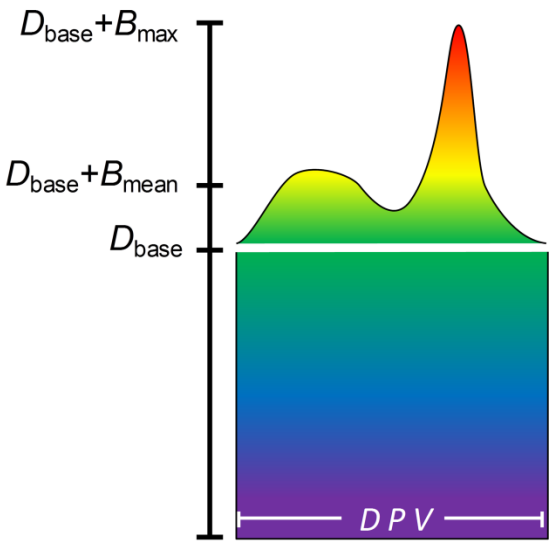

Figure 6.1. Tumor dose was prescribed such that all DPV voxels received a base dose (D_{base}), on top of which a non-uniform boost was added. Depending on the prescription method, the mean boost (B_{mean}) or maximum boost (B_{max}) dose was constrained.

where B_{i} is the boost dose to voxel i, , $\mathrm{SUV_i}$ is the SUV at voxel i, $\mathrm{SUV_{mean}}$ is the mean SUV in the DPV, and B_{mean} is the mean boost dose prescribed to the DPV.

For the max-dose method, both B_{max} and D_{base} were constrained. Consequently, all tumors had the same B_{max}, but the mean boost dose, B_{mean}, varied across patients according to the unique distributions of voxel SUVs for each patient. The prescription function for a non-uniform boost using the max-dose method was

$$B_{\mathrm{i}} = \frac{\mathrm{SUV_i}}{\mathrm{SUV_{max}}} B_{\mathrm{max}}, \tag{6.3}$$

where SUV_{max} is the maximum voxel SUV in the DPV, B_{max} is the maximum boost dose allowed for a voxel, and B_i and SUV_i are as previously defined. This method results in the voxel with highest uptake (i.e., SUV_{max}) receiving a boost of B_{max}. A variant of this method has been used in previous dose painting clinical trials (*65*, *73*).

6.2.4. Prescription analysis

For each patient, theoretical voxel-wise prescriptions were created for each of the three tracers using both redistribution and max-dose prescription methods. For the redistribution method, resulting boost dose prescriptions are reported as fractions of B_{mean} so that results can be applied to any arbitrary value of B_{mean}. Likewise, for the max-dose method, resulting boost prescription maps were normalized by B_{max}, so that results can be applied to any arbitrary value of B_{max}. Prescription dose-volume histograms (PDVHs) were created to illustrate how boost prescription maps would be distributed inside the DPV, analogous to conventional dose-volume histograms but for prescriptions. Probability maps of PDVHs were also generated to show patient variability in dose-volume relationships; these were created by binning PDVHs and fitting Weibull distributions to the 10 (or 9) patients' PDVH values at each bin. Weibull probability distributions were used because of their flexibility in fitting different distribution shapes at different points along the PDVHs.

The sensitivity of the boost prescription maps to the contouring of the DPV was also assessed. For each patient, the DPV mask and PET images were resampled from 128×128 to 256×256, then the DPV was expanded by a single layer of voxels to create the DPV_{plus}, or contracted by a single layer of

voxels to create the DPV_{minus}. Nearest neighbor resampling was used so as to not change PET image gradients. For both cases, new dose painting boost prescription maps were generated as described above and compared to the original prescriptions.

6.2.5. Example prescriptions

Example dose prescriptions were created for the HN patients using clinically-relevant values of B_{mean}, B_{max}, and D_{base}. For the redistribution method, a D_{base} of 72.5 Gy was used with a B_{mean} of 8.4 Gy — these values were loosely adapted from Duprez *et al* (*65*). For the max-dose method, a base dose of 72.5 Gy was used with a B_{max} of 18.4 Gy — these values were also derived from Duprez *et al*. Prescriptions were then repeated such that the dose modulation was doubled. For the redistribution method, the D_{base} was lowered to 64.1 Gy and the B_{mean} was doubled to 16.8 Gy (resulting in the same mean tumor dose — 80.9 Gy). For the max-dose method, the D_{base} remained at 72.5 Gy and B_{max} was doubled to 36.8 Gy.

6.2.6. Dosimetry using canine data

For evaluating the feasibility of planning and delivering dose painting plans, Cu-ATSM images from five canine patients from the CIRT trial were used to create simulated dose painting plans, which were then delivered via tomotherapy. For imaging details of the canine patients, please refer to section 1.5. Dose painting prescriptions were created inside the GTV according to the following constraints: 1) D_{base} was constrained to 4.2 Gy per fraction, 2) B_{mean} was constrained to 0.8 Gy per fraction for a total

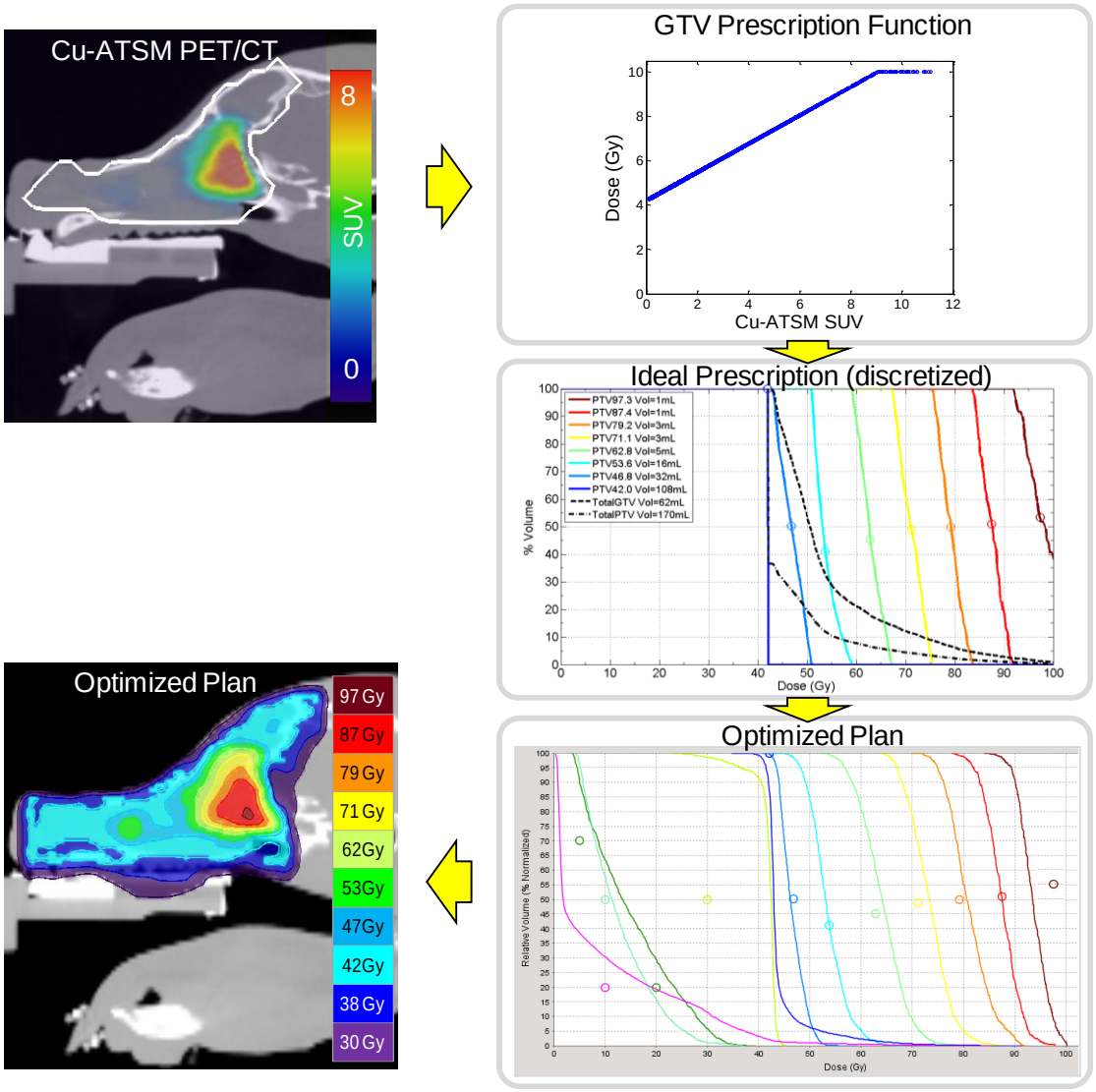

Figure 6.2. For canine patients, Cu-ATSM images were converted to dose prescriptions using a linear function (capped at 10.0 Gy per fraction), which were discretized into 8 nested contours, and then transferred to tomotherapy treatment planning system for optimization.

mean dose of 5.0 Gy per fraction, and 3) if B_{max} exceeded 10.0 Gy per fraction, iterative methods were used to cap voxel prescriptions to 10.0 Gy per fraction while preserving the B_{mean} of 0.8 Gy per fraction (see Figure 6.2 for an example). The PTV was uniformly prescribed to 4.2 Gy per fraction. Voxel dose prescriptions were converted into 8 contours representing dose levels and imported into tomotherapy treatment planning system for optimization, following the methods outlined by Deveau *et al.* (*27*). One fraction from each optimized plan was delivered to the tomotherapy phantom using 1.05 cm jaw width

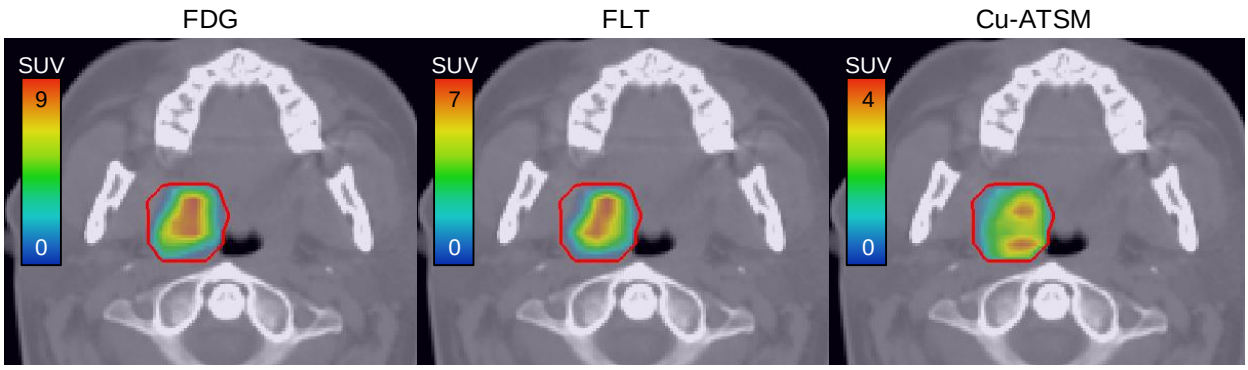

Figure 6.3. Axial slices from a patient's FDG, FLT, and Cu-ATSM PET/CT images. The DPV is outlined in red.

and 0.43 pitch. Absolute and relative measurements were performed with ion chamber and EDR2 film, respectively.

6.3. Results

Figure 6.3 shows example images of axial slices from a patient's FDG, FLT, and Cu-ATSM PET/CT scans. For many tumors, FLT uptake patterns were similar to FDG uptake patterns.

Figure 6.4 illustrates how non-uniform *boost* prescription maps were distributed within the DPV, plotted as fractions of an arbitrary fixed B_{mean} (redistribution method) or B_{max} (max-dose method),

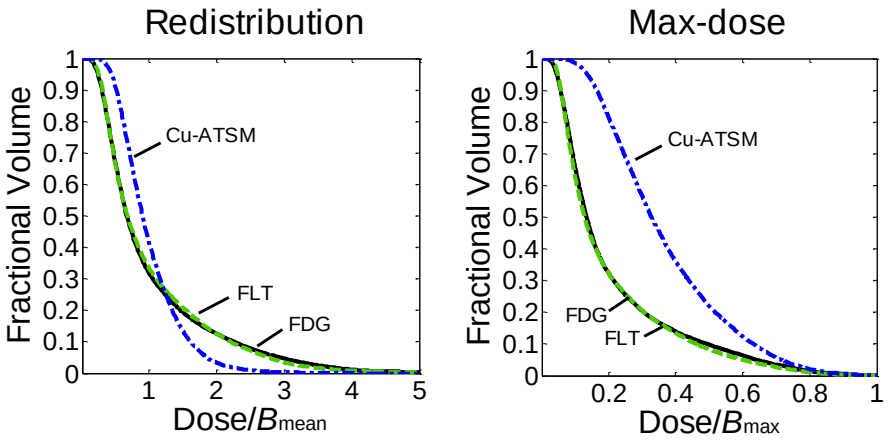

Figure 6.4. Population-averaged PDVHs representing how a boost dose would, on average, be prescribed in the DPV using FDG (*black*), FLT (*green*), and Cu-ATSM (*blue*) PET for dose painting. Results from the redistribution method (*left*) and max-dose method (*right*) are shown as fractions of arbitrary mean boosts (B_{mean}) and maximum voxel boost doses (B_{max}), respectively.

averaged across all patients. PDVHs for FDG and FLT were nearly identical across the population, whereas Cu-ATSM PDVHs had steeper falloffs (ie, greater dose uniformity in the DPV). Figure 6.5

shows probability maps of PDVHs for each PET tracer and prescription method, illustrating the variability in boost prescription maps among patients for both prescription methods. The color wash represents the probability of a patient's PDVH occurring at that location, normalized by the maximum probability.

For the redistribution method, we found that average B_{max} values for FDG and FLT prescriptions were about 5.2 times greater than B_{mean}. Cu-ATSM boost prescription maps had lower B_{max} values than FDG and FLT boosts: the average B_{max} for Cu-ATSM plans was only 2.9 times greater than B_{mean} (see Table 6.1). As illustrated in Figure 6.4, only small fractions of tumor volumes were boosted to very high doses: for FDG and FLT prescriptions, 5% of the DPV was boosted above $3\times B_{mean}$, whereas in Cu-ATSM prescriptions, 5% of the DPV was boosted above only $1.8\times B_{mean}$.

Using the max-dose prescription method with an arbitrary B_{max}, Cu-ATSM boosts had higher average B_{mean} than FDG and FLT boosts. Table 6.2 shows the population-averaged B_{mean} and the population-averaged median boost dose (B_{median}) as fractions of B_{max}. The average B_{mean} was 21% of B_{max} for FDG plans, 20% of B_{max} for FLT plans, and 37% of B_{max} for Cu-ATSM plans.

Table 6.1. Population averages and standard deviations of maximum voxel boost doses, normalized by a fixed mean boost dose, calculated using the *redistribution prescription method* with three different ROI sizes.

ROI	Average B_{max}/B_{mean}		
	FDG prescriptions	FLT prescriptions	Cu-ATSM prescriptions
DPV	5.1 ± 1.4	5.3 ± 1.6	2.9 ± 0.7
DPV_{plus}	5.9 ± 1.5	6.1 ± 1.7	3.2 ± 0.8
DPV_{minus}	4.4 ± 1.2	4.6 ± 1.5	2.6 ± 0.7

B_{mean} = mean boost dose to DPV; B_{max} = maximum voxel boost dose; DPV_{plus} = DPV expanded by 1 voxel layer; DPV_{minus} = DPV contracted by 1 voxel layer

Table 6.2. Population averages and standard deviations of mean and median boost doses, given as fractions of a fixed maximum voxel boost dose, calculated using the *max-dose prescription method* with three different ROI sizes.

ROI	FDG prescriptions	FLT prescriptions	Cu-ATSM prescriptions
DPV			
B_{mean}/B_{max}	0.21 ± 0.05	0.20 ± 0.05	0.37 ± 0.08
B_{median}/B_{max}	0.13 ± 0.04	0.13 ± 0.04	0.33 ± 0.09
DPV_{plus}			
B_{mean}/B_{max}	0.18 ± 0.04	0.17 ± 0.04	0.33 ± 0.08
B_{median}/B_{max}	0.11 ± 0.03	0.11 ± 0.02	0.30 ± 0.08
DPV_{minus}			
B_{mean}/B_{max}	0.24 ± 0.06	0.24 ± 0.07	0.40 ± 0.09
B_{median}/B_{max}	0.17 ± 0.06	0.18 ± 0.06	0.37 ± 0.11

B_{mean} = mean boost dose; B_{max} = maximum voxel boost dose; B_{median} = median boost dose; DPV_{plus} = DPV expanded by 1 voxel layer; DPV_{minus} = DPV contracted by 1 voxel layer

Figure 6.6 illustrates how dose painting prescriptions change when uncertainty is introduced in definition of the dose painting target volume. For the redistribution method, the B_{max} values changed by approximately 15% for FDG and FLT prescriptions, and by approximately10% for Cu-ATSM prescriptions (see Table 6.1). For the max-dose method, B_{mean} and B_{median} changed by approximately 20% for FDG and FLT prescriptions, and by about 10% for Cu-ATSM prescriptions (see Table 6.2).

Figure 6.7 shows an example patient's SUV histograms, as well as the patient's PDVHs when clinically-relevant values of D_{base}, $B_{mean,}$ and B_{max} were used. In this patient, FDG and FLT SUV histograms were similarly skewed to the right, whereas Cu-ATSM SUV histograms were less skewed. This was a general trend observed in the patient population (the average skewness coefficients for SUV

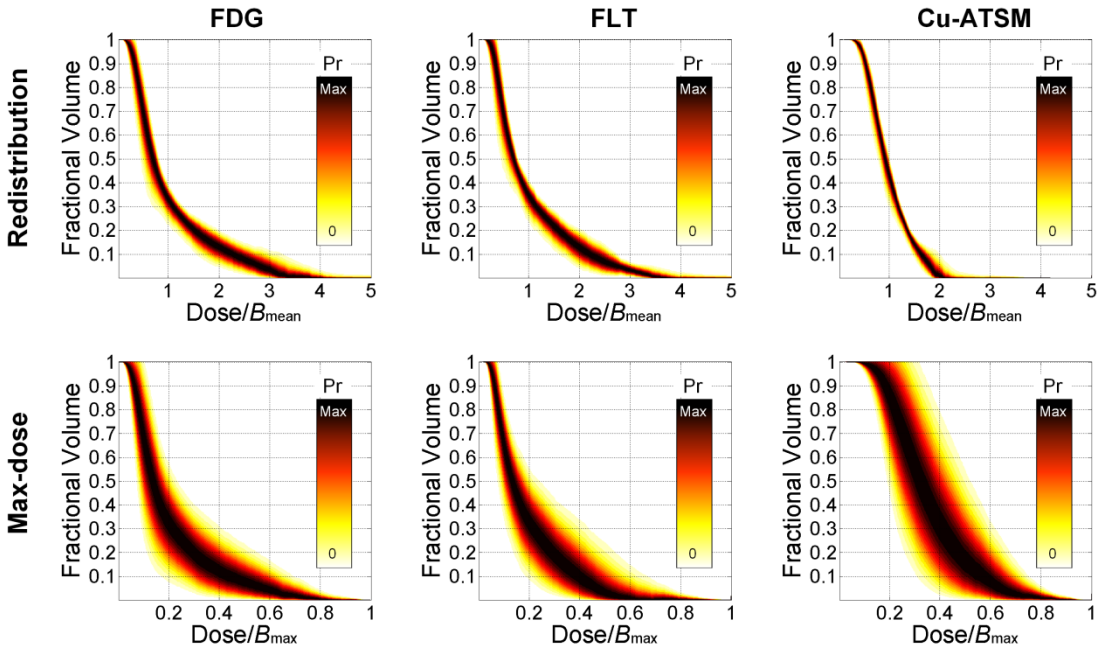

Figure 6.5. Probability maps representing how a boost dose would be distributed in the DPV using different tracers. The redistribution prescription method (*top row*) constrains the mean boost dose (B_{mean}). The max-dose method (*bottom row*) constrains the maximum voxel dose (B_{max}). Probabilities were calculated by fitting a Weibull distribution to the 10 patients' PDVHs, and the color wash represents the probability of a patient's PDVH occurring at that location, normalized by the maximum probability.

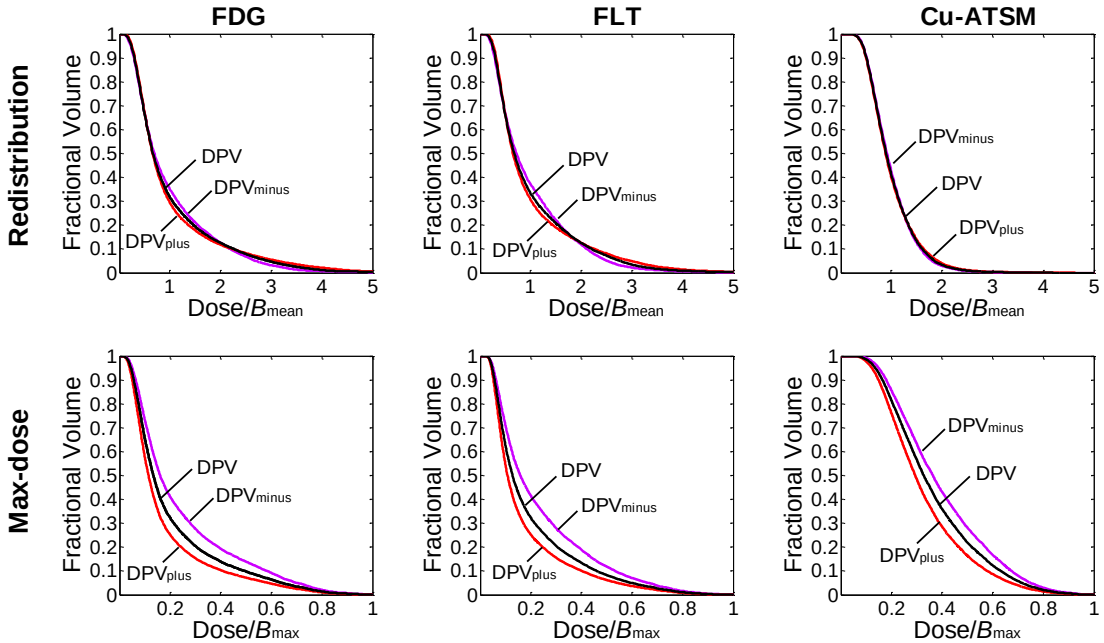

Figure 6.6. Population-averaged PDVHs of dose painting prescriptions for different contouring methods. Average PDVHs are shown for the original DPV (*black*), the DPV expanded by a single voxel layer (DPV_{plus}, *red*), and the DPV contracted by a single voxel layer (DPV_{minus}, *purple*).

histograms were 1.9 for FDG, 1.8 for FLT, and 1.0 for Cu-ATSM). The skewness in FDG and FLT SUV distributions resulted in higher B_{max} (redistribution method) or lower B_{mean} (max-dose method) values. Population averages of maximum tumor doses (D_{max}) are shown in Table 6.3 when different dose

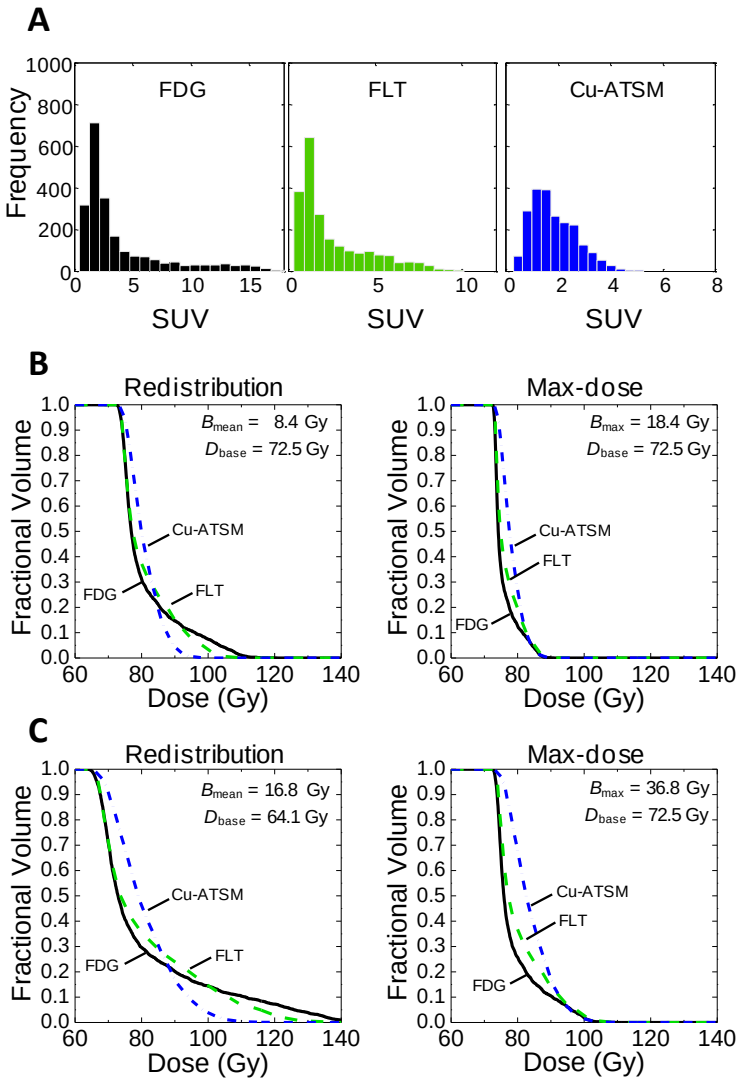

Figure 6.7. **A)** Histograms of voxel SUVs from an example patient's FDG, FLT, and Cu-ATSM PET images. **B)** PDVHs representing the patient's dose prescriptions using FDG (*black*), FLT (*green*), and Cu-ATSM (*blue*). For both prescription methods, the base dose to the tumor was constrained to be 72.5 Gy. For the redistribution method (*left*), the mean boost dose (B_{mean}) was constrained to be 8.4 Gy. For the max-dose method (*right*), the maximum boost to a tumor voxel (B_{max}) was constrained to be 18.4 Gy. **C)** PDVHs when B_{mean} was increased to 16.8 Gy for the redistribution method (*left*), and when B_{max} was increased to 36.8 Gy for the max-dose method (*right*).

constraints are used for the redistribution prescription method, and population averages of mean tumor doses (D_{mean}) are shown in Table 6.4 when different dose constraints are used for the max-dose prescription method.

For dosimetry analysis, images from resulting treatment plans and dosimetric analyses are shown for each of the 5 canine patients in Figure 6.8. Quantitative results are given in Table 6.5. Maximum voxel doses varied between patients, ranging from 6.9 Gy to 10.0 Gy per fraction, depending on Cu-ATSM uptake patterns. Decent conformity was obtained between optimized plans and voxel prescriptions: on average 89% of voxels received ±10% of their prescribed dose. Most of the discrepancies between prescriptions and optimized plans occurred around the boundaries of the GTV, where high dose values sometimes fell off in a step-like manner to the baseline dose of 4.2 Gy. Absolute dose measurements were within 3% of dose plans for all patients, with an average difference of -1.4%. Film dosimetry showed tomotherapy was capable of delivering the highly modulated plans: Gamma analysis (3%/3mm) showed that plans on average had only 0.1% of gamma values greater than 1.

Table 6.3. Population averages and standard deviations of maximum voxel doses when different clinically-relevant dose constraints are used for the redistribution prescription method.

Dose constraints (Gy)		Average D_{max} (Gy)		
D_{base}	B_{mean}	FDG prescriptions	FLT prescriptions	Cu-ATSM prescriptions
72.5	8.4	115 ± 12	117 ± 13	97 ± 6
64.1	16.8	150 ± 24	153 ± 27	113 ± 12

D_{base} = base dose; B_{mean} = mean boost; D_{max} = maximum voxel dose

Table 6.4. Population averages and standard deviations of mean tumor doses when different clinically-relevant dose constraints are used for the max-dose prescription method.

Dose constraints (Gy)		Average D_{mean} (Gy)		
D_{base}	B_{max}	FDG prescriptions	FLT prescriptions	Cu-ATSM prescriptions
72.5	18.4	76 ± 1	76 ± 1	79 ± 1
72.5	36.8	80 ± 2	80 ± 2	86 ± 3

D_{base} = base dose; B_{max} = maximum voxel boost; D_{mean} = mean tumor dose

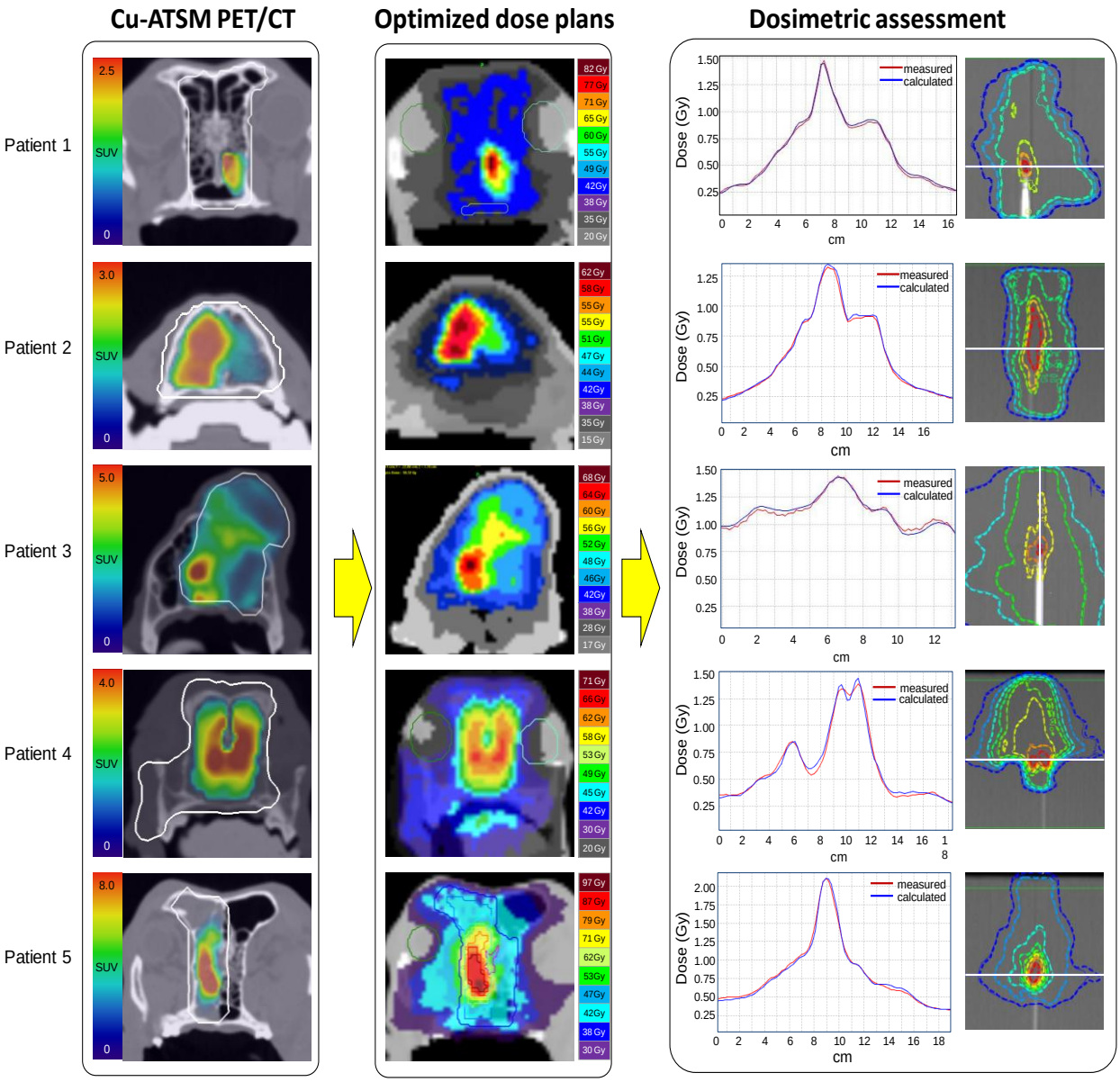

Figure 6.8. Five canine patients' Cu-ATSM dose painting plans were optimized in tomotherapy, and delivered to a phantom for dosimetric assessment.

Table 6.5. Absolute dose measurements and gamma analysis results from canine Cu-ATSM dose painting plans.

Patient	Max voxel dose per fraction	D_{meas} vs D_{calc}	γ >1 (3%/3mm)	γ >1 (2%/2mm)
1	6.9 Gy	-2.7%	0.2%	2.7%
2	7.5 Gy	-1.9%	0.01%	0.9%
3	10.0 Gy	-0.4%	0.1%	1.3%
4	8.7 Gy	-1.4%	0.05%	1.0%
5	7.3 Gy	-0.7%	0.1%	1.9%

6.4. Discussion

Dose painting for HN tumors is a promising area of research that has produced several clinical trials (*65, 73, 77, 97*), with several more currently underway. Yet there are still many uncertainties regarding how to best implement dose painting, particularly in defining the target volume and prescribing dose to said volume. In this study, we investigated how the uptake distributions of three different PET radiotracers would influence dose prescriptions for HN dose painting. We were able to make a direct comparison of how the different tracer distributions and prescription methods influenced overall dose prescription maps, and characterized the dosimetric trade-off between low- and high-uptake subvolumes.

Using the redistribution prescription method, we found that B_{max} could be very high for FDG and FLT plans, even for prescriptions with modest mean boosts. For every 1 Gy of B_{mean} added to a prescription, over 5 Gy would be added to the highest uptake voxels. We emphasize that the addition of 1 Gy to B_{mean} for a prescription with a fixed total dose is only possible by a parallel decrease in D_{base} by 1 Gy (see Figure 6.1). Hence, for a prescription with a fixed total dose, lowering the D_{base} by 1 Gy (ie, removing 1 Gy from the lowest-uptake subvolumes) would create a 1 Gy increase in B_{mean}, and therefore a 5 Gy increase in B_{max}. Consequently, only small sacrifices in dose need to be made to the low-uptake subvolumes to achieve large gains in dose for the highest uptake subvolumes. Cu-ATSM-based prescriptions had a lower degree of trade-off — a factor of 2.9 — due to the lower degree of skewness in Cu-ATSM SUV distributions.

Using the max-dose method, in which B_{max} was constrained, we found that FDG- and FLT-based prescriptions had average B_{mean} of about 20% of B_{max}. For Cu-ATSM plans, the B_{mean} was higher — about

37% of B_{max} — which was again due to the lower degree of skewness in Cu-ATSM SUV histograms. Several dose painting trials have previously used the max-dose methods for prescribing non-uniform dose (*65, 73*). We have demonstrated a consequence of the max-dose method: when B_{max} and D_{base} are constrained, B_{mean} will necessarily vary according to the unique distribution of voxel values in each patient's PET image. Therefore, different patients will have different mean tumor doses. We also showed that using the max-dose method, Cu-ATSM prescriptions would have a higher B_{mean} than FDG and FLT prescriptions.

We found that non-uniform boosts based on FDG and FLT had remarkably similar dose-volume relationships for both prescription methods. We previously showed in this patient population that tumor uptake of FDG and FLT (average $SUV_{max} \approx 14$) tended to be much higher than uptake of Cu-ATSM (average $SUV_{max} \approx 5$); however, FDG SUV_{max} and FLT SUV_{max} were not correlated across patients (*149*). Within tumors, however, we previously found that spatial correlations between tracer uptake patterns were slightly higher for FDG:FLT comparisons (R=0.53–0.85) than for FDG:Cu-ATSM (R=0.51–0.79) or for FLT:Cu-ATSM (R=0.21–0.80) comparisons (*149*). In this study, we found that PDVHs were, on average, nearly identical for FDG and FLT dose painting. This was due to FDG and FLT images having similar shapes to their SUV histograms (ie, similar relative distributions of SUV_i). The relative shape of a patient's SUV histogram ultimately determines the dose-volume relationships for their dose painting prescription for linear prescriptions functions, and both FDG and FLT SUV histograms were dominated by high frequencies of low SUVs (see Figure 6.7). Cu-ATSM SUV histograms, on the other hand, were less skewed, resulting in more homogeneous dose painting prescription maps.

For FDG- and FLT-based prescriptions, we observed that only very small volumes were prescribed very high boosts (see Figure 6.4). While high boosts to very small volumes might be more clinically preferable for certain tumor sites (eg, in avoiding large regions of necrosis), these prescriptions are also likely to be more challenging to plan and optimize. We also found that B_{max} values were sensitive to how the DPV was contoured for the redistribution method, with larger contours resulting in

substantially larger B_{max} values. This is due to larger contours incorporating a greater portion of low-uptake voxels, resulting in more dose being transferred to high-uptake voxels. Given the complexity of FDG and FLT redistribution plans and their sensitivities to contouring, it appears likely that future dose painting trials using the redistribution method will need to constrain B_{mean} while also capping B_{max}; this can be accomplished through iterative methods, as shown in Figure 6.2. As for Cu-ATSM dose painting, the feasibility of planning and delivering redistributed Cu-ATSM boosts has already been demonstrated (*27*).

There are a number of ways by which these results can be used to inform the design of prospective dose painting trials in HNSCC. First, this work describes some of the practical issues associated with choosing a particular dose prescription method. The redistribution method has a primary advantage over other methods: the mean tumor dose can be constrained to be the same for all patients. This allows for a trial design whereby a dose painting treatment arm can be directly compared with a uniform-dose treatment arm (ie, a control arm) (*47*). The results of this study can also aid in the selection of reasonable base (D_{base}) and boost (B_{mean}) prescription doses for a prospective clinical trial, as various values of B_{mean} can be multiplied by the x-axes' values of Figure 6.4 and Figure 6.5 to provide an estimate of the expected dose painting prescriptions. We have also demonstrated some disadvantages to using the redistribution method: the physical complexity of the dose prescriptions and its sensitivity to contouring. The max-dose method has the advantage that all patients' prescriptions would have roughly similar degrees of complexity, in addition to the simplicity and adaptability of the method (*51*, *65*). However, due to the variable SUV distributions among patient images, different patients' prescriptions would have different mean dose values, making it difficult to directly compare the efficacy of dose painting strategies against conventional plans. The results of this study provide an estimate of the expected mean and median dose boosts for any arbitrary B_{max} when using the max-dose prescription method.

A primary limitation of this study was the limited sample size. Despite the low number of patients, PDVHs were fairly consistent across patients, as interpatient variability was surprisingly low

(see Figure 6.5). An additional limitation is that we only evaluated two dose prescription methods, both of which involved linear prescription functions. As there are numerous potential methods for relating imaging values to dose (*75*), we chose to investigate two of the most practical and often-used methods, simplified so that they can be extended to a number of scenarios. Other nonlinear methods of prescription would have different results than those presented here. Finally, all results in this study were based on theoretical prescriptions, not on optimized plans, and therefore the influence of treatment modality, machine constraints, or dose optimization on the overall plans was not evaluated. The feasibility of dose painting optimization and its sensitivities to various delivery parameters has been published elsewhere (*27-28, 43, 75, 81*).

6.5. Conclusions

The goal of this work was to characterize how prescriptions maps are likely to be distributed for voxel-based dose painting in HN tumors, and to demonstrate the feasibility of accurately delivering voxel-based dose painting with tomotherapy. We showed that for dose painting prescriptions, especially those derived from FDG and FLT PET, a small reduction in dose to the low-uptake tumor subvolumes often results in large dosimetric gains to the highest-uptake subvolumes (for redistribution of a fixed mean tumor dose). This implies that if the high-uptake subvolumes are indeed the most radioresistant subvolumes, they can be targeted for very large dose boosts at the expense of relatively small dose reductions to the low-uptake subvolumes. This may prove to be a powerful method for controlling tumors that contain a small niche of highly resistant cells. Using canine data, we also demonstrated that Cu-ATSM dose painting plans can be accurately created and delivered using tomotherapy.

7. Summary and future directions

The overall goal of this dissertation was to characterize the properties of several potential imaging-based dose painting targets and determine how well they correlate with resistance to radiation therapy. This overall objective was split into three specific aims: the evaluation of FDG, FLT, and Cu-ATSM PET for their suitability as dose painting targets (Specific Aim 1), the assessment of quantitative imaging biomarkers as predictors of clinical outcome following radiation therapy (Specific Aim 2), and the demonstration of the feasibility of creating and delivering PET-based dose painting plans (Specific Aim 3).

This chapter summarizes the significant findings presented in this dissertation work, and discusses how they—in concert with other current dose painting research—impact the overall outlook for target definition in biologically-conformal radiation therapy. The limitations of this work are also examined. Finally, the future of biologically-conformal radiation therapy is discussed, with speculation on the future clinical research necessary to establish dose painting as a viable clinical treatment option.

7.1. Research summary

For Specific Aim 1, we aimed to characterize the properties of FDG, FLT, and Cu-ATSM PET that qualify them as good or poor candidates for targets in dose painting (Chapters 2-4). In Chapter 2 we evaluated the spatial stability of FLT and Cu-ATSM PET distributions during radiation therapy, and found that spatial distributions of FLT and Cu-ATSM uptake were surprisingly stable, especially for Cu-ATSM PET, indicating robust spatial targets for dose escalation. This was the first published study to evaluate the spatio-temporal stability of either proliferation maps or hypoxia maps during fractionated radiation therapy. In Chapter 3, we demonstrated that FDG, FLT, and Cu-ATSM PET uptake distributions were colocalized in canine carcinoma tumors, but were disparate in sarcoma tumors. This implies that certain tumor types or histologies may be more robust to how dose painting targets are defined, especially when there is uncertainty about which phenotype to target. In Chapter 4 we attempted

to identify the best spatial markers of resistance by correlating PET uptake patterns to spatial patterns of tumor recurrence through the use of voxel regression methods. This included the development of new image analysis methods for relating voxel intensity values at different time points. We discovered large interpatient variability in how well PET distributions predicted recurrence location, as roughly half of the patients showed strong correlations between PET imaging patterns and location of recurrence. All PET radiotracers performed about equally well (or equally poor, depending on the patient) in predicting location of recurrence.

Specific Aims 2 and 3 were addressed in Chapters 5 and 6, respectively. For Specific Aim 2, we evaluated numerous quantitative imaging biomarkers as predictors of resistance to radiation therapy in the CIRT trials. Using Cox PH regression, we found that neither FDG nor Cu-ATSM biomarkers were predictive of outcome, but rather FLT-based biomarkers were the most predictive of patient outcome, especially FLT biomarkers acquired during the course of radiation therapy. Finally, in Chapter 6, we characterized how non-uniform dose is likely to be distributed within human HN tumors. We found that for FDG and FLT redistributions-based dose painting, sacrificing 1 Gy to the lowest-uptake tumor subvolumes allows for approximately 5 Gy to be added to the highest-uptake subvolumes. We also demonstrated the accuracy with which Cu-ATSM-based dose painting plans can be delivered via tomotherapy.

This dissertation work makes a unique contribution to the field of dose painting by simultaneously evaluating the spatiotemporal properties of imaging surrogates for three potential dose painting targets: hypoxia (Cu-ATSM), glucose metabolism (FDG), and proliferation (FLT). Furthermore, we were able to evaluate how radiation-induced changes in Cu-ATSM and FLT uptake relate to treatment resistance. Due to the cost and logistics of acquiring multiple PET scans of cancer patients at multiple

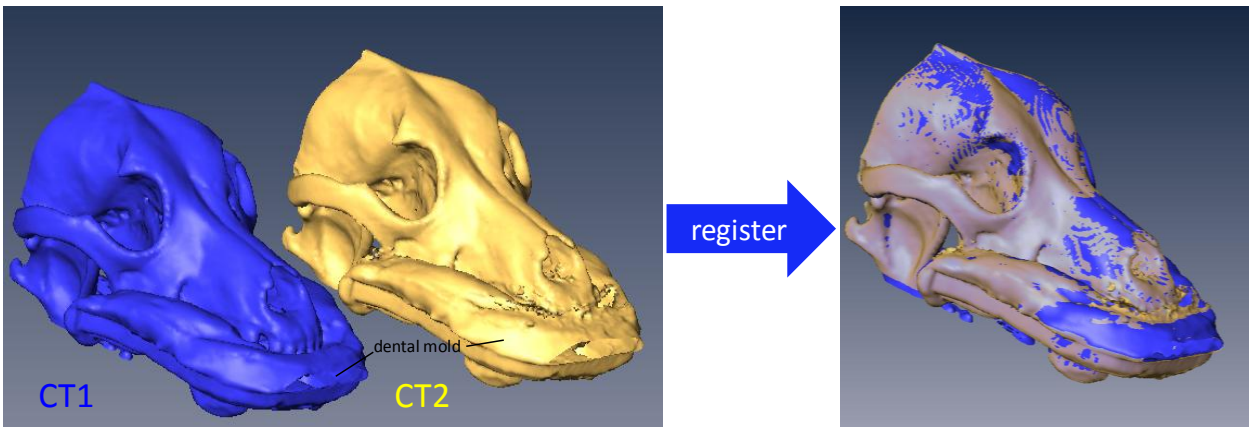

Figure 7.1. The bones surrounding the nasal cavities enabled very accurate image registration in canine sinonasal tumors.

time points, such exploratory studies are challenging and costly to perform in human patients, and are therefore uncommon (*149, 170-171, 207*). By utilizing canine tumors as models, we were able to benefit from several advantages of working with animal tumor models. The foremost advantage of using canine sinonasal tumors as research models was the precision with which we could acquire and cross-compare high quality PET images. In the CIRT trial, PET acquisitions were motionless due to anesthesia, patient positioning was precise and repeatable due to the bite block setup, and images were of high quality due to long PET acquisition times and high injected activities. Plus, the rigid bony nasal cavities surrounding the sinonasal tumors enabled extremely accurate image registration (see Figure 7.1), which is vital to performing accurate cross-comparisons of tracer spatial distributions (*149*). And while multi-tracer PET studies can and have been performed in murine models of cancer (*169, 172, 175-176, 208*), the spontaneous nature of canine tumors — often resulting from the same environmental carcinogens as human cancers — offers a more heterogeneous spectrum of biological resistances that are more representative of what would be observed in human tumors (*152, 209*).

In the following subsections, we describe what we have learned about target definition based on tumor hypoxia, glucose metabolism, and proliferation. These results are summarized in Table 7.1. We also discuss an important principle that was evident in the CIRT trial: that not all patients may be well-suited for dose painting. The limitations of our methods and results are then discussed.

7.1.1. Tumor hypoxia

When designing the CIRT trial, we originally hypothesized that Cu-ATSM PET would emerge as the best biomarker of radiation resistance, and therefore the best target for dose painting. Tumor hypoxia is the best established biomarker of radiation resistance in both humans and animals (*5*), and is therefore a logical candidate for a dose painting target (*35*). Furthermore, studies of Cu-ATSM PET in humans undergoing radiation therapy have been promising: the level of Cu-ATSM uptake has been found to be prognostic in tumors of the cervix (*132-133*), lung (*134*), rectum (*135*), and head-and-neck (*130*). We were also encouraged in the CIRT study by the observation that relative spatial distributions of Cu-ATSM were very stable after 3 fractions (12.6 or 15 Gy) of hypofractionated radiation therapy, suggesting that as a dose painting target, Cu-ATSM PET would be spatially robust (ie, it would not change locations over time). Also, we demonstrated the feasibility of accurately delivering Cu-ATSM-based dose painting plans with tomotherapy. However, according to our analysis of patient outcome in the CIRT trial, Cu-ATSM PET uptake patterns (both absolute uptake and relative changes in uptake during therapy) did not predict outcome following radiation therapy (see Chapter 5). Additionally, Cu-ATSM PET did not outperform FDG or FLT PET at predicting the location of tumor recurrence according to our voxel regression methods. In fact, in carcinoma tumors, Cu-ATSM uptake patterns were actually very similar to that of FDG and FLT uptake patterns. Therefore, based on the results presented in this dissertation work, Cu-ATSM PET did not stand out as a promising candidate target for dose painting.

There are several possible explanations as to why Cu-ATSM uptake did not predict resistance to radiation therapy in the CIRT trial. A primary limitation may have been the sample size, considering the heterogeneity of canine breeds, tumor sizes, and even tumor histologic subtypes included in the CIRT study. Another problem may have been the limitations of our method of analysis—namely, the uncertainties of the voxel-based regression methods and outcome analysis (this is discussed in greater detail in section 7.1.5). There are also several biochemical uncertainties that may have obscured the relationship between Cu-ATSM uptake and hypoxia. While many studies have demonstrated that Cu-

ATSM uptake is sensitive to induced hypoxia (*127, 157, 210*), several studies have found inconsistencies in the colocalization of Cu-ATSM uptake and tumor hypoxia in murine animals (*158, 211-214*). This lack of specificity for hypoxia appears to be more pronounced in certain histologic tumor types than others (*158, 214*). This may very well be the reason we saw different patterns of uptake in sarcoma tumors and in carcinoma tumors in the CIRT trial. An additional biochemical uncertainty is the stability of the Cu-ATSM complex *in vivo* after 3 hours. Studies have found that Cu can dissociate from the ATSM complex in animal blood, resulting in unbound radioactive Cu circulating through the tumor (*211*). Furthermore, once Cu-ATSM is internalized by a cancer cell and the Cu dissociates from the ATSM, the free Cu in the cytoplasm can still be expelled back into the extracellular space via Cu exporter proteins (*215*). The free circulating radioactive Cu can then be taken up by tumor cells in a manner independent of hypoxia, as has been demonstrated with PET imaging of ^{64}Cu salts (*216-217*). The relationship between Cu-ATSM and hypoxia may have been further obscured by the fact that serum albumin in canines has greater binding affinity for Cu-ATSM than in humans (*155*), and the fact that combination of anesthesia and 100% O_2 inhalation has been shown to influence Cu-ATSM uptake levels (*154*).

It is important to note that Cu-ATSM may yet be a viable biomarker of resistance regardless of the uncertainties surrounding its uptake mechanism. A mechanistic understanding of the relationship between dose response and the imaging intensity values is not as important as the existence of an empirical relationship between the target expression and resistance to radiation therapy (*47*). However, given the decades of accumulated evidence linking tumor hypoxia to radiation resistance, future dose painting trials using PET hypoxia tracers with more consistent correlations to tumor hypoxia (such as FMISO or FAZA (*218-219*)) may find a stronger associations between PET uptake patterns and patterns of radioresistance. These alternative hypoxia tracers, however, have been shown to suffer from low levels of uptake in tumors relative to surrounding tissues (*220*). Low signal, when combined with the statistical noise and biological uncertainties inherent to PET imaging, can translate into large relative uncertainties

in dose painting target definition and prescriptions (*144*). On the other hand, FMISO PET imaging has been shown to be spatially robust in a test-retest study (*145*), despite its low imaging values.

7.1.2. Tumor metabolism

Out of all the available imaging modalities, FDG PET has accumulated the most empirical evidence supporting its use as a dose painting target. This evidence comes from clinical trials demonstrating FDG PET uptake as a biomarker of resistance to radiation therapy (*221-223*), from studies in human tumors which correlated spatial patterns of tumor recurrence to FDG uptake patterns (*9, 14, 100, 109, 179-180*), and even from preclinical studies that demonstrated a dose-response relationship between FDG uptake and radiation therapy (*224*). These studies, however, were limited in that they did not concurrently investigate other imaging modalities or PET radiotracers as a means of comparison. Nonetheless, FDG PET has been used as a dose painting target in previous clinical trials, with several more trials underway (see Table 1.1).

In the CIRT trial, we did not observe evidence suggesting FDG PET as the best imaging modality for target definition in dose painting. According to survival analysis of the canine patients, FDG PET biomarkers did not predict resistance to radiation therapy. On the other hand, in Chapter 4 we found that pre-treatment FDG uptake distributions did have the highest performance in predicting the locations of recurrent tumor, according to linear voxel-regressions (ie, pre-treatment FDG had the highest average R^2 at predicting post-treatment FDG). The R^2 values for FDG, however, were not significantly different than those for Cu-ATSM or FLT, and when using logistic regression (which removed possible autocorrelation between pre- and post-FDG), all of the tracers performed about equally. It was also demonstrated in Chapter 3 that FDG had similar uptake distributions as FLT and Cu-ATSM in canine carcinoma tumors, and in canine sarcoma tumors, FDG had stronger spatial correlations to FLT and to Cu-ATSM than the correlations between FLT and Cu-ATSM. This suggests FDG uptake may have been influenced by both proliferation and hypoxia.

7.1.3. Tumor proliferation

FLT PET has been considered a promising imaging biomarker of early response to radiation therapy due to a rapid reduction in its uptake after the onset of radiation therapy (*26*), although its prognostic value has yet to be validated. In the CIRT trial, FLT PET biomarkers acquired during treatment, and FLT response from pre- to mid-treatment, were the most predictive biomarkers of resistance to radiation therapy in canine tumors, which suggests at FLT's potential as a dose painting target. The caveat, however, is that tumors with pronounced decreases in FLT uptake actually fared *worse* than tumors with no FLT response, or with increases in FLT uptake. This is contrast to results published by Hoeben *et al.*, who found large decreases in FLT uptake corresponded to better disease-free survival following chemoradiation for 33 HN cancer patients (*120*), although the addition of chemotherapy does not allow for a direct comparison to our study. Furthermore, in Chapter 4, we evaluated response maps of FLT PET (ratios of mid-treatment FLT images to pre-treatment FLT images) as predictors of recurrent tumor location, and found they were very poor predictors of recurrent tumor location ($R^2 \approx 0.05$). These spatial response maps, however, suffered from inflated ratios in regions of initially-low FLT uptake (ie, denominators were close to zero). We did include absolute changes in FLT uptake (ie, FLT_{mid}-FLT_{pre}) as part of the multivariate regression model in Chapter 4, but the R^2 were still very poor for many patients. FLT PET, therefore, appears to have some relationship to resistance mechanisms of tumors, although it remains uncertain if and how it could serve as an appropriate dose painting target. This work, as well as other FLT studies, warrants further evaluation of the relationship between longitudinal FLT PET imaging and resistance for cancer patients undergoing radiation therapy.

Table 7.1. Evidence for and against the use of FDG, FLT, and Cu-ATSM PET as dose painting targets.

Tracer	Origins of evidence	Empirical evidence *supporting* its use as a dose painting target	Empirical evidence *against* its use as a dose painting target
FDG	*Our work*	• Was a strong predictor of recurrent tumor location in *some* canine patients (Ch. 4) • According to linear voxel regressions, it had slightly higher correlations to post-treatment FDG than FLT or Cu-ATSM (*95*)(Ch. 4) • Using redistribution prescription methods with FDG, large dosimetric gains (5 to 1) can be achieved in high-uptake subvolumes by removing dose from low-uptake subvolumes (Ch. 6)	• Was not predictive of outcome in the CIRT study (Ch. 5) • Was a poor predictor of recurrent tumor location in *some* canine patients (Ch. 4)
	In literature	• Baseline FDG PET is often a good predictor of location of recurrence in human tumors (*14, 70, 100, 109, 179-180, 185*) • It is predictive of outcome following radiation therapy in certain human tumor types (*222-223, 225-227*)	• FDG uptake is influenced by inflammation and perfusion (*110*)
FLT	*Our work*	• Spatially-stable target early during radiation therapy (Ch. 2) • Mid-treatment FLT uptake and early FLT response were the best predictors of patient outcome in the CIRT study (Ch. 5) • FLT response precedes anatomical response (*26*)(Ch. 2) • Using redistribution prescription methods with FLT, large dosimetric gains (5 to 1) can be achieved in high-uptake subvolumes by removing dose from low-uptake subvolumes (Ch. 6) • Baseline and mid-treatment FLT were strong predictors of recurrent tumor location in *some* canine patients (Ch. 4)	• Early FLT response has predicted both favorable (*120*) and unfavorable outcome (Ch. 5) • FLT response maps were very poor predictors of recurrent tumor location in canine patients (Ch. 4) • Baseline and mid-treatment FLT were poor predictors of recurrent tumor location in *some* canine patients (Ch. 4)
	In literature	• FLT uptake is relatively specific for most tumors (*113*)	• Baseline proliferation rates do not predict response to radiation therapy (*116*)
Cu-ATSM	*Our work*	• Spatially-stable target early during radiation therapy (Ch. 2) • Baseline and mid-treatment Cu-ATSM were poor predictors of recurrent tumor location in *some* canine patients (Ch. 4)	• Was not predictive of outcome in the CIRT study (Ch. 5) • Baseline and mid-treatment Cu-ATSM were poor predictors of recurrent tumor location in *some* canine patients (Ch. 4)
	In literature	• Predictive of outcome following radiation therapy in several tumor types (*130-135*)	• Inconsistent correlation to hypoxia in different tumor types (*158, 211, 214*) • Uncertainties regarding *in vivo* molecular stability (*211*)

7.1.4. Candidate selection for dose painting

An important message has emerged from the results presented in this dissertation work that needs to be highlighted: a particular dose painting strategy is unlikely to be beneficial to all patients. In Chapter 4 we saw large variability among patients in how well PET imaging was able to predict the location of tumor recurrence. In Chapter 3 we saw sarcoma tumors and carcinoma tumors had very distinct imaging patterns. In future dose painting clinical trials, once an imaging target is selected, it will likely be necessary to screen patients whose tumors do not express that target, or in whom the imaging target is not expressed in a manner consistent with resistant to radiation therapy. For example, we have already discussed how Cu-ATSM may not correlate with hypoxia in certain tumor histologies (*211*). Matching patient-specific biology to the appropriate dose painting method will be necessary to improve clinical outcomes.

7.1.5. Limitations

There were several aspects of the CIRT study and its subsequent analysis that limited our ability to relate imaging patterns to resistance to radiation therapy—factors that should be considered in future studies. Unfortunately, due to logistical constraints, we were not able to validate FDG, FLT, and Cu-ATSM as reliable markers of glucose metabolism, proliferation, and hypoxia, respectively, in canine sinonasal tumors. PET radiotracers are imperfect surrogates of their respective biological targets, as tracer uptake can be influenced by perfusion, cellular density, and even target mutations. It is therefore desirable to evaluate the extent of their surrogacy, especially for an experimental tracer in an experimental host. For example, certain mutations in tumor cells can decouple thymidine influx from proliferative activity, thus confounding FLT uptake as a marker of proliferation (*228*). We have already discussed in the previous section the uncertainties surrounding Cu-ATSM's uptake mechanism. Furthermore, tracers can be metabolized by the host, making it difficult to decouple the PET signal originating from the tracer and the signal from the metabolites. We did perform metabolite analysis for FLT scans (we found canines do not metabolize FLT), but not for Cu-ATSM scans. Validating imaging methods as surrogates for biological

processes is not a simple process, and can involve the following: metabolite analysis of tracers in plasma, comparing tracer uptake patterns to perfusion patterns (eg, through perfusion imaging), comparing imaging patterns to an alternative imaging modality that measures the same function (if one exists), image-guided biopsies evaluated via histopathology staining, and correlating histopathology results against SUV and against parameters arising from kinetic analysis. Future studies should validate PET tracers in the host species, as understanding the biological mechanisms of the underlying imaging signal is vital to understanding the limitations, uncertainties, and robustness of the molecular imaging target (*22*).

A primary challenge in identifying imaging biomarkers of radiation resistance is the limited methods by which radioresistance can be measured *in vivo*. Traditionally, radioresistance is defined by the increased dose necessary to provide the same level of cell kill (for *in vitro* experiments) or tumor control (for *in vivo* experiments) as for control samples (*5*). However, spontaneous tumors demonstrate much greater biological complexity and inter-tumor variability than cell cultures or xenograft tumors, and resistance to radiation therapy can be influenced by a variety of additional biological properties, including immune response, perfusion, anatomical location, and so forth. Identifying consistent markers of radioresistance in a diverse population of tumors can be challenging, as evidenced by the relatively small number of molecular biomarkers that can consistently predict resistance to radiation (*192*). Typically, biomarkers of resistance are identified by outcome analysis of local control rates or overall survival in patients treated with radiation therapy. But this only identifies biological targets that are in some way related to or influence clinical outcome, which may not necessarily indicate the existence of a dose-response relationship. For example, one may identify an imaging biomarker that predicts worse overall survival in patients undergoing radiation therapy, but that biomarker may actually be an indication of host immune response rather than inherent cellular radioresistance, and may not actually indicate whether or not that tumor would have responded better to a higher dose prescription. In the CIRT trial, we identified change in FLT uptake as a prognostic biomarkers of progression-free survival (Chapter 5), but we did not

observe FLT uptake patterns to be a consistent spatial predictor of recurrent tumor location (Chapter 4). Response maps of FLT were even worse predictors of recurrent tumor location. These are the limitations of outcome analysis, and highlight the importance of understanding the underlying mechanistic relationship between an imaging biomarker and its biological target.

An even greater challenge is acquiring spatially-resolved measurements of radiosensitivity in tumors. Prognostic biomarkers of overall resistance to radiation therapy—measured according to clinical outcome—may or may not be adequate biomarkers for measuring spatially-varying radioresistance (tumor volume would be an example biomarker that cannot be defined on the voxel level). It is unclear how to best evaluate spatially-varying radiosensitivity. The most commonly-used method is to compare the location of residual or recurrent tumor to baseline imaging patterns—such as we performed in Chapter 4—either through overlap analysis or through voxel regressions/correlations (*14, 70, 95*). These methods work under the assumption that when the PET or CT signal in a tumor's voxel disappears following treatment, that tumor subvolume has been controlled. It is unclear how frequently this assumption is valid. For example, it does not allow for cases in which viable tumor cells remain in a voxel location, but not enough to produce a detectible imaging signal. Nor does it allow for cases where a fraction of the tumor cells of multiple neighboring voxels are controlled, and the remaining tumor cells conjoin into a smaller number of voxels. While deformable registration methods can account for tumor morphological changes over time, these methods are 'mass-preserving', meaning they do not account for the fraction of the tumor that is killed and cleared away from the tumor. It is also uncertain how to best define residual or recurrent tumor location after therapy. Using CT imaging, necrotic tumor can be mistaken as viable tumor, and using FDG PET, inflammation or non-specific uptake can appear as recurrent tumor. There are also statistical limitations when performing voxel-based statistical analysis. As various tumor properties (eg, tumor shape, variations in cell density, perfusions levels) can similarly influence all imaging methods, there is often high multicollinearity among voxel-based covariates, which can confound statistical analysis. Also, treating individual voxels as independent samples for hypothesis testing is

inaccurate and can lead to misleading results. Methods of accounting for autocorrelations among neighboring voxels are necessary, yet underdeveloped in image analysis for oncology.

We were limited in the number of imaging methods we could investigate in the CIRT trial. It is possible that other imaging methods could be better markers of radioresistance—and be more suitable as a dose painting target—than the imaging methods we investigated. Other candidates for biological targets include apoptosis (*229*), epidermal growth factor receptor expression (*230*), hypoxia inducible factor expression (*231*), amino acid metabolism (*47*), cancer stem cell density (*232*), and alternative imaging surrogates of hypoxia such as FMISO or FAZA PET (*145, 218*). A challenge to finding an imaging surrogate of resistance to radiation therapy, however, is that only a small niche of remaining tumor cells may be necessary to repopulate a treated tumor. If the resistant cells are small in number, no matter how they are targeted and labeled for imaging, the imaging signal may be too low for detection. This is a primary challenge in the development of tracers for radiation resistance.

7.2. Dose painting clinical trial design

The future of dose painting research will primarily involve two objectives: validating existing dose painting imaging targets through randomized clinical trials, and discovering new imaging agents for target definition through preclinical research and exploratory clinical studies. In the end, dose painting can only be validated as an effective therapeutic option after extensive clinical trials randomizing patients between dose painting and standard of care IMRT. However, intelligently-designed exploratory trials can help guide the design of subsequent trials, increasing the probability of the development of a successful dose painting strategy. In this section, we recommend study components that should be considered or included in future dose painting clinical trials.

7.2.1. Imaging target selection

As has already been discussed in this dissertation, there are many imaging modalities from which to select an imaging target for dose painting, none of which have been actually validated as suitable

targets. The selection of the imaging target will probably have the largest impact on whether or not the dose painting method will be successful. It is therefore necessary that before selecting an imaging modality for target definition, both preclinical experiments and exploratory trials should demonstrate a link between the imaging signal and resistance to radiation therapy. It is also important that different dose painting trials test a variety of promising imaging targets, so that different methods can be cross compared and the best method eventually identified. It is also not unreasonable to use a combination of imaging methods to define a target. For example, combining the sensitivity of FDG PET imaging with the specificity of FLT PET imaging may allow for more accurate tumor delineation methods (*233-235*).

A further consideration should be the time point at which the imaging target is defined. Studies have demonstrated that target definition during therapy, or adapting target volumes during therapy, is feasible (*57, 65*). We found that mid-treatment FLT images were more predictive of resistance than baseline FLT images. The imaging time points will certainly depend on the imaging target that is used, but should not be restricted to being defined at baseline only.

Future dose painting studies may also want to consider the method of regional dose painting. In regional dose painting, the tumor volume is partitioned into regions or clusters based on biological similarities, and then each region receives a unique dose prescription depending on its expected state of resistance. This would represent a compromise between voxel-based dose painting and uniform boosting. Indirect evidence for this is illustrated in Figure 4.2, which shows during-treatment CT imaging of canine tumors treated with IMRT. Images revealed that certain tumor subregions experienced prompt anatomical response, whereas other subregions did not. The patterns of anatomical response were unique for each tumor, but response was typically on a regional scale rather than on a voxel or whole-tumor level. While it is unclear how to best partition tumors into subregions with similar biological and resistance profiles, there is promise in combining molecular imaging with supervised or unsupervised classification algorithms (*236*). Methods for indentifying regional-based biological targets and performing regional dose painting have yet to be explored.

7.2.2. Patient selection

Choosing the patient populations most likely to benefit from dose painting is a challenging but necessary task. First, a tumor site needs to be selected. The top candidate sites for dose painting are in the HN, brain, and lung (*41, 47, 237*). Tumors of the HN and brain benefit from established immobilization techniques, which would reduce the imaging and treatment uncertainties associated with motion and setup error (*238*). A disadvantage for dose painting in HN tumors, however, is that current uniform dose prescriptions already perform very well for many patients and histologies, with local control rates above 90% for early stage tumors (*239*). Dose painting in HN tumors, therefore, is unlikely to result in a substantial improvements over standard-of-care therapies, as has already been evidenced from recent dose painting trials (*59, 67*). Dose painting in the brain is mainly limited by the fact that some radiopharmaceuticals do not perform well in the brain, either due to the blood-brain barrier (*240*) or high background metabolic activity in healthy brain (*241-242*). Lung cancer, on the other hand, is the leading cause of cancer death among men and women (*243*), with current radiation therapy protocols resulting in poor local control rates (*191*). The primary obstacle in lung dose painting is motion-induced geometric uncertainties, which results in blurring of the image and dose distribution, although these can be somewhat mitigated using 4-dimensional imaging and motion management techniques (*244*).

Beyond tumor site, further patient selection requirements would include tumor stage, histologic tumor type, and tumor volume. We demonstrated in Chapter 3—as has been demonstrated by other studies (*170-171*)—that different tumor histologies can have dramatically different imaging patterns. Some histologies may be better suited than others for dose painting with a particular imaging target, and preliminary experiments are necessary to establish the imaging method as a marker of radiation resistance in the histology of interest. As for tumor stage/volume, small and large tumors should not necessarily be grouped together. Dose painting for small spherical lesions or nodules, in which biological heterogeneity in minimal (especially on the spatial scale of molecular imaging), is likely to have different outcome that dose painting for large advanced tumors, in which dose can be shaped to match the intratumor

heterogeneities. Inclusion criteria for clinical trials should either include a minimum tumor volume, or patients should be stratified according to tumor volume.

7.2.3. Dose prescription method

The method of dose prescription has already been discussed in detail in Chapter 6. Currently, linear prescription functions seem to be the rational choice for experimental dose painting trials, at least until evidence emerges suggesting the superiority of non-linear prescription methods. The optimal prescription function is likely to be very complex, involving numerous biological and biochemical variables that often go unmeasured. For example, using electrochemical modeling, Bowen *et al.* estimated that the relationship between Cu-ATSM and hypoxia was very sensitive to the conditions of the microenvironment, particularly the acidity. For dose painting methods that use oxygen enhancement ratios, these biochemical uncertainties would then translate into relatively large dosimetric uncertainties (*245*). Therefore, first-order approximations of prescription functions (ie, linear) are a reasonable starting point.

Perhaps the more pertinent questions is: by how much should the dose be modulated inside the target volume? We showed in Chapter 6 that for FDG and FLT-based prescriptions in HN tumors, removing 1 Gy from the lowest-uptake tumor subvolumes allows for about 5 Gy to be added to the highest-uptake tumor subvolumes, while keeping the mean tumor dose fixed. At some point, however, lowering the dose to the low-uptake voxels will prove detrimental to the overall tumor control probability. This threshold of modulation will clearly depend on the sensitivity and specificity of imaging method, the tumor site, and even the patient biology. It is plausible that lung tumors (with their low local control rates) will require a greater degree of dose modulation than HN tumors. Based on measurements of oxygen enhancement ratios, hypoxic cells may require up to 3 times the dose for equivalent cell kill (*5*), suggesting that considerably large degrees of dose modulations may be required. An understanding of the relationship between the imaging agent and its biological target, and the relationship between the biological target and radioresistance will allow for modeling studies to approximate the optimal degree of

dose modulation. In the meantime, systematically increasing the degree of dose modulation across different studies may help identify a "peak" at which local control rates are maximized.

7.2.4. Additional assays

An important component to future dose painting trials will be any additional imaging and biological information that can be acquired from tumors, so as to better guide future dose painting studies. In traditional radiation therapy, patients were categorized according to tumor type and stage, and given population-based dose prescriptions based on clinical experience. Dose painting aims to incorporate patient-specific biology in the form of the imaging target, but this need not be the only biological assay incorporated into treatment planning. For example, a particular tumor mutation may cause the expression of the imaging target to occur in a manner inconsistent with radioresistance, and that mutation could be used as a biomarker to screen or stratify patients in future trials. Examples of other variables with potential discriminatory value include degree of tumor inflammation, prevalence of hypoxia, human papillomavirus status, biochemical stability of the radiotracer *in vivo*, location of the tumor relative to surrounding sensitive tissue, rapidity of anatomical response, and so forth.

Additional functional imaging of normal tissue might also prove useful in not only stratifying patients, but in guiding dose distributions in healthy tissue. For example, in lung cancer, it has been proposed that lung perfusion imaging may help identify non-functioning regions of lung that could receive a larger portion of the normal tissue dose than healthy functioning lung (*246-247*). Likewise, FDG PET in lung may identify regions of inflammation that are more susceptible to radiation damage — regions that could be conformally avoided (*248*). Overall, the addition of informative biological assays to dose painting trials can help guide future studies, and lead to more effective, personalized radiation therapy.

7.2.5. Endpoints and analysis

Biologically- and clinically- relevant primary and secondary endpoints in trials will allow for the proper evaluation of effectiveness of different dose painting methods. For randomized controlled trials, the gold standard for evaluation of treatment efficacy is the evidence of statistically significant improvement in overall survival (OS) and/or quality-of-life (*249*). However, using OS as a primary endpoint requires long follow-up times and a larger sample size, and therefore surrogate endpoints have found increasing use, such as progression-free survival (PFS) and disease-free survival, albeit controversially (*249*). For dose painting, in addition to OS and PFS, secondary endpoints of local control (or loco-regional control) and normal tissue toxicity rates will be particularly important to monitor. Dose painting has the potential to both reduce *and* increase normal tissue toxicities, depending on the location of the high-uptake tumor subvolumes relative to surrounding tissues. If, for example, a particular dose painting strategy reduces normal tissue toxicity, but not local control rates, it would follow that the integral dose for that dose painting strategy could be raised. Or, if dose painting dramatically improves local control but also worsens normal tissue toxicities, lower dose prescriptions might be needed. Informative secondary endpoints can help tailor future dose prescriptions to maximize the therapeutic ratio.

In addition to conventional clinical trial endpoints, imaging endpoints may prove particularly valuable in dose painting (*250*). Dose painting is a form of targeted therapy, as specific biological targets are identified and then therapeutically targeted. Evaluating the biological target expression, or other related biological targets, either during therapy or after therapy may help identify which patients are responding or will respond to the treatment. Furthermore, it can help elucidate how the therapy is altering the pathophysiology of the tumor, and how that alteration relates to clinical outcome. The challenge, however, will be matching the appropriate imaging biomarker to the dose painting method. Ultimately, identifying relevant imaging biomarkers of response to dose painting may eventually lead to identification of imaging-based surrogate endpoints.

7.3. Conclusion

This dissertation work represents an important step in the characterization of the spatio-temporal properties of several molecular imaging agents commonly considered as candidates for dose painting targets, and in the development of methods for estimating the efficacy of different imaging targets. Current methods of population-based uniform-dose prescriptions will only be necessary until functional imaging methods allow for accurate measurements of non-uniform patterns of radioresistance. Once adequate methods for imaging resistance are available, dose painting will undoubtedly become the preferred method of radiation therapy for select tumor sites. We are currently at the threshold of an era of personalized medicine in oncology, wherein treatments are tailored to match patient-specific biology for optimal patient outcome. Dose painting will become a valuable tool in the arsenal of personalized therapies available to physicians and patients.

References

1. Heppner GH. Tumor heterogeneity. *Cancer Res.* 1984;44(6):2259-2265.

2. Hanahan D, Weinberg RA. Hallmarks of cancer: the next generation. *Cell.* Mar 4 2011;144(5):646-674.

3. Gerlinger M, Rowan AJ, Horswell S, et al. Intratumor heterogeneity and branched evolution revealed by multiregion sequencing. *N Engl J Med.* Mar 8 2012;366(10):883-892.

4. Navin N, Krasnitz A, Rodgers L, et al. Inferring tumor progression from genomic heterogeneity. *Genome Res.* 2010;20(1):68-80.

5. Hall EJ, Giaccia AJ. *Radioboiology for the Radiologist*. 6 ed. Philadeplphia, PA: Lippincott Williams & Wilkins; 2006.

6. Moulder JE, Rockwell S. Hypoxic fractions of solid tumors: experimental techniques, methods of analysis, and a survey of existing data. *Int J Radiat Oncol Biol Phys.* 1984;10(5):695-712.

7. Nordsmark M, Bentzen SM, Rudat V, et al. Prognostic value of tumor oxygenation in 397 head and neck tumors after primary radiation therapy. An international multi-center study. *Radiother Oncol.* 2005;77(1):18-24.

8. Webb S, Nahum AE. A model for calculating tumour control probability in radiotherapy including the effects of inhomogeneous distributions of dose and clonogenic cell density. *Phys Med Biol.* Jun 1993;38(6):653-666.

9. van den Bogaard J, Janssen MHM, Janssens G, et al. Residual metabolic tumor activity after chemo-radiotherapy is mainly located in initially high FDG uptake areas in rectal cancer. *Radiother Oncol.* 2011;99(2):137-141.

10. Hurkmans CW, Cuijpers JP, Lagerwaard FJ, et al. Recommendations for implementing stereotactic radiotherapy in peripheral stage IA non-small cell lung cancer: report from the Quality Assurance Working Party of the randomised phase III ROSEL study. *Radiat Oncol.* 2009;4:1.

11. Martel MK, Ten Haken RK, Hazuka MB, et al. Estimation of tumor control probability model parameters from 3-D dose distributions of non-small cell lung cancer patients. *Lung Cancer.* Apr 1999;24(1):31-37.

12. Bradley J. A review of radiation dose escalation trials for non-small cell lung cancer within the Radiation Therapy Oncology Group. *Semin Oncol.* Apr 2005;32(2 Suppl 3):S111-113.

13. Bradley JD, Paulus R, Komaki R, et al. A randomized phase III comparison of standard-dose (60 Gy) versus high-dose (74 Gy) conformal chemoradiotherapy with or without cetuximab for stage III non-small cell lung cancer: Results on radiation dose in RTOG 0617. *ASCO Meeting Abstracts.* June 17, 2013 2013;31(15_suppl):7501.

14. Aerts HJWL, van Baardwijk AAW, Petit SF, et al. Identification of residual metabolic-active areas within individual NSCLC tumours using a pre-radiotherapy (18)Fluorodeoxyglucose-PET-CT scan. *Radiother Oncol.* 2009;91(3):386-392.

15. Chao KS, Ozyigit G, Tran BN, Cengiz M, Dempsey JF, Low DA. Patterns of failure in patients receiving definitive and postoperative IMRT for head-and-neck cancer. *Int J Radiat Oncol Biol Phys.* Feb 1 2003;55(2):312-321.

16. Pucar D, Hricak H, Shukla-Dave A, et al. Clinically significant prostate cancer local recurrence after radiation therapy occurs at the site of primary tumor: magnetic resonance imaging and step-section pathology evidence. *Int J Radiat Oncol Biol Phys.* Sep 1 2007;69(1):62-69.

17. Arrayeh E, Westphalen AC, Kurhanewicz J, et al. Does local recurrence of prostate cancer after radiation therapy occur at the site of primary tumor? Results of a longitudinal MRI and MRSI study. *Int J Radiat Oncol Biol Phys.* 2012;82(5):e787-793.

18. Ling CC, Humm J, Larson S, et al. Towards multidimensional radiotherapy (MD-CRT): biological imaging and biological conformality. *Int J Radiat Oncol Biol Phys.* 2000;47(3):551-560.

19. Brahme A, Agren AK. Optimal dose distribution for eradication of heterogeneous tumours. *Acta Oncol.* 1987;26(5):377-385.

20. Brahme A. Dosimetric precision requirements in radiation therapy. *Acta radiologica Oncology.* 1984;23(5):379-391.

21. Webb S, Evans PM, Swindell W, Deasy JO. A proof that uniform dose gives the greatest TCP for fixed integral dose in the planning target volume. *Phys Med Biol.* 1994;39(11):2091-2098.

22. Bentzen SM. Theragnostic imaging for radiation oncology: dose-painting by numbers. *Lancet Oncol.* 2005;6(2):112-117.

23. Yang Y, Xing L. Towards biologically conformal radiation therapy (BCRT): selective IMRT dose escalation under the guidance of spatial biology distribution. *Med Phys.* 2005;32(6):1473-1484.

24. Popple RA, Ove R, Shen S. Tumor control probability for selective boosting of hypoxic subvolumes, including the effect of reoxygenation. *Int J Radiat Oncol Biol Phys.* Nov 1 2002;54(3):921-927.

25. Solberg TD, Agazaryan N, Goss BW, Dahlbom M, Lee SP. A feasibility study of 18F-fluorodeoxyglucose positron emission tomography targeting and simultaneous integrated boost for intensity-modulated radiosurgery and radiotherapy. *J Neurosurg.* Nov 2004;101 Suppl 3:381-389.

26. Troost EG, Bussink J, Hoffmann AL, Boerman OC, Oyen WJ, Kaanders JH. 18F-FLT PET/CT for early response monitoring and dose escalation in oropharyngeal tumors. *J Nucl Med.* Jun 2010;51(6):866-874.

27. Deveau MA, Bowen SR, Westerly DC, Jeraj R. Feasibility and sensitivity study of helical tomotherapy for dose painting plans. *Acta Oncol.* 2010;49(7):991-996.

28. Thorwarth D, Eschmann S-M, Paulsen F, Alber M. Hypoxia dose painting by numbers: a planning study. *Int J Radiat Oncol Biol Phys.* 2007;68(1):291-300.

29. Rickhey M, Koelbl O, Eilles C, Bogner L. A biologically adapted dose-escalation approach, demonstrated for 18F-FET-PET in brain tumors. *Strahlenther Onkol.* Oct 2008;184(10):536-542.

30. Niyazi M, Bartenstein P, Belka C, Ganswindt U. Choline PET based dose-painting in prostate cancer--modelling of dose effects. *Radiat Oncol.* 2010;5:23.

31. Malinen E, Sovik A, Hristov D, Bruland OS, Olsen DR. Adapting radiotherapy to hypoxic tumours. *Phys Med Biol.* Oct 7 2006;51(19):4903-4921.

32. Bender ET. Using spatial information about recurrence risk for robust optimization of dose-painting prescription functions. *Med Phys.* 2012;39(5):2713-2720.

33. Stavreva NA, Stavrev PV, Round WH. A mathematical approach to optimizing the radiation dose distribution in heterogeneous tumours. *Acta Oncol.* 1996;35(6):727-732.

34. Galvin JM, De Neve W. Intensity modulating and other radiation therapy devices for dose painting. *J Clin Oncol.* Mar 10 2007;25(8):924-930.

35. Chao KS, Bosch WR, Mutic S, et al. A novel approach to overcome hypoxic tumor resistance: Cu-ATSM-guided intensity-modulated radiation therapy. *Int J Radiat Oncol Biol Phys.* 2001;49(4):1171-1182.

36. Bentzen SM. Dose painting and theragnostic imaging: towards the prescription, planning and delivery of biologically targeted dose distributions in external beam radiation oncology. *Cancer Treat Res.* 2008;139:41-62.

37. Lawrence YR, Werner-Wasik M, Dicker AP. Biologically conformal treatment: biomarkers and functional imaging in radiation oncology. *Future Oncol.* Oct 2008;4(5):689-704.

38. Alber M, Paulsen F, Eschmann SM, Machulla HJ. On biologically conformal boost dose optimization. *Phys Med Biol.* Jan 21 2003;48(2):N31-35.

39. Sovik A, Malinen E, Olsen DR. Strategies for biologic image-guided dose escalation: a review. *Int J Radiat Oncol Biol Phys.* Mar 1 2009;73(3):650-658.

40. Brahme A. Biologically optimized 3-dimensional in vivo predictive assay-based radiation therapy using positron emission tomography-computerized tomography imaging. *Acta Oncol.* 2003;42(2):123-136.

41. Lambin P, Petit SF, Aerts HJ, et al. The ESTRO Breur Lecture 2009. From population to voxel-based radiotherapy: exploiting intra-tumour and intra-organ heterogeneity for advanced treatment of non-small cell lung cancer. *Radiother Oncol.* Aug 2010;96(2):145-152.

42. Thorwarth D, Alber M. Implementation of hypoxia imaging into treatment planning and delivery. *Radiother Oncol.* 2010;97(2):172-175.

43. Das SK, Miften MM, Zhou S, et al. Feasibility of optimizing the dose distribution in lung tumors using fluorine-18-fluorodeoxyglucose positron emission tomography and single photon emission computed tomography guided dose prescriptions. *Med Phys.* 2004;31(6):1452-1461.

44. Thorwarth D, Geets X, Paiusco M. Physical radiotherapy treatment planning based on functional PET/CT data. *Radiother Oncol.* 2010;96(3):317-324.

45. Supiot S, Lisbona A, Paris F, Azria D, Fenoglietto P. ["Dose-painting": myth or reality?]. *Cancer Radiother.* Oct 2010;14(6-7):554-562.

46. Schwartz DL, Ford EC, Rajendran J, et al. FDG-PET/CT-guided intensity modulated head and neck radiotherapy: a pilot investigation. *Head Neck.* 2005;27(6):478-487.

47. Bentzen SM, Gregoire V. Molecular imaging-based dose painting: a novel paradigm for radiation therapy prescription. *Semin Radiat Oncol.* 2011;21(2):101-110.

48. van der Heide UA, Houweling AC, Groenendaal G, Beets-Tan RG, Lambin P. Functional MRI for radiotherapy dose painting. *Magn Reson Imaging.* Nov 2012;30(9):1216-1223.

49. Vanderstraeten B, De Gersem W, Duthoy W, De Neve W, Thierens H. Implementation of biologically conformal radiation therapy (BCRT) in an algorithmic segmentation-based inverse planning approach. *Phys Med Biol.* 2006;51(16):N277-286.

50. Gregoire V, Jeraj R, Lee JA, O'Sullivan B. Radiotherapy for head and neck tumours in 2012 and beyond: conformal, tailored, and adaptive? *Lancet Oncol.* Jul 2012;13(7):e292-300.

51. Vanderstraeten B, Duthoy W, De Gersem W, De Neve W, Thierens H. [18F]fluoro-deoxy-glucose positron emission tomography ([18F]FDG-PET) voxel intensity-based intensity-modulated radiation therapy (IMRT) for head and neck cancer. *Radiother Oncol.* 2006;79(3):249-258.

52. Hoeben BA, Bussink J, Troost EG, Oyen WJ, Kaanders JH. Molecular PET imaging for biology-guided adaptive radiotherapy of head and neck cancer. *Acta Oncol.* Oct 2013;52(7):1257-1271.

53. Sovik A, Malinen E, Bruland OS, Bentzen SM, Olsen DR. Optimization of tumour control probability in hypoxic tumours by radiation dose redistribution: a modelling study. *Phys Med Biol.* Jan 21 2007;52(2):499-513.

54. Geets X, Gregoire V, Lee JA. Implementation of hypoxia PET imaging in radiation therapy planning. *Q J Nucl Med Mol Imaging.* Sep 2013;57(3):271-282.

55. Sovik A, Malinen E, Skogmo HK, Bentzen SM, Bruland OS, Olsen DR. Radiotherapy adapted to spatial and temporal variability in tumor hypoxia. *Int J Radiat Oncol Biol Phys.* 2007;68(5):1496-1504.

56. Chen GP, Ahunbay E, Schultz C, Li XA. Development of an inverse optimization package to plan nonuniform dose distributions based on spatially inhomogeneous radiosensitivity extracted from biological images. *Med Phys.* Apr 2007;34(4):1198-1205.

57. Douglas JG, Stelzer KJ, Mankoff DA, et al. [F-18]-fluorodeoxyglucose positron emission tomography for targeting radiation dose escalation for patients with glioblastoma multiforme: clinical outcomes and patterns of failure. *Int J Radiat Oncol Biol Phys.* Mar 1 2006;64(3):886-891.

58. Thorwarth D, Soukup M, Alber M. Dose painting with IMPT, helical tomotherapy and IMXT: a dosimetric comparison. *Radiother Oncol.* 2008;86(1):30-34.

59. Madani I, Duthoy W, Derie C, et al. Positron emission tomography-guided, focal-dose escalation using intensity-modulated radiotherapy for head and neck cancer. *Int J Radiat Oncol Biol Phys.* 2007;68(1):126-135.

60. Gillham C, Zips D, Ponisch F, et al. Additional PET/CT in week 5-6 of radiotherapy for patients with stage III non-small cell lung cancer as a means of dose escalation planning? *Radiother Oncol.* Sep 2008;88(3):335-341.

61. Miwa K, Matsuo M, Shinoda J, et al. Simultaneous integrated boost technique by helical tomotherapy for the treatment of glioblastoma multiforme with 11C-methionine PET: report of three cases. *Journal of neuro-oncology.* 2008;87(3):333-339.

62. Lee NY, Mechalakos JG, Nehmeh S, et al. Fluorine-18-labeled fluoromisonidazole positron emission and computed tomography-guided intensity-modulated radiotherapy for head and neck cancer: a feasibility study. *Int J Radiat Oncol Biol Phys.* Jan 1 2008;70(1):2-13.

63. Pinkawa M, Holy R, Piroth MD, et al. Intensity-modulated radiotherapy for prostate cancer implementing molecular imaging with 18F-choline PET-CT to define a simultaneous integrated boost. *Strahlenther Onkol.* 2010;186(11):600-606.

64. Lin Z, Mechalakos J, Nehmeh S, et al. The influence of changes in tumor hypoxia on dose-painting treatment plans based on 18F-FMISO positron emission tomography. *Int J Radiat Oncol Biol Phys.* Mar 15 2008;70(4):1219-1228.

65. Duprez F, De Neve W, De Gersem W, Coghe M, Madani I. Adaptive Dose Painting by Numbers for Head-and-Neck Cancer. *Int J Radiat Oncol Biol Phys.* 2011;80(4):1045-1055.

66. Kim Y, Tome WA. On Voxel based Iso-Tumor Control Probabilty and Iso-Complication Maps for Selective Boosting and Selective Avoidance Intensity Modulated Radiotherapy. *Imaging Decis (Berl).* Spring 2008;12(1):42-50.

67. Madani I, Duprez F, Boterberg T, et al. Maximum tolerated dose in a phase I trial on adaptive dose painting by numbers for head and neck cancer. *Radiother Oncol.* Dec 2011;101(3):351-355.

68. Flynn RT, Bowen SR, Bentzen SM, Rockwell Mackie T, Jeraj R. Intensity-modulated x-ray (IMXT) versus proton (IMPT) therapy for theragnostic hypoxia-based dose painting. *Phys Med Biol.* Aug 7 2008;53(15):4153-4167.

69. Fodor A, Fiorino C, Dell'Oca I, et al. PET-guided dose escalation tomotherapy in malignant pleural mesothelioma. *Strahlenther Onkol.* Nov 2011;187(11):736-743.

70. Petit SF, Aerts HJWL, van Loon JGM, et al. Metabolic control probability in tumour subvolumes or how to guide tumour dose redistribution in non-small cell lung cancer (NSCLC): an exploratory clinical study. *Radiother Oncol.* 2009;91(3):393-398.

71. Piroth MD, Pinkawa M, Holy R, et al. Integrated boost IMRT with FET-PET-adapted local dose escalation in glioblastomas. Results of a prospective phase II study. *Strahlenther Onkol.* Apr 2012;188(4):334-339.

72. Petit SF, Dekker ALAJ, Seigneuric R, et al. Intra-voxel heterogeneity influences the dose prescription for dose-painting with radiotherapy: a modelling study. *Phys Med Biol.* 2009;54(7):2179-2196.

73. Berwouts D, Olteanu LA, Duprez F, et al. Three-phase adaptive dose-painting-by-numbers for head-and-neck cancer: initial results of the phase I clinical trial. *Radiother Oncol.* Jun 2013;107(3):310-316.

74. Feng M, Kong F-M, Gross M, Fernando S, Hayman JA, Ten Haken RK. Using fluorodeoxyglucose positron emission tomography to assess tumor volume during radiotherapy for non-small-cell lung cancer and its potential impact on adaptive dose escalation and normal tissue sparing. *Int J Radiat Oncol Biol Phys.* 2009;73(4):1228-1234.

75. Bowen SR, Flynn RT, Bentzen SM, Jeraj R. On the sensitivity of IMRT dose optimization to the mathematical form of a biological imaging-based prescription function. *Phys Med Biol.* 2009;54(6):1483-1501.

76. South CP, Evans PM, Partridge M. Dose prescription complexity versus tumor control probability in biologically conformal radiotherapy. *Med Phys.* Oct 2009;36(10):4379-4388.

77. Heukelom J, Hamming O, Bartelink H, et al. Adaptive and innovative Radiation Treatment FOR improving Cancer treatment outcomE (ARTFORCE); a randomized controlled phase II trial for individualized treatment of head and neck cancer. *BMC Cancer.* 2013;13:84.

78. Jingu K, Ariga H, Kaneta T, et al. Focal dose escalation using FDG-PET-guided intensity-modulated radiation therapy boost for postoperative local recurrent rectal cancer: a planning study with comparison of DVH and NTCP. *BMC Cancer.* 2010;10:127.

79. van Elmpt W, De Ruysscher D, van der Salm A, et al. The PET-boost randomised phase II dose-escalation trial in non-small cell lung cancer. *Radiother Oncol.* 2012;104(1):67-71.

80. Kissick MW, Mo X, McCall KC, Schubert LK, Westerly DC, Mackie TR. A phantom model demonstration of tomotherapy dose painting delivery, including managed respiratory motion without motion management. *Phys Med Biol.* 2010;55(10):2983-2995.

81. Korreman SS, Ulrich S, Bowen S, Deveau M, Bentzen SM, Jeraj R. Feasibility of dose painting using volumetric modulated arc optimization and delivery. *Acta Oncol.* 2010;49(7):964-971.

82. Kim Y, Tome WA. Dose-painting IMRT optimization using biological parameters. *Acta Oncol.* 2010;49(8):1374-1384.

83. Rickhey M, Moravek Z, Eilles C, Koelbl O, Bogner L. 18F-FET-PET-based dose painting by numbers with protons. *Strahlenther Onkol.* Jun 2010;186(6):320-326.

84. Le Maitre A, Hatt M, Le Rest CC, Pradier O, Visvikis D. Adapting dose prescription to tumour heterogeneities: The impact of the functional contrast. Paper presented at: Nuclear Science Symposium Conference Record (NSS/MIC), 2010 IEEE; Oct. 30 2010-Nov. 6 2010, 2010.

85. Shi K, Astner ST, Sun L, et al. Sparse dose painting based on a dual-pass kinetic-oxygen mapping of dynamic PET images. *Med Image Comput Comput Assist Interv.* 2011;14(Pt 1):484-491.

86. Meijer G, Steenhuijsen J, Bal M, De Jaeger K, Schuring D, Theuws J. Dose painting by contours versus dose painting by numbers for stage II/III lung cancer: practical implications of using a broad or sharp brush. *Radiother Oncol.* Sep 2011;100(3):396-401.

87. Aristophanous M, Yap JT, Killoran JH, Chen AB, Berbeco RI. Four-dimensional positron emission tomography: implications for dose painting of high-uptake regions. *Int J Radiat Oncol Biol Phys.* Jul 1 2011;80(3):900-908.

88. Hendrickson K, Phillips M, Smith W, Peterson L, Krohn K, Rajendran J. Hypoxia imaging with [F-18] FMISO-PET in head and neck cancer: potential for guiding intensity modulated radiation therapy in overcoming hypoxia-induced treatment resistance. *Radiother Oncol.* Dec 2011;101(3):369-375.

89. Rodal J, Waldeland E, Sovik A, Malinen E. Dosimetric verification of biologically adapted IMRT. *Med Phys.* May 2011;38(5):2586-2594.

90. Witte M, Shakirin G, Houweling A, Peulen H, van Herk M. Dealing with geometric uncertainties in dose painting by numbers: introducing the DeltaVH. *Radiother Oncol.* Sep 2011;100(3):402-406.

91. Hardcastle N, Tome WA, Foo K, Miller A, Carolan M, Metcalfe P. Comparison of prostate IMRT and VMAT biologically optimised treatment plans. *Medical dosimetry : official journal of the American Association of Medical Dosimetrists.* 2011;36(3):292-298.

92. Chang JH, Lim Joon D, Lee ST, et al. Intensity modulated radiation therapy dose painting for localized prostate cancer using (1)(1)C-choline positron emission tomography scans. *Int J Radiat Oncol Biol Phys.* Aug 1 2012;83(5):e691-696.

93. Dirscherl T, Rickhey M, Bogner L. Feasibility of TCP-based dose painting by numbers applied to a prostate case with (18)F-choline PET imaging. *Z Med Phys.* Feb 2012;22(1):48-57.

94. Toma-Dasu I, Uhrdin J, Antonovic L, et al. Dose prescription and treatment planning based on FMISO-PET hypoxia. *Acta Oncol.* 2012;51(2):222-230.

95. Bowen SR, Chappell RJ, Bentzen SM, Deveau MA, Forrest LJ, Jeraj R. Spatially resolved regression analysis of pre-treatment FDG, FLT and Cu-ATSM PET from post-treatment FDG PET: An exploratory study. *Radiother Oncol.* Jun 8 2012.

96. Hardcastle N, Tome WA. Risk-adaptive volumetric modulated arc therapy using biological objective functions for subvolume boosting in radiotherapy. *Computational and mathematical methods in medicine.* 2012;2012:348471.

97. Chang JH, Wada M, Anderson NJ, et al. Hypoxia-targeted radiotherapy dose painting for head and neck cancer using F-FMISO PET: A biological modeling study. *Acta Oncol.* Nov 2013;52(8):1723-1729.

98. Rusten E, Rodal J, Bruland OS, Malinen E. Biologic targets identified from dynamic FDG-PET and implications for image-guided therapy. *Acta Oncol.* Aug 28 2013.

99. Teoh M, Beveridge S, Wood K, et al. Volumetric-modulated arc therapy (RapidArc) vs. conventional fixed-field intensity-modulated radiotherapy for ^{8}F-FDG-PET-guided dose escalation in oropharyngeal cancer: a planning study. *Medical dosimetry : official journal of the American Association of Medical Dosimetrists.* 2013;38(1):18-24.

100. Vogelius IR, Hakansson K, Due AK, et al. Failure-probability driven dose painting. *Med Phys.* Aug 2013;40(8):081717.

101. Hakansson K, Specht L, Aznar MC, Rasmussen JH, Bentzen SM, Vogelius IR. Prescribing and evaluating target dose in dose-painting treatment plans. *Acta Oncol.* 2014;53(9):1251-1256.

102. Olteanu LAM, Berwouts D, Madani I, et al. Comparative dosimetry of three-phase adaptive and non-adaptive dose-painting IMRT for head-and-neck cancer. *Radiother Oncol.* 2014;111(3):348-353.

103. Park Y-K, Park S, Wu H-G, Kim S. A new plan quality index for dose painting radiotherapy. *J Appl Clin Med Phys.* 2014;15(4):4941.

104. Alfonso JCL, Jagiella N, Nunez L, Herrero MA, Drasdo D. Estimating dose painting effects in radiotherapy: a mathematical model. *PLoS One.* 2014;9(2):e89380.

105. Pinkawa M, Piroth MD, Holy R, et al. Dose-escalation using intensity-modulated radiotherapy for prostate cancer - evaluation of quality of life with and without (18)F-choline PET-CT detected simultaneous integrated boost. *Radiat Oncol.* 2012;7:14.

106. Unkelbach J, Bortfeld T, Martin BC, Soukup M. Reducing the sensitivity of IMPT treatment plans to setup errors and range uncertainties via probabilistic treatment planning. *Med Phys.* Jan 2009;36(1):149-163.

107. Christian N, Lee JA, Bol A, De Bast M, Jordan B, Gregoire V. The limitation of PET imaging for biological adaptive-IMRT assessed in animal models. *Radiother Oncol.* Apr 2009;91(1):101-106.

108. Fletcher JW, Djulbegovic B, Soares HP, et al. Recommendations on the use of 18F-FDG PET in oncology. *J Nucl Med.* 2008;49(3):480-508.

109. Soto DE, Kessler ML, Piert M, Eisbruch A. Correlation between pretreatment FDG-PET biological target volume and anatomical location of failure after radiation therapy for head and neck cancers. *Radiother Oncol.* 2008;89(1):13-18.

110. Bos R, van Der Hoeven JJM, van Der Wall E, et al. Biologic correlates of (18)fluorodeoxyglucose uptake in human breast cancer measured by positron emission tomography. *J Clin Oncol.* 2002;20(2):379-387.

111. Zhao S, Kuge Y, Mochizuki T, et al. Biologic correlates of intratumoral heterogeneity in 18F-FDG distribution with regional expression of glucose transporters and hexokinase-II in experimental tumor. *J Nucl Med.* 2005;46(4):675-682.

112. van Waarde A, Cobben DCP, Suurmeijer AJH, et al. Selectivity of 18F-FLT and 18F-FDG for differentiating tumor from inflammation in a rodent model. *J Nucl Med.* 2004;45(4):695-700.

113. Buck AK, Halter G, Schirrmeister H, et al. Imaging proliferation in lung tumors with PET: 18F-FLT versus 18F-FDG. *J Nucl Med.* 2003;44(9):1426-1431.

114. Rasey JS, Grierson JR, Wiens LW, Kolb PD, Schwartz JL. Validation of FLT uptake as a measure of thymidine kinase-1 activity in A549 carcinoma cells. *J Nucl Med.* 2002;43(9):1210-1217.

115. Bergonie J, Tribondeau L. Interpretation of some results from radiotherapy and an attempt to determine a rational treatment technique. 1906. *Comptes Rendus des Seances de l'Academie des Sciences.* 1906;143:983-985.

116. Begg AC, Haustermans K, Hart AA, et al. The value of pretreatment cell kinetic parameters as predictors for radiotherapy outcome in head and neck cancer: a multicenter analysis. *Radiother Oncol.* 1999;50(1):13-23.

117. Kim JJ, Tannock IF. Repopulation of cancer cells during therapy: an important cause of treatment failure. *Nat Rev Cancer.* Jul 2005;5(7):516-525.

118. Vera P, Bohn P, Edet-Sanson A, et al. Simultaneous positron emission tomography (PET) assessment of metabolism with ^{8}F-fluoro-2-deoxy-d-glucose (FDG), proliferation with ^{8}F-fluoro-thymidine (FLT), and hypoxia with ^{8}fluoro-misonidazole (F-miso) before and during radiotherapy in patients with non-small-cell lung cancer (NSCLC): a pilot study. *Radiother Oncol.* 2011;98(1):109-116.

119. Yue J, Chen L, Cabrera AR, et al. Measuring tumor cell proliferation with 18F-FLT PET during radiotherapy of esophageal squamous cell carcinoma: a pilot clinical study. *J Nucl Med.* 2010;51(4):528-534.

120. Hoeben BAW, Troost EGC, Span PN, et al. 18F-FLT PET During Radiotherapy or Chemoradiotherapy in Head and Neck Squamous Cell Carcinoma Is an Early Predictor of Outcome. *J Nucl Med.* 2013;54(4):532-540.

121. Everitt S, Hicks RJ, Ball D, et al. Imaging cellular proliferation during chemo-radiotherapy: a pilot study of serial 18F-FLT positron emission tomography/computed tomography imaging for non-small-cell lung cancer. *Int J Radiat Oncol Biol Phys.* 2009;75(4):1098-1104.

122. Becker A, Hansgen G, Bloching M, Weigel C, Lautenschlager C, Dunst J. Oxygenation of squamous cell carcinoma of the head and neck: comparison of primary tumors, neck node metastases, and normal tissue. *Int J Radiat Oncol Biol Phys.* Aug 1 1998;42(1):35-41.

123. Rudat V, Vanselow B, Wollensack P, et al. Repeatability and prognostic impact of the pretreatment pO(2) histography in patients with advanced head and neck cancer. *Radiother Oncol.* Oct 2000;57(1):31-37.

124. Ewing D. The oxygen fixation hypothesis: a reevaluation. *Am J Clin Oncol.* Aug 1998;21(4):355-361.

125. Dewhirst MW, Cao Y, Moeller B. Cycling hypoxia and free radicals regulate angiogenesis and radiotherapy response. *Nat Rev Cancer.* 2008;8(6):425-437.

126. Chan N, Koch CJ, Bristow RG. Tumor hypoxia as a modifier of DNA strand break and cross-link repair. *Curr Mol Med.* 2009;9(4):401-410.

127. Fujibayashi Y, Taniuchi H, Yonekura Y, Ohtani H, Konishi J, Yokoyama A. Copper-62-ATSM: a new hypoxia imaging agent with high membrane permeability and low redox potential. *J Nucl Med.* 1997;38(7):1155-1160.

128. Rasey JS, Koh WJ, Grierson JR, Grunbaum Z, Krohn KA. Radiolabelled fluoromisonidazole as an imaging agent for tumor hypoxia. *Int J Radiat Oncol Biol Phys.* Nov 1989;17(5):985-991.

129. Krohn KA, Link JM, Mason RP. Molecular imaging of hypoxia. *J Nucl Med.* Jun 2008;49 Suppl 2:129S-148S.

130. Minagawa Y, Shizukuishi K, Koike I, et al. Assessment of tumor hypoxia by 62Cu-ATSM PET/CT as a predictor of response in head and neck cancer: a pilot study. *Ann Nucl Med.* 2011;25(5):339-345.

131. Sato Y, Tsujikawa T, Oh M, et al. Assessing Tumor Hypoxia in Head and Neck Cancer by PET With 62Cu-Diacetyl-Bis(N4-Methylthiosemicarbazone). *Clin Nucl Med.* Aug 19 2014.

132. Dehdashti F, Grigsby PW, Mintun MA, Lewis JS, Siegel BA, Welch MJ. Assessing tumor hypoxia in cervical cancer by positron emission tomography with 60Cu-ATSM: relationship to therapeutic response-a preliminary report. *Int J Radiat Oncol Biol Phys.* Apr 1 2003;55(5):1233-1238.

133. Dehdashti F, Grigsby PW, Lewis JS, Laforest R, Siegel BA, Welch MJ. Assessing tumor hypoxia in cervical cancer by PET with 60Cu-labeled diacetyl-bis(N4-methylthiosemicarbazone). *J Nucl Med.* 2008;49(2):201-205.

134. Dehdashti F, Mintun MA, Lewis JS, et al. In vivo assessment of tumor hypoxia in lung cancer with 60Cu-ATSM. *Eur J Nucl Med Mol Imaging.* 2003;30(6):844-850.

135. Dietz DW, Dehdashti F, Grigsby PW, et al. Tumor hypoxia detected by positron emission tomography with 60Cu-ATSM as a predictor of response and survival in patients undergoing Neoadjuvant chemoradiotherapy for rectal carcinoma: a pilot study. *Dis Colon Rectum.* 2008;51(11):1641-1648.

136. Dirix P, Vandecaveye V, De Keyzer F, Stroobants S, Hermans R, Nuyts S. Dose painting in radiotherapy for head and neck squamous cell carcinoma: value of repeated functional imaging with (18)F-FDG PET, (18)F-fluoromisonidazole PET, diffusion-weighted MRI, and dynamic contrast-enhanced MRI. *J Nucl Med.* Jul 2009;50(7):1020-1027.

137. Kubicek LN, Seo S, Chappell RJ, Jeraj R, Forrest LJ. Helical tomotherapy setup variations in canine nasal tumor patients immobilized with a bite block. *Vet Radiol Ultrasound.* Jul-Aug 2012;53(4):474-481.

138. Bradshaw TJ, Bowen SR, Jallow N, Forrest LJ, Jeraj R. Heterogeneity in Intratumor Correlations of 18F-FDG, 18F-FLT, and 61Cu-ATSM PET in Canine Sinonasal Tumors. *J Nucl Med.* Sep 16 2013.

139. Bradshaw TJ, Yip S, Jallow N, Forrest LJ, Jeraj R. Spatiotemporal stability of Cu-ATSM and FLT positron emission tomography distributions during radiation therapy. *Int J Radiat Oncol Biol Phys.* 2014.

140. Adams WM, Kleiter MM, Thrall DE, et al. Prognostic significance of tumor histology and computed tomographic staging for radiation treatment response of canine nasal tumors. *Vet Radiol Ultrasound.* May-Jun 2009;50(3):330-335.

141. Bradshaw TJ, Bowen SR, Jallow N, Forrest LJ, Jeraj R. Heterogeneity in intratumor correlations of 18F-FDG, 18F-FLT, and 61Cu-ATSM PET in canine sinonasal tumors. *J Nucl Med.* Nov 2013;54(11):1931-1937.

142. Nordsmark M, Overgaard M, Overgaard J. Pretreatment oxygenation predicts radiation response in advanced squamous cell carcinoma of the head and neck. *Radiother Oncol.* Oct 1996;41(1):31-39.

143. Roels S, Slagmolen P, Nuyts J, et al. Biological image-guided radiotherapy in rectal cancer: is there a role for FMISO or FLT, next to FDG? *Acta Oncol.* 2008;47(7):1237-1248.

144. Nehmeh SA, Lee NY, Schroder H, et al. Reproducibility of intratumor distribution of (18)F-fluoromisonidazole in head and neck cancer. *Int J Radiat Oncol Biol Phys.* 2008;70(1):235-242.

145. Okamoto S, Shiga T, Yasuda K, et al. High Reproducibility of Tumor Hypoxia Evaluated by 18F-Fluoromisonidazole PET for Head and Neck Cancer. *J Nucl Med.* Feb 2013;54(2):201-207.

146. Avila-Rodriguez M. *Low Energy Cyclotron Production of Multivalent Transition Metals for PET Imaging and Therapy*. Madison: Medical Physics, University of Wisconsin; 2007.

147. Yang D, Brame S, El Naqa I, et al. Technical note: DIRART--A software suite for deformable image registration and adaptive radiotherapy research. *Med Phys.* 2011;38(1):67-77.

148. McCall KC, Barbee DL, Kissick MW, Jeraj R. PET imaging for the quantification of biologically heterogeneous tumours: measuring the effect of relative position on image-based quantification of dose-painting targets. *Phys Med Biol.* 2010;55(10):2789-2806.

149. Nyflot MJ, Harari PM, Yip S, Perlman SB, Jeraj R. Correlation of PET images of metabolism, proliferation and hypoxia to characterize tumor phenotype in patients with cancer of the oropharynx. *Radiother Oncol.* Oct 2012;105(1):36-40.

150. Murata R, Shibamoto Y, Sasai K, et al. Reoxygenation after single irradiation in rodent tumors of different types and sizes. *Int J Radiat Oncol Biol Phys.* Mar 1 1996;34(4):859-865.

151. Iliakis G, Wang Y, Guan J, Wang H. DNA damage checkpoint control in cells exposed to ionizing radiation. *Oncogene.* 2003;22(37):5834-5847.

152. Hansen K, Khanna C. Spontaneous and genetically engineered animal models; use in preclinical cancer drug development. *Eur J Cancer.* Apr 2004;40(6):858-880.

153. Fuchs K, Kukuk D, Reischl G, et al. Oxygen Breathing Affects 3'-Deoxy-3'-18F-Fluorothymidine Uptake in Mouse Models of Arthritis and Cancer. *J Nucl Med.* May 2012;53(5):823-830.

154. Kersemans V, Cornelissen B, Hueting R, et al. Hypoxia imaging using PET and SPECT: the effects of anesthetic and carrier gas on [Cu]-ATSM, [Tc]-HL91 and [F]-FMISO tumor hypoxia accumulation. *PLoS One.* 2011;6(11):e25911.

155. Basken NE, Green MA. Cu(II) bis(thiosemicarbazone) radiopharmaceutical binding to serum albumin: further definition of species dependence and associated substituent effects. *Nucl Med Biol.* 2009;36(5):495-504.

156. Dilworth JR, Hueting R. Metal complexes of thiosemicarbazones for imaging and therapy. *Inorganica Chimica Acta.* 2012;389(0):3-15.

157. Donnelly PS, Liddell JR, Lim S, et al. An impaired mitochondrial electron transport chain increases retention of the hypoxia imaging agent diacetylbis(4-methylthiosemicarbazonato)copperII. *Proc Natl Acad Sci U S A.* Jan 3 2012;109(1):47-52.

158. O'Donoghue JA, Zanzonico P, Pugachev A, et al. Assessment of regional tumor hypoxia using 18F-fluoromisonidazole and 64Cu(II)-diacetyl-bis(N4-methylthiosemicarbazone) positron emission tomography: Comparative study featuring microPET imaging, Po2 probe measurement, autoradiography, and fluorescent microscopy in the R3327-AT and FaDu rat tumor models. *Int J Radiat Oncol Biol Phys.* Apr 1 2005;61(5):1493-1502.

159. Gerlinger M, Rowan AJ, Horswell S, et al. Intratumor heterogeneity and branched evolution revealed by multiregion sequencing. *The New England Journal of Medicine.* 2012;366(10):883-892.

160. *venn* [computer program]. Version: MATLAB Central File Exchange; 2008.

161. Hansen AE, McEvoy F, Engelholm SA, Law I, Kristensen AT. FDG PET/CT imaging in canine cancer patients. *Vet Radiol Ultrasound.* 2011;52(2):201-206.

162. Kaira K, Okumura T, Ohde Y, et al. Correlation between 18F-FDG uptake on PET and molecular biology in metastatic pulmonary tumors. *J Nucl Med.* 2011;52(5):705-711.

163. Gelderblom H, Hogendoorn PCW, Dijkstra SD, et al. The clinical approach towards chondrosarcoma. *Oncologist.* 2008;13(3):320-329.

164. La Fontaine MD. *The viability of DCE-CT kinetic analysis in tumor vasculature imaging in veterinary medicine* [Ph.D.]. Madison, The University of Wisconsin - Madison; 2014.

165. Vaupel P. The role of hypoxia-induced factors in tumor progression. *Oncologist.* 2004;9 Suppl 5:10-17.

166. Gardner LB, Li Q, Park MS, Flanagan WM, Semenza GL, Dang CV. Hypoxia inhibits G1/S transition through regulation of p27 expression. *J Biol Chem.* 2001;276(11):7919-7926.

167. Kondo Y, Matsunaga S, Mochizuki M, et al. Prognosis of canine patients with nasal tumors according to modified clinical stages based on computed tomography: a retrospective study. *J Vet Med Sci.* Mar 2008;70(3):207-212.

168. Eary JF, O'Sullivan F, O'Sullivan J, Conrad EU. Spatial heterogeneity in sarcoma 18F-FDG uptake as a predictor of patient outcome. *J Nucl Med.* 2008;49(12):1973-1979.

169. Busk M, Horsman MR, Kristjansen PEG, van der Kogel AJ, Bussink J, Overgaard J. Aerobic glycolysis in cancers: implications for the usability of oxygen-responsive genes and fluorodeoxyglucose-PET as markers of tissue hypoxia. *Int J Cancer.* 2008;122(12):2726-2734.

170. Lohith TG, Kudo T, Demura Y, et al. Pathophysiologic correlation between 62Cu-ATSM and 18F-FDG in lung cancer. *J Nucl Med.* 2009;50(12):1948-1953.

171. Rajendran JG, Mankoff DA, O'Sullivan F, et al. Hypoxia and glucose metabolism in malignant tumors: evaluation by [18F]fluoromisonidazole and [18F]fluorodeoxyglucose positron emission tomography imaging. *Clin Cancer Res.* 2004;10(7):2245-2252.

172. Yoshii Y, Furukawa T, Kiyono Y, et al. Copper-64-diacetyl-bis (N4-methylthiosemicarbazone) accumulates in rich regions of CD133+ highly tumorigenic cells in mouse colon carcinoma. *Nucl Med Biol.* 2010;37(4):395-404.

173. Oh M, Tanaka T, Kobayashi M, et al. Radio-copper-labeled Cu-ATSM: an indicator of quiescent but clonogenic cells under mild hypoxia in a Lewis lung carcinoma model. *Nucl Med Biol.* 2009;36(4):419-426.

174. Hansen AE, Kristensen AT, Law I, McEvoy FJ, Kjar A, Engelholm SA. Multimodality functional imaging of spontaneous canine tumors using 64Cu-ATSM and 18FDG PET/CT and dynamic contrast enhanced perfusion CT. *Radiother Oncol.* 2012;102(3):424-428.

175. Dence CS, Ponde DE, Welch MJ, Lewis JS. Autoradiographic and small-animal PET comparisons between (18)F-FMISO, (18)F-FDG, (18)F-FLT and the hypoxic selective (64)Cu-ATSM in a rodent model of cancer. *Nucl Med Biol.* 2008;35(6):713-720.

176. Huang T, Civelek AC, Li J, et al. Tumor microenvironment-dependent 18F-FDG, 18F-fluorothymidine, and 18F-misonidazole uptake: a pilot study in mouse models of human non-small cell lung cancer. *J Nucl Med.* Aug 2012;53(8):1262-1268.

177. Yamada K, Brink I, Bisse E, Epting T, Engelhardt R. Factors influencing [F-18] 2-fluoro-2-deoxy-D-glucose (F-18 FDG) uptake in melanoma cells: the role of proliferation rate, viability, glucose transporter expression and hexokinase activity. *J Dermatol.* May 2005;32(5):316-334.

178. Baird K, Davis S, Antonescu CR, et al. Gene expression profiling of human sarcomas: insights into sarcoma biology. *Cancer Res.* Oct 15 2005;65(20):9226-9235.

179. Aerts HJ, Bussink J, Oyen WJ, et al. Identification of residual metabolic-active areas within NSCLC tumours using a pre-radiotherapy FDG-PET-CT scan: a prospective validation. *Lung Cancer.* Jan 2012;75(1):73-76.

180. Shusharina N, Cho J, Sharp GC, Choi NC. Correlation of (18)F-FDG Avid Volumes on Pre-Radiation Therapy and Post-Radiation Therapy FDG PET Scans in Recurrent Lung Cancer. *Int J Radiat Oncol Biol Phys.* May 1 2014;89(1):137-144.

181. Galavis PE. *(PhD Thesis) Robust tumor segmentation for radiotherapy target definition*. Madison: Medical Physics, University of Wisconsin; 2013.

182. Loh W-Y. Classification and regression trees. *Wiley Interdisciplinary Reviews: Data Mining and Knowledge Discovery.* 2011;1(1):14-23.

183. Breiman L, Friedman JH, Olshen RA, Stone CJ. *Classification and Regression Trees*: CRC Press; 1984.

184. Kinoshita M, Arita H, Goto T, et al. A Novel PET Index, 18F-FDG-11C-Methionine Uptake Decoupling Score, Reflects Glioma Cell Infiltration. *J Nucl Med.* Nov 2012;53(11):1701-1708.

185. Abramyuk A, Tokalov S, Zophel K, et al. Is pre-therapeutical FDG-PET/CT capable to detect high risk tumor subvolumes responsible for local failure in non-small cell lung cancer? *Radiother Oncol.* 2009;91(3):399-404.

186. Bollineni VR, Widder J, Pruim J, Langendijk JA, Wiegman EM. Residual ^{8}F-FDG-PET uptake 12 weeks after stereotactic ablative radiotherapy for stage I non-small-cell lung cancer predicts local control. *Int J Radiat Oncol Biol Phys.* 2012;83(4):e551-555.

187. Inoue T, Kim EE, Komaki R, et al. Detecting recurrent or residual lung cancer with FDG-PET. *J Nucl Med.* 1995;36(5):788-793.

188. Levine EA, Farmer MR, Clark P, et al. Predictive value of 18-fluoro-deoxy-glucose-positron emission tomography (18F-FDG-PET) in the identification of responders to chemoradiation therapy for the treatment of locally advanced esophageal cancer. *Ann Surg.* 2006;243(4):472-478.

189. Bradshaw TJ, Bowen SR, Deveau M, et al. Molecular imaging biomarkers of resistance to radiation therapy for spontaneous nasal tumors in canines. *Int J Radiat Oncol Biol Phys.* [In press].

190. Hedman M, Bjork-Eriksson T, Mercke C, West C, Hesselius P, Brodin O. Comparison of predicted and clinical response to radiotherapy: a radiobiology modelling study. *Acta Oncol.* 2009;48(4):584-590.

191. Chen M, Jiang G-L, Fu X-L, et al. Prognostic factors for local control in non-small-cell lung cancer treated with definitive radiation therapy. *Am J Clin Oncol.* 2002;25(1):76-80.

192. Bibault J-E, Fumagalli I, Ferte C, Chargari C, Soria J-C, Deutsch E. Personalized radiation therapy and biomarker-driven treatment strategies: a systematic review. *Cancer metastasis reviews.* 2013;32(3-4):479-492.

193. Van de Wiele C, Lahorte C, Oyen W, et al. Nuclear medicine imaging to predict response to radiotherapy: a review. *Int J Radiat Oncol Biol Phys.* 2003;55(1):5-15.

194. Concato J, Peduzzi P, Holford TR, Feinstein AR. Importance of events per independent variable in proportional hazards analysis. I. Background, goals, and general strategy. *J Clin Epidemiol.* Dec 1995;48(12):1495-1501.

195. Peduzzi P, Concato J, Feinstein AR, Holford TR. Importance of events per independent variable in proportional hazards regression analysis. II. Accuracy and precision of regression estimates. *J Clin Epidemiol.* Dec 1995;48(12):1503-1510.

196. Cox DH, Snell EJ. *Analysis of binary data*. 2nd ed. London: Chapman and Hall; 1989.

197. Menda Y, Boles Ponto LL, Dornfeld KJ, et al. Kinetic analysis of 3'-deoxy-3'-(18)F-fluorothymidine ((18)F-FLT) in head and neck cancer patients before and early after initiation of chemoradiation therapy. *J Nucl Med.* 2009;50(7):1028-1035.

198. Wieder HA, Geinitz H, Rosenberg R, et al. PET imaging with [18F]3'-deoxy-3'-fluorothymidine for prediction of response to neoadjuvant treatment in patients with rectal cancer. *Eur J Nucl Med Mol Imaging.* Jun 2007;34(6):878-883.

199. Trigonis I, Koh PK, Taylor B, et al. Early reduction in tumour [(18)F]fluorothymidine (FLT) uptake in patients with non-small cell lung cancer (NSCLC) treated with radiotherapy alone. *Eur J Nucl Med Mol Imaging.* Apr 2014;41(4):682-693.

200. Vera P, Bohn P, Edet-Sanson A, et al. Simultaneous positron emission tomography (PET) assessment of metabolism with 18F-fluoro-2-deoxy-d-glucose (FDG), proliferation with 18F-fluoro-thymidine (FLT), and hypoxia with 18fluoro-misonidazole (F-miso) before and during radiotherapy in patients with non-small-cell lung cancer (NSCLC): a pilot study. *Radiother Oncol.* 2011;98(1):109-116.

201. Sohn H-J, Yang Y-J, Ryu J-S, et al. [18F]Fluorothymidine positron emission tomography before and 7 days after gefitinib treatment predicts response in patients with advanced adenocarcinoma of the lung. *Clin Cancer Res.* 2008;14(22):7423-7429.

202. Zander T, Scheffler M, Nogova L, et al. Early prediction of nonprogression in advanced non-small-cell lung cancer treated with erlotinib by using [(18)F]fluorodeoxyglucose and [(18)F]fluorothymidine positron emission tomography. *J Clin Oncol.* 2011;29(13):1701-1708.

203. Brink C, Bernchou U, Bertelsen A, Hansen O, Schytte T, Bentzen SM. Locoregional control of non-small cell lung cancer in relation to automated early assessment of tumor regression on cone beam computed tomography. *Int J Radiat Oncol Biol Phys.* Jul 15 2014;89(4):916-923.

204. LaDue TA, Dodge R, Page RL, Price GS, Hauck ML, Thrall DE. Factors influencing survival after radiotherapy of nasal tumors in 130 dogs. *Vet Radiol Ultrasound.* 1999;40(3):312-317.

205. Yoon JH, Feeney DA, Jessen CR, Walter PA. External-beam Co-60 radiotherapy for canine nasal tumors: a comparison of survival by treatment protocol. *Res Vet Sci.* 2008;84(1):140-149.

206. Orlhac F, Soussan M, Maisonobe JA, Garcia CA, Vanderlinden B, Buvat I. Tumor texture analysis in 18F-FDG PET: relationships between texture parameters, histogram indices, standardized uptake values, metabolic volumes, and total lesion glycolysis. *J Nucl Med.* Mar 2014;55(3):414-422.

207. Thorwarth D, Eschmann S-M, Holzner F, Paulsen F, Alber M. Combined uptake of [18F]FDG and [18F]FMISO correlates with radiation therapy outcome in head-and-neck cancer patients. *Radiother Oncol.* 2006;80(2):151-156.

208. Obata A, Yoshimoto M, Kasamatsu S, et al. Intra-tumoral distribution of (64)Cu-ATSM: a comparison study with FDG. *Nucl Med Biol.* 2003;30(5):529-534.

209. Paoloni M, Khanna C. Translation of new cancer treatments from pet dogs to humans. *Nat Rev Cancer.* Feb 2008;8(2):147-156.

210. Lewis JS, Sharp TL, Laforest R, Fujibayashi Y, Welch MJ. Tumor uptake of copper-diacetyl-bis(N(4)-methylthiosemicarbazone): effect of changes in tissue oxygenation. *J Nucl Med.* Apr 2001;42(4):655-661.

211. Hueting R, Kersemans V, Cornelissen B, et al. A comparison of the behavior of (64)Cu-acetate and (64)Cu-ATSM in vitro and in vivo. *J Nucl Med.* Jan 2014;55(1):128-134.

212. Valtorta S, Belloli S, Sanvito F, et al. Comparison of 18F-Fluoroazomycin-Arabinofuranoside and 64Cu-Diacetyl-Bis(N4-Methylthiosemicarbazone) in Preclinical Models of Cancer. *J Nucl Med.* Jul 2013;54(7):1106-1112.

213. Yuan H, Schroeder T, Bowsher JE, Hedlund LW, Wong T, Dewhirst MW. Intertumoral differences in hypoxia selectivity of the PET imaging agent 64Cu(II)-diacetyl-bis(N4-methylthiosemicarbazone). *J Nucl Med.* 2006;47(6):989-998.

214. Burgman P, O'Donoghue JA, Lewis JS, Welch MJ, Humm JL, Ling CC. Cell line-dependent differences in uptake and retention of the hypoxia-selective nuclear imaging agent Cu-ATSM. *Nucl Med Biol.* Aug 2005;32(6):623-630.

215. Katano K, Safaei R, Samimi G, Holzer A, Rochdi M, Howell SB. The copper export pump ATP7B modulates the cellular pharmacology of carboplatin in ovarian carcinoma cells. *Mol Pharmacol.* 2003;64(2):466-473.

216. Peng F, Lu X, Janisse J, Muzik O, Shields AF. PET of human prostate cancer xenografts in mice with increased uptake of 64CuCl2. *J Nucl Med.* Oct 2006;47(10):1649-1652.

217. Jorgensen JT, Persson M, Madsen J, Kjaer A. High tumor uptake of (64)Cu: implications for molecular imaging of tumor characteristics with copper-based PET tracers. *Nucl Med Biol.* Apr 2013;40(3):345-350.

218. Busk M, Mortensen LS, Nordsmark M, et al. PET hypoxia imaging with FAZA: reproducibility at baseline and during fractionated radiotherapy in tumour-bearing mice. *Eur J Nucl Med Mol Imaging.* 2013;40(2):186-197.

219. Piert M, Machulla HJ, Becker G, Aldinger P, Winter E, Bares R. Dependency of the [18F]fluoromisonidazole uptake on oxygen delivery and tissue oxygenation in the porcine liver. *Nucl Med Biol.* Nov 2000;27(8):693-700.

220. Rajendran JG, Schwartz DL, O'Sullivan J, et al. Tumor hypoxia imaging with [F-18] fluoromisonidazole positron emission tomography in head and neck cancer. *Clin Cancer Res.* 2006;12(18):5435-5441.

221. Satoh Y, Onishi H, Nambu A, Araki T. Volume-based parameters measured by using FDG PET/CT in patients with stage I NSCLC treated with stereotactic body radiation therapy: prognostic value. *Radiology.* Jan 2014;270(1):275-281.

222. Horne ZD, Clump DA, Vargo JA, et al. Pretreatment SUVmax predicts progression-free survival in early-stage non-small cell lung cancer treated with stereotactic body radiation therapy. *Radiat Oncol.* 2014;9:41.

223. Liu WS, Wu MF, Tseng HC, et al. The role of pretreatment FDG-PET in nasopharyngeal carcinoma treated with intensity-modulated radiotherapy. *Int J Radiat Oncol Biol Phys.* Feb 1 2012;82(2):561-566.

224. Schutze C, Bergmann R, Yaromina A, et al. Effect of increase of radiation dose on local control relates to pre-treatment FDG uptake in FaDu tumours in nude mice. *Radiother Oncol.* Jun 2007;83(3):311-315.

225. Ulger S, Demirci NY, Eroglu FN, et al. High FDG uptake predicts poorer survival in locally advanced nonsmall cell lung cancer patients undergoing curative radiotherapy, independently of tumor size. *J Cancer Res Clin Oncol.* Mar 2014;140(3):495-502.

226. Allal AS, Slosman DO, Kebdani T, Allaoua M, Lehmann W, Dulguerov P. Prediction of outcome in head-and-neck cancer patients using the standardized uptake value of 2-[18F]fluoro-2-deoxy-D-glucose. *Int J Radiat Oncol Biol Phys.* 2004;59(5):1295-1300.

227. Na F, Wang J, Li C, Deng L, Xue J, Lu Y. Primary tumor standardized uptake value measured on F18-Fluorodeoxyglucose positron emission tomography is of prediction value for survival and local control in non-small-cell lung cancer receiving radiotherapy: meta-analysis. *J Thorac Oncol.* Jun 2014;9(6):834-842.

228. Mikulits W, Hengstschlager M, Sauer T, Wintersberger E, Mullner EW. Overexpression of thymidine kinase mRNA eliminates cell cycle regulation of thymidine kinase enzyme activity. *J Biol Chem.* 1996;271(2):853-860.

229. Song S, Xiong C, Lu W, Ku G, Huang G, Li C. Apoptosis imaging probe predicts early chemotherapy response in preclinical models: A comparative study with 18F-FDG PET. *J Nucl Med.* 2013;54(1):104-110.

230. Niu G, Li Z, Xie J, Le Q-T, Chen X. PET of EGFR antibody distribution in head and neck squamous cell carcinoma models. *J Nucl Med.* 2009;50(7):1116-1123.

231. Kudo T, Ueda M, Konishi H, et al. PET imaging of hypoxia-inducible factor-1-active tumor cells with pretargeted oxygen-dependent degradable streptavidin and a novel 18F-labeled biotin derivative. *Mol Imaging Biol.* 2011;13(5):1003-1010.

232. Gaedicke S, Braun F, Prasad S, et al. Noninvasive positron emission tomography and fluorescence imaging of CD133+ tumor stem cells. *Proc Natl Acad Sci U S A.* 2014;111(6):E692-701.

233. Tian J, Yang X, Yu L, et al. A multicenter clinical trial on the diagnostic value of dual-tracer PET/CT in pulmonary lesions using 3'-deoxy-3'-18F-fluorothymidine and 18F-FDG. *J Nucl Med.* Feb 2008;49(2):186-194.

234. Lelandais B, Ruan S, Denoeux T, Vera P, Gardin I. Fusion of multi-tracer PET images for dose painting. *Medical image analysis.* 2014;18(7):1247-1259.

235. Xu B, Guan Z, Liu C, et al. Can multimodality imaging using 18F-FDG/18F-FLT PET/CT benefit the diagnosis and management of patients with pulmonary lesions? *Eur J Nucl Med Mol Imaging.* Feb 2011;38(2):285-292.

236. Schreibmann E, Waller AF, Crocker I, Curran W, Fox T. Voxel clustering for quantifying PET-based treatment response assessment. *Med Phys.* 2013;40(1):012401.

237. Ken S, Vieillevigne L, Franceries X, et al. Integration method of 3D MR spectroscopy into treatment planning system for glioblastoma IMRT dose painting with integrated simultaneous boost. *Radiat Oncol.* 2013;8:1.

238. McCall KC. *Effect of Patient Set-Up and Respiration Motion on Defining Biological Targets for Image-Guided Targeted Radiotherapy*. Madison: Medical Physics, University of Wisconsin; 2011.

239. Wang CC, Montgomery W, Efird J. Local control of oropharyngeal carcinoma by irradiation alone. *Laryngoscope.* May 1995;105(5 Pt 1):529-533.

240. Chen W, Cloughesy T, Kamdar N, et al. Imaging proliferation in brain tumors with 18F-FLT PET: comparison with 18F-FDG. *J Nucl Med.* Jun 2005;46(6):945-952.

241. Ricci PE, Karis JP, Heiserman JE, Fram EK, Bice AN, Drayer BP. Differentiating recurrent tumor from radiation necrosis: time for re-evaluation of positron emission tomography? *AJNR Am J Neuroradiol.* 1998;19(3):407-413.

242. Gross MW, Weber WA, Feldmann HJ, Bartenstein P, Schwaiger M, Molls M. The value of F-18-fluorodeoxyglucose PET for the 3-D radiation treatment planning of malignant gliomas. *Int J Radiat Oncol Biol Phys.* 1998;41(5):989-995.

243. Siegel R, Naishadham D, Jemal A. Cancer statistics, 2013. *CA: A Cancer Journal for Clinicians.* 2013;63(1):11-30.

244. Bowen SR, Nyflot MJ, Gensheimer M, et al. Challenges and opportunities in patient-specific, motion-managed and PET/CT-guided radiation therapy of lung cancer: review and perspective. *Clin Transl Med.* 2012;1(1):18.

245. Bowen SR, van der Kogel AJ, Nordsmark M, Bentzen SM, Jeraj R. Characterization of positron emission tomography hypoxia tracer uptake and tissue oxygenation via electrochemical modeling. *Nucl Med Biol.* 2011;38(6):771-780.

246. Guerrero T, Sanders K, Castillo E, et al. Dynamic ventilation imaging from four-dimensional computed tomography. *Phys Med Biol.* Feb 21 2006;51(4):777-791.

247. Ireland RH, Bragg CM, McJury M, et al. Feasibility of image registration and intensity-modulated radiotherapy planning with hyperpolarized helium-3 magnetic resonance imaging for non-small-cell lung cancer. *Int J Radiat Oncol Biol Phys.* 2007;68(1):273-281.

248. Petit SF, van Elmpt WJC, Oberije CJG, et al. [^{8}F]fluorodeoxyglucose uptake patterns in lung before radiotherapy identify areas more susceptible to radiation-induced lung toxicity in non-small-cell lung cancer patients. *Int J Radiat Oncol Biol Phys.* 2011;81(3):698-705.

249. Booth CM, Eisenhauer EA. Progression-free survival: meaningful or simply measurable? *J Clin Oncol.* 2012;30(10):1030-1033.

250. Richter WS. Imaging biomarkers as surrogate endpoints for drug development. *Eur J Nucl Med Mol Imaging.* Jul 2006;33 Suppl 1:6-10.